U.PORTO
FACULDADE DE CIÊNCIAS
UNIVERSIDADE DO PORTO

PhD

3rd CYCLE

FCUP
2025

U.PORTO

Probing the Internal Structure and Composition of Exoplanets

Nuno Miguel Pereira da Cruz Rosário

FC

U.PORTO
FACULDADE DE CIÊNCIAS
UNIVERSIDADE DO PORTO

Probing the Internal Structure and Composition of Exoplanets

Nuno Miguel Pereira da Cruz Rosário
Doctoral Program in Astronomy
Department of Physics and Astronomy
Faculty of Sciences of the University of Porto
2025

Probing the Internal Structure and Composition of Exoplanets

Nuno Miguel Pereira da Cruz Rosário
Thesis carried out as part of the Doctoral Program in Astronomy
Department of Physics and Astronomy
2025

Supervisor
Susana C. C. Barros, Senior Researcher, U. Porto, IA

Co-supervisors
Olivier D. S. Demangeon, Senior Researcher, U. Porto, IA
Nuno C. Santos, Full Professor, U. Porto, IA

Centro de Astrofísica
da Universidade do Porto

instituto de astrofísica
e ciências do espaço

" Trailblazing means taking paths your predecessors foreswore, and venturing even further. "

Trailblazer, in *Honkai: Star Rail*, by HoYoverse

Acknowledgements

Embarking on this journey among the planets and the stars was a difficult decision. Leaving behind what I had for the sake of learning and finding a new purpose was scary but exciting.

First and foremost, I would like to express my gratitude to my supervisor, Susana Barros, for accepting to guide me through what was a little over four years of many challenges and providing me with many opportunities within the scientific community that I would never be able to get otherwise. I am also very grateful to my co-supervisors, Olivier Demangeon and Nuno Santos, whose encouragement, insights, and contributions were fundamental to bringing this thesis to life. Undertaking a PhD is always a challenge, but starting one during a global pandemic, navigating online classes, virtual meetings, and limited in-person interactions, added an extra layer of difficulty. Despite these obstacles, I am truly thankful to all of you for believing in me and my work until the very end.

A special thank you to my family, especially my parents, who were maybe even more scared than I was when I made the decision to take this PhD full-time, but always provided all the support and all the encouragement to see me doing something I really wanted. I hope I can repay you and make you proud from now on.

To my friends and colleagues, thank you for being by my side throughout these years, offering encouragement when I needed it most. A special mention goes to my long-time friends from high school and my master's, who have known me for years and have always believed research was the right path for me, even before I did. Thank you for being there all these years, even if the chances to see each other are few and sparse. To my PhD colleagues, thank you for being part of this journey, for the much-needed laughter during lunch and after work, and for reassuring me that I was never alone in overcoming these challenges. Congratulations to those of you who have also finished in the meantime, and good luck to those of you who are yet to finish, I am sure you will succeed.

I would also like to extend my gratitude to everyone at CAUP, from researchers to the administrative and IT teams, whose assistance was instrumental in completing this PhD. A special thank you to the members of Axes 1 and 3 of the CHEOPS consortium, who placed their trust in my work and provided invaluable guidance. I would like to properly acknowledge Dr. Gwenaël Boué for providing me the necessary tools and theoretical background used in the last part of my work.

I would finally like to acknowledge the financial support by FCT through the PhD grant DFA/BD/5472/2020, which was essential for the development of this thesis. This work was also supported by FCT through national funds by these grants: UIDB/04434/2020, UIDP/04434/2020, 2022.06962.PTDC and 2022.04416.PTDC.

Once again, thank you to everyone who accompanied me in this journey and made this thesis possible.

Resumo

A descoberta de milhares de exoplanetas nas últimas décadas expandiu-se drasticamente o estudo de ciências planetárias. A caracterização detalhada de cada um destes novos planetas leva a potenciais desenvolvimentos na procura pela resposta a uma das perguntas mais antigas da humanidade, a possibilidade de existir vida noutros planetas semelhantes à Terra. Existem dois métodos particularmente bem-sucecidos na procura por exoplanetas, o método das velocidades radiais e o método dos trânsitos.

Nesta tese, fazemos uso de ambos os métodos para investigar e melhorar a caracterização do interior e da composição de exoplanetas. Na primeira parte do trabalho, utilizamos novos dados de missões como o TESS, o CHEOPS e o HARPS para estudar os dois planetas do sistema HD 15337, melhorando a precisão das medições dos seus raios e massas. De seguida, utilizamos esses novos valores num modelo de cálculo da estrutura interna para identificar a presença de camadas de água ou gás e aplicar novas restrições às restantes camadas do interior. A nossa análise revela no entanto que, apesar da elevada precisão das medições, estes modelos ainda possuem um grande grau de degenerescência e necessitam de outras formas de restringir cada camada e a respectiva composição.

Na segunda parte do trabalho, investigamos a interação entre as estrelas e planetas gigantes de períodos curtos. Utilizamos dados recentes de trânsitos observados pelo TESS para procurar evidências da dimunuição do período orbital causada pelas forças de maré. Derivamos os tempos dos trânsitos de forma precisa, juntando os novos valores aos mais antigos da literatura para fornecer parâmetros atualizados para os planetas WASP-18b e WASP-19b. Adicionalmente, derivamos novos limites para o valor do *tidal quality parameter* de ambas as estrelas, fornecendo pistas importantes para uma melhor compreensão do efeito das forças de maré na órbita dos planetas.

A forma destes planetas é também afetada pelas forças de maré e a deformação causada por estas pode ser observada através das curvas de luz obtidas durante os trânsitos, relacionada com a diferenciação do seu interior através do número de Love. Na parte final desta tese, tomamos uma abordagem mais teórica ao investigar a criação de um modelo capaz de calcular o número de Love de um planeta e correlacioná-lo com o tamanho e a massa do seu núcleo. Apesar deste trabalho se encontrar ainda em desenvolvimento, apresentamos os resultados preliminares obtidos através de um modelo analítico simples e também as potencialidades de futuros desenvolvimentos.

De um modo geral, este trabalho melhora a caracterização de exoplanetas. Aperfeiçoamos vários parâmetros planetários, investigamos as interações devido às forças de maré e exploramos novas abordagens para restringir a estrutura interna dos planetas. Apesar dos avanços significativos, os nossos resultados mostram as limitações dos modelos atuais e a necessidade de restrições adicionais. Missões futuras, como o PLATO, juntamente com observações espectroscópicas do JWST e ARIEL, terão um papel fundamental na resolução das degenerescências existentes, permitindo um melhor entendimento da estrutura e evolução planetária. Combinando estas observações com melhores modelos teóricos, podemos obter para uma compreensão mais abrangente da diversidade exoplanetária e continuar a busca por outra Terra.

Abstract

The discovery of thousands of exoplanets in recent decades has transformed planetary science, offering new opportunities to address one of humanity's most profound questions: the uniqueness of Earth as a life-hosting planet. Two primary methods, radial velocity (RV) and transit photometry, have been instrumental to detect and characterise exoplanets in recent years.

In this thesis, we use both methods to investigate and improve the characterisation of the interior and composition of exoplanets. In the first part of our work, we refine the parameters of the two planets of the HD 15337 system, using TESS, CHEOPS and HARPS to further enhance the measurements of mass and radius. The newly refined parameters are then used in a state-of-the-art internal structure model in order to constrain the layers of the interior and probe the existence of a water layer or a gas envelope. Despite improved data precision, our analysis highlights the inherent degeneracy in internal structure models, showing the need for additional constraints.

In the second part, we investigate the interaction between stars and close-in hot giant planets. We use up-to-date TESS transit data to find evidence towards orbital shrinkage caused by tidal forces. We derive precise transit timings and provide updated values for WASP-18b and WASP-19b, matching the new timing with previous timings from the literature. We further constrain the tidal quality parameter of both stars, providing new insights towards a better understanding of the effect of tides on stars and planets.

The shape of close-in planets is also impacted by tides, and the amount of tidal deformation can be measured through the analysis of transit light curves and linked to the level of differentiation of the planet's interior through its Love number. We present the development of a model to compute the Love number and correlate it with core mass. While this project is still in progress, we discuss preliminary results obtained through an analytical approach and early implementations in MESA, outlining future directions for this work.

Overall, this work improves the characterisation of exoplanets by refining key planetary parameters, investigating tidal interactions, and exploring new approaches to constraining planetary interiors. Despite significant progress, our findings show the limitations of current models and the need of additional constraints. Future missions such as PLATO, along with spectroscopic observations from JWST and ARIEL, will play a crucial role in resolving

existing degeneracies, improving our understanding of planetary structure and evolution. By combining high-precision observations with advanced modelling techniques, we can move toward a more comprehensive understanding of exoplanetary diversity and continue the search for another Earth.

Contents

List of Figures

Chapter 1

Introduction

With the ever growing discoveries made by science in recent years, we found that our galaxy is home to many other planetary systems, with the majority possessing architectures and planets very different from the Solar System (e.g. Batalha, 2014). Some systems include very hot, Jupiter-sized planets, with periods of less than a day (e.g.; WASP-19, Hebb et al., 2009b; TOI-2109, Wong et al., 2021) while others have planets with sizes between the Earth and the ice giants (e.g., HD 15337, Gandolfi et al., 2019; Dumusque et al., 2019; Rosário et al., 2024), two types of planets that are not present in the Solar System. The discovery of these planets challenged existing formation theories, leading to the development of new theories to explain their unique characteristics and system architectures (e.g. Lin et al., 1996; Tanaka et al., 2002; Morales et al., 2019).

One of the most important open questions in planetary science is to find out if there is another system with a planet that could host life similar to Earth. For this reason, the structure, atmosphere and overall composition of planets is a field of major relevance, and it is directly linked to planet formation and evolution. In particular, the characterisation of hot Jupiters and giant planets has played a critical role in shaping our models of planetary atmospheres and interiors, as their large sizes and short periods make them more accessible to current observational instruments. These gas giants serve as valuable testbeds for developing and validating atmospheric and interior structure models, which can later be applied to smaller, terrestrial planets. Improving our understanding of the interiors of planets as well as their atmospheres can therefore lead to major advances in the search for another Earth (e.g. von Paris et al., 2013; Kaltenegger, 2017).

In this thesis, we use new spectroscopic and photometric data to improve the precision of several planetary parameters and characterise the interiors of selected planets. We apply state-of-the-art models to tackle the challenges behind the retrieval of quantities such as the planet masses and radii as well as the internal structure and composition of rocky planets. We also explore the characterisation of hot giant planets, whose unique location close to the star challenges formation mechanisms and provides important clues about their evolution and interiors (e.g. Helled et al., 2014). The interaction with the star also allows better constraints on stellar physics that can further explain the dynamics of planetary systems (e.g. Maciejewski et al., 2018).

1.1 Overview

The discovery of a Jupiter-sized planet orbiting the 51 Pegasi star by Mayor & Queloz (1995) marked a key breakthrough in the field of planetary science. Ever since the discovery of other planets in the Solar System that the possibility of one day finding another life-hosting planet filled the dreams of astronomers, astrophysicists, and humankind in general. With the discovery and confirmation of the first planet around a solar-type star, planet-related research drastically expanded. The NASA Exoplanet Archive* (Akeson et al., 2013) reports over 5700 confirmed planets orbiting other stars, otherwise known as exoplanets, as of September 2024. These include many different kinds of planets, including some whose properties are not found within the Solar System. 51 Pegasi b, for example, is a Jupiter-sized planet orbiting its host star at only 0.05 AU, which is over 7 times closer than the orbit of Mercury. The idea that a massive Jupiter can exist so close to the star challenged the existing theories behind the formation of planets and led to many new breakthroughs (e.g. Lin et al., 1996; Tanaka et al., 2002).

Figure 1.1 shows the distribution of the confirmed exoplanets in the mass-period diagram as retrieved from the NASA Exoplanet Archive in September 2024. There are two main populations distinguishable in the plot: giant Jupiter-like planets with masses above 100 $M_\oplus$ and smaller planets below that threshold. The latter group can be further classified into Neptune-like planets (between 10 and 100 $M_\oplus$), sub-Neptunes (4-10 $M_\oplus$) and rocky planets with a structure similar to Earth ($< 4\ M_\oplus$). The rapid technological development allowed for an exponential increase in the number of discovered exoplanets, as seen in Figure 1.2. The more precision the instruments are able to get, the easier it becomes to characterise these objects, especially planets near the size of the Earth.

*https://exoplanetarchive.ipac.caltech.edu/

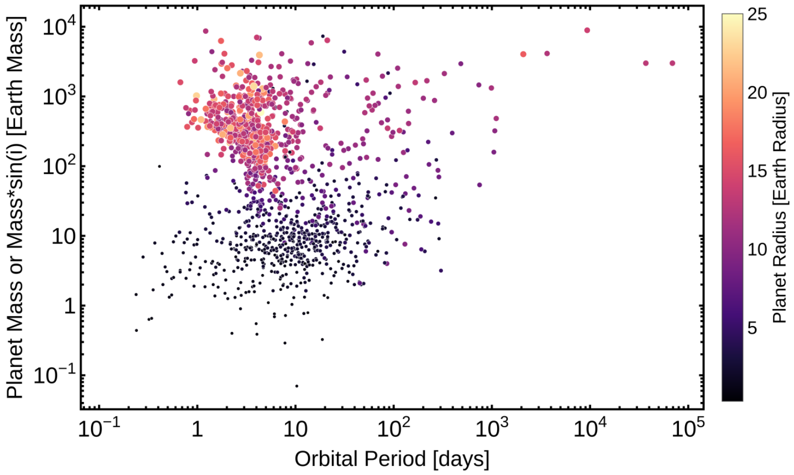

FIGURE 1.1: Distribution of confirmed exoplanets by period, mass and radius, as of September 2024. Figure credit to NASA Exoplanet Archive (Akeson et al., 2013).

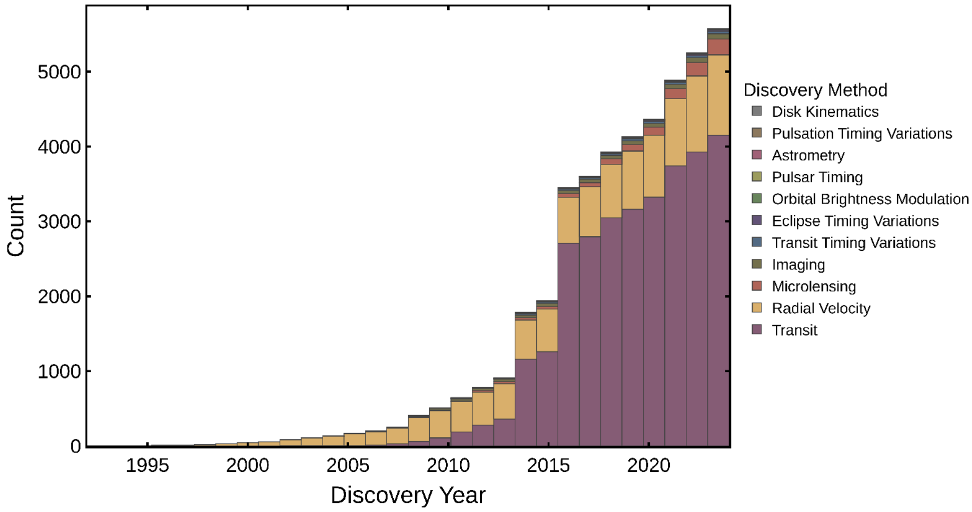

FIGURE 1.2: Cumulative detections of exoplanets by year. Figure credit to NASA Exoplanet Archive (Akeson et al., 2013).

The type of planet being discovered is also heavily influenced by the method used to detect them. There are many different methods to detect exoplanets, but the two most successful ones are the radial velocity (RV) method and the transit method (e.g. Santos et al., 2020, see Figure 1.2), described in more detail in Section 1.3. The RV method utilizes spectroscopic observations of the star, measuring the Doppler shift caused by the wobbling of the star due to the planet's gravity. In contrast, the transit method relies on photometry to detect a decrease in stellar flux, caused by a planet passing across the star's disk along the observer's line of sight. Due to their different physical background, both methods are complementary and are often used simultaneously (e.g. Lillo-Box et al., 2020; Barros et al., 2022a; Rosário et al., 2024). While the radial velocities provide a way to infer the minimum mass of a planet, the transit method allows the estimation of its radius. These two quantities together give the average density of the planet, which is a key parameter to answer the important questions about planetary interiors and composition (Leleu et al., 2021; Egger et al., 2024). For example, a planet of the same mass but a larger radius must have a different composition, either because of a high water content, a large atmospheric envelope or a different unknown composition. The ongoing research behind the internal structure of exoplanets aims to both improve the existing models and tackle the challenges posed by the degeneracies existing between different compositions, which is also impacted by the precision of the density measurements (e.g. Dorn et al., 2015; Dorn et al., 2017; Otegi et al., 2020). The knowledge about the interior of planets is rooted in what is known about the Earth and the other planets in the Solar System, and the ever growing amount of data that is being obtained can soon lead to major developments in the theoretical models and provide even more clues about the nature of many exoplanets, potentially leading to the discovery of an Earth-like planet in the future. As models become more sophisticated and are tested against a wider range of exoplanet types, our capacity to identify truly Earth-like worlds with similar structure, composition, and potential for surface water, becomes significantly more robust (e.g. Acuña et al., 2021; Dorn & Lichtenberg, 2021).

1.2 The radius valley

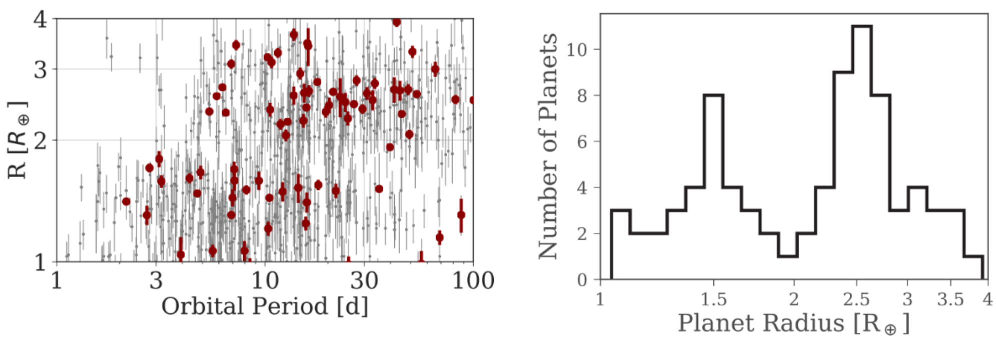

FIGURE 1.3: *Left*: Planet radius as a function of the orbital period. Data points and uncertainties from Fulton et al. (2017) are shown in grey, with the sample used in Van Eylen et al. (2018) in red. *Right*: Histogram of the number of planets in the sample of Van Eylen et al. (2018) as a function of planet radius, showing a bimodal distribution with peaks around 1.5 $R_\oplus$ and 2.5 $R_\oplus$. Figures published originally in Van Eylen et al. (2018).

Among all these newly discovered planets, the majority of them are in the super-Earth ($R_\mathrm{p} = 1 - 2\ R_\oplus$) and sub-Neptune ($R_\mathrm{p} = 2 - 4\ R_\oplus$) regimes (e.g. Batalha, 2014). Super-Earths are defined as planets with a density and composition similar to the Earth but significantly larger, while the sub-Neptunes are volatile-rich planets that are smaller than Neptune. These planets are particularly relevant as they belong to populations that are not present in the Solar System, despite being relatively common within the known exoplanet population (e.g. Mayor et al., 2011; Batalha, 2014).

Using precise radius measurements from Kepler, Fulton et al. (2017) found a bimodal distribution in the radius of the smaller exoplanet population ($1 - 4\ R_{\oplus}$), shown in Figure 1.3. This indicated that planets were more likely to be part of these sub-groups and showed a lack of detections in the range of $1.5 - 2.0\ R_{\oplus}$, which became known as the radius valley or gap. Follow-up studies have confirmed the presence of the bimodal distribution and the location of the gap around $1.9 - 2.0\ R_{\oplus}$ (Van Eylen et al., 2018; Martinez et al., 2019; Petigura, 2020), although it may vary for M-type stars (e.g. Cloutier & Menou, 2020; Bonfanti et al., 2024).

The main mechanisms thought to be behind the formation of this gap are photoevaporation of the atmosphere (e.g. Owen & Wu, 2017; Venturini et al., 2020), core-powered mass-loss (e.g. Ginzburg et al., 2018; Gupta & Schlichting, 2019), gas-poor formation (e.g. Lee & Chiang, 2016), or giant impact erosion (e.g. Liu et al., 2015). Both photoevaporation and core-powered mass-loss models can reproduce the radius valley, however, photoevaporation remains the most widely accepted scenario. Studies have shown that planets located at the second peak of the bimodal distribution are rich in volatiles, indicating that they likely formed beyond the ice line (e.g. Bitsch et al., 2019; Venturini et al., 2020). However, some planets in the first peak may have been initially volatile-rich having lost their volatile content during migration, resulting in their present-day rocky composition (e.g. Van Eylen et al., 2018).

In Chapter 3 of this thesis, we discuss the composition and structure of HD 15337 (Gandolfi et al., 2019; Dumusque et al., 2019), a system containing two planets on opposite sides of the radius valley, making it an excellent laboratory to study the valley and better understand the mechanisms behind its existence.

1.3 Exoplanet detection methods

Figure 1.2 shows a breakdown of confirmed exoplanet detections and the methods used to detect them. As mentioned before, the RV method and the transit method provide the vast majority of the detections and are capable of providing large amounts of information on the planets' orbits and their host star. For those reasons and due to the accessibility of the data, they are also the main methods used in this thesis. In this section we present an introduction to the two methods and how they can be used to detect and characterise exoplanets.

1.3.1 The radial velocity method

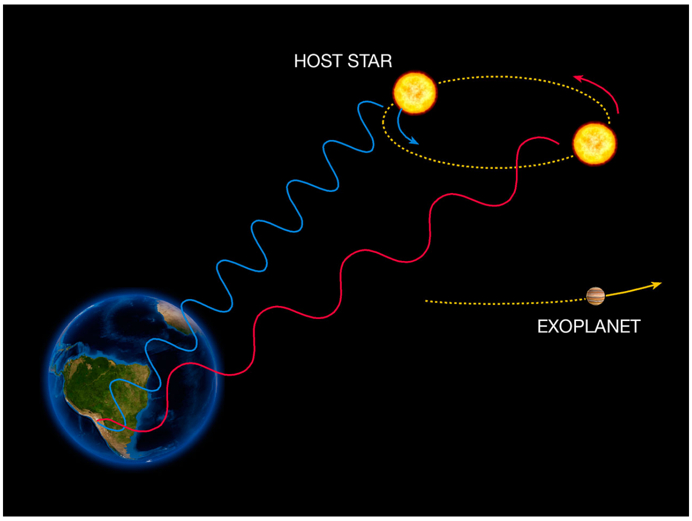

FIGURE 1.4: Schematics of the RV method, where the exoplanet causes a shift in the spectrum. Figure credit to ESO*.

The radial velocity method consists in the use of the stellar radial velocity (RV) variations to infer the presence of an object orbiting the observed star, by means of Doppler spectroscopy (e.g. Baranne et al., 1996; Lovis et al., 2010; Santos et al., 2020). It is based on the theory of gravitation from classical mechanics, which predicts the motion of two gravitationally-bound bodies orbiting each other. According to this theory, the star and the planet both orbit the common center of mass of the system and the planet induces variations in the star's position and velocity that can be seen from the Earth. Due to the Doppler effect, the changes in velocity cause a shift in the spectral lines of the star (e.g. Hearnshaw, 2014). As seen in Figure 1.4, as the star moves away from the observer, the spectrum is shifted towards longer wavelengths (redshift). When moving towards the observer, the spectrum will instead shift towards shorter wavelengths (blueshift). The wavelength shift ($\Delta\lambda$) relative to the rest frame wavelength (λ_0) is equal to the ratio between the radial velocity of the star (V_{r}) and the speed of light (c), according to the equation below for non-relativistic approaches (e.g. Lovis et al., 2010).

*https://www.eso.org/public/ireland/images/eso0722e/

$$\frac{\Delta\lambda}{\lambda} = \frac{V_{\rm r}}{c} \tag{1.1}$$

Following the solution to the gravitational two-body problem in terms of orbital parameters (semi-major axis a, eccentricity e, argument of periastron ω and inclination i), we can relate the velocity in the direction of the observer, given by $V_{\rm r}$, to the mass of the two bodies as a function of those parameters, with the following equation:

$$V_{\rm r} = \sqrt{\frac{G}{(M_\star + M_p)a(1-e^2)}} M_p \sin i \cdot [\cos(\omega + x) + e\cos\omega] \tag{1.2}$$

where x is the true anomaly, G is the universal gravitational constant and $M_\star$ and M_p are the masses of the star and the planet, respectively.

This equation can be used to retrieve the semi-amplitude of the RV signal K, given by equation 1.3, or in more practical units, by equation 1.4, using Kepler's third law of planetary motion to replace a by the period P (e.g. Murray & Correia, 2010; Perryman, 2018).

$$K = \sqrt{\frac{G}{(1-e^2)}} M_p \sin i (M_\star + M_p)^{-1/2} a^{-1/2} \tag{1.3}$$

$$K = \frac{28.4329 \text{ m s}^{-1}}{\sqrt{(1-e^2)}} \frac{M_p \sin i}{M_{\rm Jup}} \left(\frac{M_\star + M_p}{M_\odot}\right)^{-2/3} \left(\frac{P}{1 \text{ yr}}\right)^{-1/3} \tag{1.4}$$

Since the RV method is based on the velocity changes in the line of observation, the RV signal alone is not enough to obtain the mass of the planet. The method is only able to constrain the minimum mass ($M_p \ \sin i$), and therefore a measure of the orbital inclination is necessary to obtain the true mass of the planet.

As seen in equation 1.4, the RV method is sensitive to the mass of the two bodies and to the orbital period and is therefore more suited to find massive planets with shorter orbits. This is the case of 51 Pegasi b, and from there many other close-in giant planets have been found through the RV method. Currently, the challenge lies in detecting the small amplitude signals caused by Earth-mass planets with longer orbital periods that can be inside the habitable zone of solar-like stars, which is the region in the orbit where it is possible for a planet to maintain liquid water at the surface (e.g. Mayor et al., 2011; Santos et al., 2020). To detect such signals on the order of 10 cm s^{-1}, we require highly precise instruments and the ability to reliably eliminate noise from instrumentation and stellar variability. A more detailed discussion of these effects is provided in Section 2.2.

High-precision spectrographs for RVs

Spectroscopic observations of exoplanet hosts have been a major source of new planet candidates and confirmations over the years. The first spectrograph used to detect an exoplanet was ELODIE (Baranne et al., 1996), responsible for the RVs that led to the discovery of 51 Pegasi b (Mayor & Queloz, 1995). The discovery was confirmed soon after by Marcy et al. (1997) using the Hamilton echelle spectrograph located at the Lick Observatory in California, USA (Vogt, 1987).

HIRES (Vogt & Keane, 1993) was another early spectrograph, mounted in the Keck Observatory in Hawaii, USA, in 1996. Shortly thereafter, CORALIE (e.g. Queloz et al., 2000), an enhanced version of ELODIE, was installed by the European Southern Observatory (ESO) in La Silla, Chile, in April 1998. The knowledge obtained from these spectrographs provided many breakthroughs in exoplanetary science, which led to better and more precise instruments over the years, such as the High Accuracy Radial Velocity Planet Searcher (HARPS; Pepe et al., 2002; Mayor et al., 2003).

HARPS is a high-resolution planet-searching spectrograph installed in ESO's 3.6-m telescope at the La Silla Observatory. It has been operating since 2003 and is to date one of the most prolific planet-searching RV instruments. HARPS covers the optical wavelengths of the spectrum, between 378 nm and 691 nm and has an instrumental precision of approximately 1 m s^{-1}. In 2015, the fibres in the HARPS spectrograph were upgraded from circular to octagonal ones (Lo Curto et al., 2015), improving the precision down to to 0.5 m s^{-1}.

Currently, the Echelle SPectrograph for Rocky Exoplanets and Stable Spectroscopic Observations (ESPRESSO; Pepe et al., 2021) is the most precise instrument being used for exoplanet characterisation, being able to achieve an instrumental precision of 10 cm s^{-1}, close to the amplitude of the signal the Earth causes in the Sun's RVs. The NEID spectrograph (Schwab et al., 2016) was also developed recently by NASA and NSF to search for planets orbiting nearby stars, operating at the Kitt Peak National Observatory in Arizona, USA. More recently, the Near Infra Red Planet Searcher (NIRPS, Artigau et al., 2024) was installed at La Silla, Chile, and is observing stars in the near infra-red to complement HARPS observations, focusing on cool M-type dwarf stars.

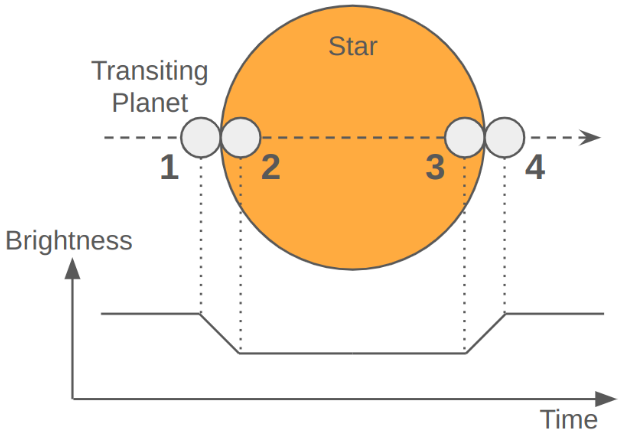

Figure 1.5: Schematics of a planetary transit, with the respective light curve shape below. The transit is defined from the moment the projected area of the planet makes contact with the stellar disc (point 1) to the moment it leaves the disc entirely (point 4).

1.3.2 The transit method

The transit method is responsible for many detections of confirmed exoplanets (see Figure 1.2). A transit is an event where an object passes in front of the star during the observation (e.g. Seager & Mallén-Ornelas, 2003; Santos et al., 2020), effectively decreasing the flux that is detected by the observer (see Figure 1.5, showing the light curve drop during each transit phase). Observing the host star over a period of time allows for the detection of periodic decreases in brightness that can be caused by a transiting planet. The observed fluxes are stored in light curves, which contain the flux measurements as a function of time at a given cadence and can then be used to model the transit event and provide key information about the planets' orbits (e.g. Hellier et al., 2011b; Patra et al., 2020) and features like shape (Correia, 2014; Akinsanmi et al., 2019; Barros et al., 2022b), rings (e.g. Barnes & Fortney, 2004; Akinsanmi et al., 2020) and atmosphere (e.g. Lendl et al., 2020; Demangeon et al., 2024). The planetary radius can be inferred by measuring the transit depth δ, which is the relative reduction in flux during the transit event, but the transit shape depends on many other orbital parameters like the semi-major axis a and the inclination i. The impact parameter, defined as the projected distance between the planet and the star's center at mid-transit and given by the equation $b = a \cos i / R_\star$ (Figure 1.6), can have a strong influence in the light curve shape (Seager & Mallén-Ornelas, 2003).

For $b = 0$ the planet passes directly across the star, blocking the maximum amount of light and creating a symmetric (for circular orbits) and deep U-shaped light curve. As the impact parameter increases, the planet transits in a off-centred line, blocking less light and resulting in a less deep and shorter transit. As b approaches 1, the transit is considered as grazing, as the planet barely crosses the stellar disk, blocking less light due to the limb-darkening effect and creating a V-shaped shallow light curve. The limb darkening effect also affects the shape of the transit in the light curve and has to be modelled to properly obtain the planet properties, affecting especially the ingress and egress phases as the planet transits the darker limb of the star (e.g. Morello et al., 2017; Claret, 2017).

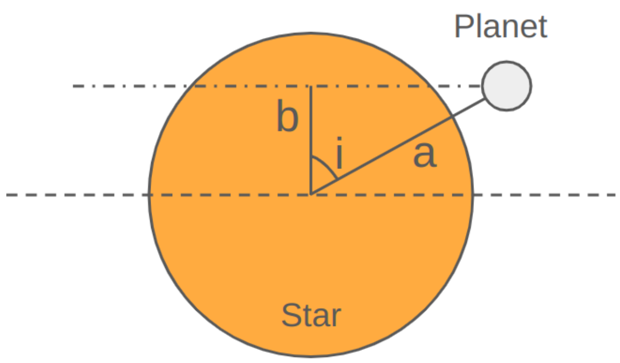

FIGURE 1.6: Diagram outlining the definition of the impact parameter b and its relation to the orbital inclination i and the projected semi-major axis of the orbit a.

The transit shape in the light curve is described by the transit depth, the total transit duration t_T and the duration between the ingress and egress t_F, while the orbital period P can be obtained through the mid-transit times of consecutive transits. The beginning of the transit (point 1 in Figure 1.5) is defined as the moment the planet projection touches the limb of the stellar disc. As the planet continues to move, it will reach a point where the entire planet is in front of the star (point 2). In simple terms, excluding effects like limb darkening and assuming the stellar disc is homogeneous, this marks the end of the ingress phase of the transit and corresponds to the maximum depth of the transit. At point 3, the transit starts the egress phase, as the planet starts to leave the stellar disc, and transit ends at point 4 as the planet leaves the disc entirely and the measured flux is once again unobstructed. The ingress and egress phases are particularly important to obtain precise mid-transit times (e.g. Barros et al., 2013; Rosário et al., 2022; Harre et al., 2023) and allow the accurate modelling of the limb-darkening effect. They can also be used to detect several planetary features like rings that can cause small variations in this part of the transit (e.g. Simon et al., 2015; Akinsanmi et al., 2020).

Derivation of system parameters

The observable quantities described before (δ, t_T, t_F and P) can be used to retrieve several physical parameters from the observed system. When modelling transits, it is common to use alternative parametrisations like the ones available in the `batman` code (Kreidberg, 2015), which facilitate the extraction of these parameters. Assuming the planet has a spherical shape, we can immediately derive the relationship between the depth and the planet-star radius ratio $R_\mathrm{p}/R_\star$ with equation 1.5. Although these relationships cannot be expressed analytically in a general case, Seager & Mallén-Ornelas (2003) derived analytical solutions for the scaled semi-major axis $a/R_\star$ and the impact parameter b in a circular orbit. The impact parameter is given by equations 1.6 and 1.7, respectively. These quantities can also be used together to obtain the orbital inclination i. We note that the mentioned equations do not take into account the effect of the limb darkening, which will be addressed later in Section 2.1.3.

$$\delta \sim \left(\frac{R_\mathrm{p}}{R_\star}\right)^2 \tag{1.5}$$

$$\frac{a}{R_\star} = \left\{\frac{(1+\sqrt{\delta})^2 - b^2[1-\sin^2(t_T\pi/P)]}{sin^2(t_T\pi/P)}\right\}^{1/2} \tag{1.6}$$

$$b = \frac{a}{R_\star}\cos i = \left\{\frac{(1-\sqrt{\delta})^2 - [\sin^2(t_F\pi/P)/\sin^2(t_T\pi/P)](1+\sqrt{\delta})^2}{1-\sin^2(t_F\pi/P)/\sin^2(t_T\pi/P)}\right\}^{1/2} \tag{1.7}$$

Lastly, with Kepler's third law (equation 1.8), it is possible to obtain the stellar density $\rho_\star$, under the assumption that $M_\mathrm{p} \ll M_\star$, from equation 1.9 below, where G is the gravitational constant.

$$P^2 = \frac{4\pi^2 a^3}{G(M_\star + M_\mathrm{p})} \tag{1.8}$$

$$\rho_\star = \frac{3M_\star}{4\pi R_\star^3} = \frac{3\pi}{GP^2}\left(\frac{a}{R_\star}\right)^3 \tag{1.9}$$

As the depth is related to the relative radius, it is sensitive to the size of the star and the planet. Therefore, the transit method is more suited to search for large planets, especially if they are orbiting close to the star, making them more likely to be detected during observations. The probability of a transit can in fact be calculated using equation

1.10 (see Perryman, 2018), further showing the dependence with the planet size and orbital distance. Planets in eccentric orbits are also more likely to transit their host stars due to the dependence on $(1-e^2)$. These dependencies have to be taken into account when making population studies based on transits as they may introduce detection biases, making some planets appear more common than they are in reality.

$$P_{\text{transit}} = \left(\frac{R_\star \pm R_p}{a}\right)\left(\frac{1}{1-e^2}\right) \tag{1.10}$$

Transit-focused missions

The first planet observed via photometry using the transit method was HD 209458 b (Charbonneau et al., 1999), a 3.5-day period hot Jupiter previously detected via the RV method. Following transit observations from the Hubble Space Telescope (HST, Brown et al., 2001) allowed for an estimation of the radius (around 1.27 R_{Jup}) and for the confirmation of the planetary nature of the object. Follow-up observations of planet candidates from RV surveys using space-based photometry resulted in numerous confirmed planets and paved the way for dedicated missions focused on detecting exoplanets through transit photometry. Launched in 2006 by CNES/ESA, the CoRoT mission (Auvergne et al., 2009) was the first telescope specifically dedicated to exoplanet detection. It marked a significant breakthrough by discovering the first super-Earth-sized planets. Among many discovered new worlds, CoRoT 7b (Léger et al., 2009) was the first super-Earth to have a measured radius. In 2009, NASA launched the Kepler mission (Borucki et al., 2010) designed to survey a large amount of stars searching for new exoplanets. Between 2009 and 2013, when the second of its four reaction wheels failed, Kepler was responsible for the discovery of thousands of planetary candidates, many of which were super-Earths and sub-Neptunes, paving the ground for major discoveries in the field of extrasolar rocky planet size and composition. Following the reaction wheel failure, the mission was redesigned and renamed K2 (Howell et al., 2014), operating until the exhaustion of its fuel reserves in 2018. Kepler and K2 are credited with the discovery of over 2700 confirmed planets according to the NASA Exoplanet Archive as of September 2024.

The TESS mission

In 2018, NASA launched the Transiting Exoplanet Survey Satellite (TESS; Ricker et al., 2015), a new improved space mission aimed at the search for exoplanets using the transit method. It marked another major milestone in exoplanet search, with thousands of planet candidates found and over 500 confirmed planets as of September 2024. The TESS mission uses four red-sensitive wide-field cameras to cover about 85% of the sky, making it the widest planet-focused survey to date and massively growing the number of observed transit events that led to planet candidates and TESS objects of interest (TOIs).

The TESS mission was originally planned for two years, but has since been extended twice and a third extension is being planned for 2025. Each mission divides the sky into sectors, each covering a strip of 24° x 96°, observing the southern ecliptic hemisphere in year 1 and the northern hemisphere in year 2 (see Figure 1.7). The first extended mission in years 3 and 4 re-observed the southern hemisphere and a part of the original sectors in the northern one, while the second extension, planned to end in 2025, is currently re-observing both hemispheres after a shift in the pointing of the spacecraft allowed it to observe parts of the sky not covered in the first two missions. TESS predominantly observed in a 2-min cadence in the original mission, but in the extended mission several targets were added to be observed at a 20-second cadence.

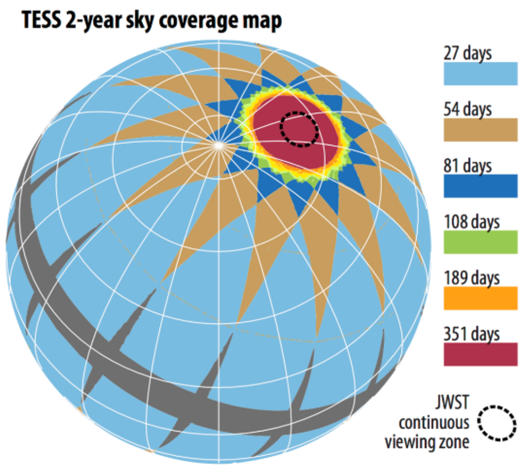

Figure 1.7: TESS 2-year sky observation map. Image courtesy: TESS/MIT*

The CHEOPS mission

The CHaracterising ExOPlanet Satellite (CHEOPS; Benz et al., 2021) is a space telescope launched by ESA in 2019, which is designed as a follow-up mission for the precise characterisation of exoplanets orbiting around bright stars. Its main objective is to use high precision transit photometry to improve the constrains in the radius of super-Earth and

*https://tess.mit.edu/science/observations/

sub-Neptune planets with already determined masses, further enhancing the prospects of characterising the interiors and atmospheres of rocky planets.

Contrary to the TESS survey which observes large areas of the sky for a long time, the follow-up nature of the CHEOPS observations allows it to focus on specific targets with known transit timings. The higher precision of the CHEOPS measurements also makes it suitable to observe entire phase-curves that can be used to characterise atmospheres (e.g. Demangeon et al., 2024) and the ingress and egress regions that can be used to detect moons and rings around exoplanets (e.g. Simon et al., 2015; Akinsanmi et al., 2020).

The mission was concluded successfully in 2023 and since then it has been extended with a renewed focus on following up previous transit and RV observations. The extended mission is expected to finish in 2026 with a further extension possible until 2029.

1.3.3 Future missions

Following the success of TESS and CHEOPS as transit-focused missions, a new mission is being planned and developed by ESA. The PLAnetary Transits and Oscillations of stars (PLATO; Rauer et al., 2024) mission is planned to launch in 2026 and will focus on searching for transits of planets in the habitable zone of their star. The mission's scientific objectives primarily focus on stars and planets. A key goal in planetary science is to determine the bulk properties of planets orbiting F-K dwarf and sub-giant stars, with an expected radius precision of 3% for an Earth-sized planet around a magnitude 10 star (Rauer et al., 2024). Another major objective is to study the formation and evolution of planetary systems, including system architecture and the relationship between planet formation and stellar properties. The mission is expected to provide many important results following up on the path paved by TESS and CHEOPS in recent years.

The James Webb Space Telescope (JWST; Gardner et al., 2006) was launched in 2021 as a joint collaboration between NASA, ESA and CSA and is also expected to provide significant contributions to planet characterisation through infrared transit spectroscopy. JWST will enable science cases ranging from cosmology and galaxy formation to stellar characterisation and exoplanet atmospheres. Finally, the Atmospheric Remote-sensing Infrared Exoplanet Large-survey (ARIEL; Tinetti et al., 2018) is planned for 2029 as well and is expected to study the atmosphere of over 1000 exoplanets orbiting distant stars, focusing on warm and hot planets. Providing new clues about the atmosphere elemental composition is one of the main science cases of the mission, but atmosphere evolution and other science cases like planet migration are also part of the mission objectives.

1.4 Planet interiors and composition

The main focus of this thesis is to improve the interior characterisation of exoplanets and study the methods and models used to estimate their structure and composition.

The most common approach to study the interior of small rocky planets consists in building computational models to calculate the mass-radius relationship of synthetic planets based on previously defined equations of state (EOS), which are in turn based on the existing knowledge of the interior of the Earth (Valencia et al., 2006; Fortney et al., 2007; Valencia et al., 2007a; Seager et al., 2007; Grasset et al., 2009; Zeng & Sasselov, 2013; Zeng et al., 2016). For example, the model of Zeng et al. (2016) derives an empirical relationship between mass and radius based on the Preliminary Reference Earth Model (PREM; Dziewonski & Anderson, 1981), which is a seismically derived model of the Earth's density distribution. Zeng et al. (2016) extrapolate the PREM to build the EOS for mantle and core, valid for planets with masses between 1 and 8 $M_{\oplus}$. The model developed in Dorn et al. (2015) and Dorn et al. (2017), on the other hand, computes the structure and composition of the planet using the EOS of the different layers (core, mantle, water and gas) and applies a Bayesian inference method to obtain the posterior distribution of composition and radius of each layer. While these have shown promising results and have been used as a baseline for internal structure modelling (e.g. Leleu et al., 2021; Delrez et al., 2021), the observed mass and radius of an exoplanet can be explained by several different interior structures and compositions. This creates a degeneracy problem that is further enhanced if the mass and radius obtained from the observations have a large associated error (e.g. Valencia et al., 2007b; Zeng & Seager, 2008; Rogers & Seager, 2010).

One suggested approach to attempt to reduce the degeneracy of the problem is to assume the planet's abundances are the same as the star (e.g. Brugger et al., 2017; Unterborn et al., 2023), as they are all formed from the same initial material. This helps constraining the possible combinations of layers and composition in some cases, but while most models assume the same abundances, it has been shown in Adibekyan et al. (2021) that the relationship is not always a 1:1 linear correlation and that this assumption may lead to inaccurate results.

The forward approach taken in these models does not allow for the quantification of the degeneracy and it is not straightforward to understand which model parameters are most affected by it. In recent years, several models have been developed that add a retrieval layer on top of the forward model and perform a Bayesian analysis that can provide the posterior probability distribution of each parameter (e.g. Dorn et al., 2017; Acuña et al., 2021; Leleu et al., 2021; Haldemann et al., 2024). Baumeister et al. (2020) explores the use of machine learning algorithms for the retrieval layer and uses mixture density neural networks (MDN) to characterise the interiors of low mass planets. This approach is further explored in Haldemann et al. (2023) and Egger et al. (2024), which presents a new state-of-the-art code that expands the neural networks to the entire Bayesian framework allowing for changes in priors and in the inference methods.

Another inherent problem in most models is that they are based on the structure of the Earth and assume clear distinct layers (core, mantle, water and atmosphere), which is not always true considering the extreme conditions some exoplanets are in. Dorn & Lichtenberg (2021) explore the possibility of water being mixed in the mantle for high-temperature planets, and expand on their previous model (Dorn et al., 2017) by adding a mixing layer, finding significant differences in the estimated radius with this new approach. Acuña et al. (2021) also includes a multiphase water layer (considering steam, supercritical, and condensed phases) in the model of Dorn et al. (2017) in an attempt to improve the modelling of the individual layers.

Despite major improvements in the precision and volume of data from the latest telescopes and spectrographs, models still have significant limitations and numerous unknown factors that influence the results. Overcoming these modelling challenges and resolving their inherent degeneracies is essential for understanding the interiors of rocky planets and identifying another Earth-like world.

1.5 Planet-star interaction

The methods described before are very favourable for rocky planets since the structure and composition of the Earth can be used as a proxy for the models, which contain essentially two main layers: core and mantle. However, the same can not be said about giant planets, especially hot Jupiters, as they possess significant differences in structure and evolution history. On the other hand, hot Jupiters are excellent laboratories for studying the planet-star interaction due to their proximity to the host star. In particular, these planets orbit so close to the star that they experience very strong tidal forces which can lead to perturbations in their orbits (e.g. Ogilvie, 2014) as well as their shape (e.g. Chandrasekhar, 1987; Correia & Rodriguez, 2013). The tides cause small bulges in both the star and the planet, which then cause torques. These torques lead to energy dissipation in the star's interior which causes an inward spiralling of the planet's orbit and a loss of energy from the system, shrinking the orbital period and resulting in the planet's engulfment by the star (Ogilvie, 2014). This process of orbit shrinkage is commonly known as tidal decay, and its timescale depends on the orbital period and on the energy dissipation due to the tides.

Tidal quality parameter

The stellar tidal quality parameter ($Q_\star$), is a dimensionless quantity that measures the efficiency of tidal dissipation in a system (Goldreich & Soter, 1966). For convenience, we use the parametrisation given by equation 1.11 (Ogilvie & Lin, 2007), which calculates the modified tidal quality factor $Q'_\star$ and relates the tidal dissipation to the second-order stellar Love number $k_{2,\star}$:

$$Q'_\star = \frac{3Q_\star}{2k_{2,\star}} \tag{1.11}$$

This parameter is tied to the dissipation of energy due to tidal interactions, including orbit circularisation, which is the transition from an eccentric to a circular orbit for very short periods, and period decay. Meibom & Mathieu (2005) provide a wide study of circularisation periods in binaries that led to a range of $10^6 - 10^7$ for the tidal quality parameter, which is also consistent with the study from Ogilvie & Lin (2007). It is thought that hot Jupiters could have a weaker tidal decay and be in a different tidal regime (Ogilvie & Lin, 2007), which would explain the longer decay timescale and the survival of very close orbits for long periods of time. A more precise and accurate measurement of $Q_\star$ would be a significant contribution to understanding the different tidal dissipation regimes and add further clues to planet-star interactions (e.g. Ogilvie, 2014; Weinberg et al., 2023).

Tidal decay and change in period

The rate at which a planet decays, given by the derivative of its orbital period over time $\dot{P}$, is strongly related to the tidal dissipation efficiency and therefore to the $Q'_\star$ parameter. Starting from the equations of Goldreich & Soter (1966) which provide the basis for the mathematical expressions used to define $Q'_\star$, we can derive a relationship in the following form (e.g. Maciejewski et al., 2018, 2020):

$$Q'_\star = -\frac{27}{2}\pi \left(\frac{M_\mathrm{p}}{M_\star}\right)\left(\frac{a}{R_\star}\right)^{-5} \dot{P}^{-1} \tag{1.12}$$

This relationship shows a strong dependence on the scaled semi-major axis $a/R_\star$ and the planet-star mass ratio $M_\mathrm{p}/M_\star$, which are observable parameters that can be used to identify potential hot Jupiters with decaying orbits.

Furthermore, we can also derive an expression that gives the infall (or inspiral) timescale of the planet, that is, the time it would take for the planet to be engulfed by the star, given the rate of decay of the system. From Ogilvie & Lin (2007), we obtain:

$$\tau_a = \frac{P}{\dot{P}} = P\frac{2Q'_\star}{27\pi}\left(\frac{M_\star}{M_\mathrm{p}}\right)\left(\frac{a}{R_\star}\right)^5 \tag{1.13}$$

Tidal deformation

The shrinkage of the orbit is not the only consequence of the strong tidal forces on close-in planets. In the case of massive planets with large gas envelopes, the gravitational pull of the star and the tidal forces between the two bodies cause a deformation of the planet's spherical shape (e.g. Chandrasekhar, 1987; Correia & Rodriguez, 2013). This effect of tidal deformation mostly depends on the planet's size: the larger the planet, the more prominent the deformation is. This deformation produces a detectable signature in a planet's transit light curve (e.g. Seager & Hui, 2002; Carter & Winn, 2010; Correia, 2014; Akinsanmi et al., 2019; Barros et al., 2022b), which affects the ingress, egress and the duration of the transit. Correia (2014) proposes an analytical model capable of calculating the projected area of the planet seen during a transit, and estimates the shape of the light curve based on this deformation at any point of the transit. The general shape can be described by equation 1.14 (Correia, 2014), with (a, b, c) representing the semi-principal axes in the (X, Y, Z) coordinate system according to Figure 1.8 (Akinsanmi et al., 2019).

$$\frac{X^2}{a^2} + \frac{Y^2}{y^2} + \frac{Z^2}{c^2} = 1 \tag{1.14}$$

Quantifying the tidal deformation is particularly interesting because it can be related to the planet structure and to its second-order Love number (k_2, Love, 1909, see Section 5.1). This number is effectively a measure of the response of a body to an external perturbation, such as tidal forces, and it can be used to measure the level of differentiation of the interior

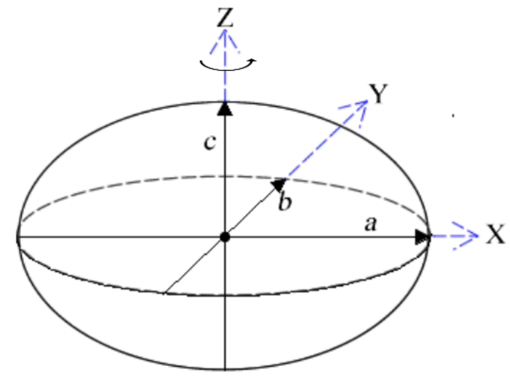

FIGURE 1.8: Schematics of the triaxial ellipsoid in the (X, Y, Z) coordinate system, showing the principal axes (a, b, c). Positive X-axis pointing towards the star. Figure published originally in Akinsanmi et al. (2019).

of the planet and the concentration of heavy elements in the core relative to the envelope (Correia, 2014). Under a perturbing potential V_p, the radial displacement ΔR can be described by equation 1.15 below

$$\Delta R = -h_2 V_p / g \tag{1.15}$$

where g is the average surface gravity of the planet and h_2 is the Love number for displacement, which is related to k_2 by:

$$h_2 = 1 + k_2 \tag{1.16}$$

Using the formulation of Correia & Rodriguez (2013) for the perturbing potential, Correia (2014) derives a relationship between the three semi-principal axes through an asymmetry parameter q, which effectively measures the difference between each axis (equations 1.17 and 1.18).

$$a = b(1 + 3q) \tag{1.17}$$

$$c = b(1 - q) \tag{1.18}$$

$$q = \frac{h_2}{2} \frac{M_\star}{M_p} \frac{R_v}{r_0} \tag{1.19}$$

As seen in equation 1.19 (Akinsanmi et al., 2019), q is proportional to h_2, the mass ratio $M_\star/M_p$ and the R_v/r_0 ratio. R_v is the radius of a sphere with the same volume as the ellipsoid, so that $R_v = (abc)^{1/3}$, whereas r_0 is the orbital radius assuming a circularised orbit.

Figure 1.9, originally from Correia (2014), shows the effect of the deformed shape in the light curve, with the residuals showing the difference between the ellipsoid model and the spherical model. The light curve is influenced by two main effects. The first affects the ingress and egress, causing flux oscillations due to the planet's ellipsoidal deformation (Seager & Hui, 2002). The second, identified by Correia (2014), results in a flux increase throughout the transit, particularly at mid-transit, driven by the planet's rotation as it moves across the star. Due to the star's gravitational pull, the planet is stretched along the direction of the star, creating a tidal distortion. At the midpoint of the transit, the planet's X-axis aligns with the observer's line of sight, reducing the projected area and consequently decreasing the amount of stellar light blocked by the planet. The effect of the deformed shape is higher for edge-on orbits with $i = 90°$ as the transit is longer and the changes in the light curves are more prominent and differentiated (Correia, 2014).

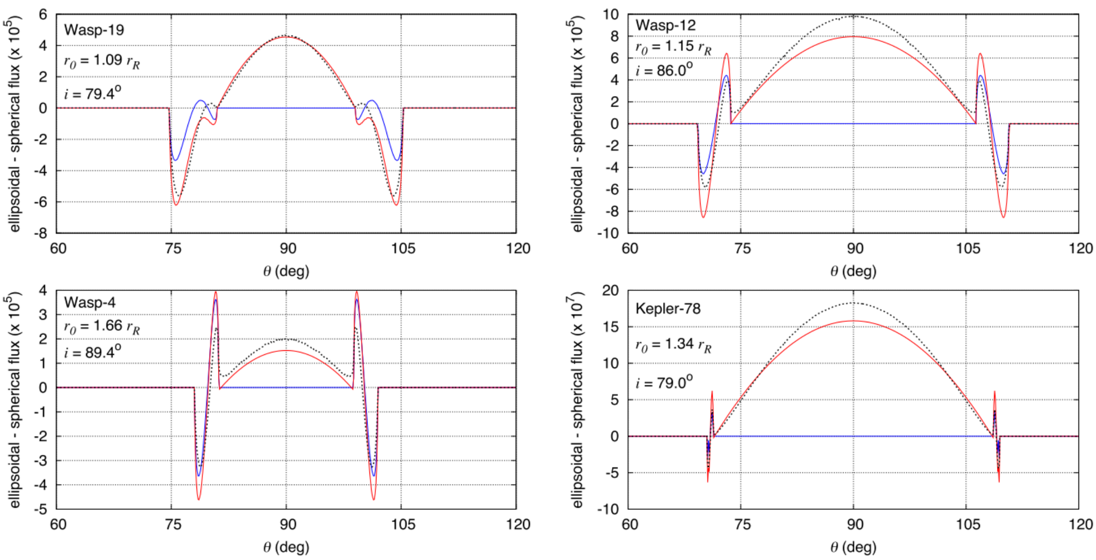

FIGURE 1.9: Difference between the transit light curves of an ellipsoidal and a spherical planet for different orbital inclinations. The red line shows the difference using the analytical model of Correia (2014), while the blue is obtained for a simple oblate planet. The dashed line is the same as the red line but using a quadratic limb-darkening model as well. Figure published originally in Correia (2014).

Tidal deformation from transit light curves was first detected within the 99.7% confidence interval for WASP-103b (Barros et al., 2022b), followed by WASP-12b (Akinsanmi et al., 2024), among other potential candidates. While these detections allow for the calculation of the Love number, a more precise determination of h_2 introduces a new input variable in the interior structure models, paving the way for a better interior characterisation. New and more precise data from CHEOPS, PLATO and JWST are expected to improve the detection of tidal deformation in hot Jupiters and place new constrains on their Love number and internal structure.

1.6 Thesis summary

In this thesis we focus on the methods and models used to characterise both rocky and giant exoplanets, from their orbits to their interior and atmosphere.

We first introduce all the methods used from the light curve analysis to the detection of orbital decay in Chapter 2. Next, in Chapter 3, we present the analysis performed for the HD 15337 system, a system with two small planets spanning the radius valley, where we use a joint transit and radial velocity analysis to refine the planetary parameters and provide updated constrains on the internal structure of the planets. We use photometric data from the TESS and CHEOPS telescopes as well as radial velocities obtained with HARPS, together with state-of-the-art modelling in both the joint analysis and the internal structure analysis.

In Chapter 4, we present an analysis of the orbital decay of two hot-Jupiters, WASP-18b and WASP-19b, known to be some of the most promising targets for this type of study. We use TESS transit data obtained over several years to update the orbital parameters and attempt to detect a period change that would indicate the presence of decay due to tidal forces.

In Chapter 5, we present our ongoing research where we investigate the relationship between the second-order Love number and the core mass fraction of hot Jupiters. We showcase the relationship using a simple analytical model and attempt to reproduce the results with a more complete model using the MESA evolution code. We present the challenges faced and future prospects tying our work to future detections of tidal deformation and measurements of the Love number.

Finally, in Chapter 6 we present a summary of the thesis as well as the future prospects for each part of our work, highlighting contributions from future missions such as PLATO and the potential for improvement in our Love number model.

Chapter 2

Characterising exoplanets

In this chapter, we describe the methods and models used to analyse transit light curves and radial velocity data and how the results can be used to further characterise both giant and rocky exoplanets.

2.1 Analysis of transit light curves

We analyse transit light curves from TESS and CHEOPS to determine the planet's radius and refine constraints on its internal structure. Additionally, we derive precise transit timings to investigate potential transit timing variations (TTV) and period changes, which may indicate orbital perturbations. The light curve is a measure of the flux of a star and its uncertainty as a function of time. In the case of TESS, the light curves we use in our work have a cadence of 2 minutes, while the CHEOPS ones have a cadence of roughly 38 seconds.

The observed flux comprises multiple components: the stellar flux (including stellar variability), the planetary flux, instrumental noise and systematics and other astrophysical contaminants. When analysing a light curve it is necessary to separate each signal and reduce the noise in order to obtain a clean transit of the planet. In this section, we discuss the effect of stellar activity in the light curve, the techniques used to mitigate it, and the data preprocessing steps.

2.1.1 Effect of stellar variability

As we know from decades of observing the Sun, stars are hosts to a number of physical phenomena that affect their brightness, such as granulation, spots, flares, differential rotation and oscillations (e.g. He et al., 2015; Mehrabi et al., 2017; Zaleski et al., 2019). Spots, for example, can cause a temporary reduction of the measured flux that impacts the estimation of the transit depth (e.g. Oshagh et al., 2013) if the planet transits the active regions. This effect is especially noticeable when comparing observations at different points in time. In a similar manner, faculae can temporarily increase the brightness of the star and produce inaccuracies in the transit measurement (e.g. Mehrabi et al., 2017). Granulation, oscillations and the star's magnetic cycle might affect the retrieval of accurate transit parameters by causing periodic signals on short- or long-term scales. For instance, variations due to stellar granulation can reach approximately 75 ppm, which is comparable to the estimated transit depth of an Earth-sized planet orbiting a Sun-like star (Gilliland et al., 2011), with timescales from several minutes to more than one day in case of supergranulation (Hirzberger et al., 2008; Priest, 2014).

To mitigate the impact of stellar activity and spot-crossing events in TESS light curves, we apply a method based on the moving filter algorithm (e.g. Charbonneau et al., 2009; Burke et al., 2014; Shporer et al., 2019), followed by polynomial detrending, which is described in detail in Section 2.1.2. Alternatively, Gaussian processes (GPs, Section 2.2.4) have been extensively used to model the activity effect and other sources of noise with good success (e.g. Grunblatt et al., 2017; Serrano et al., 2018). Other techniques, such as basis splines, have also been successfully implemented for detrending light curves (e.g. Mayo et al., 2018; Rice et al., 2019; Barros et al., 2020). A more detailed discussion of these methods can be found in Hippke et al. (2019).

2.1.2 Pre-processing the light curves

When accessing the measured flux, the data are initially reduced to provide a clean measurement that can be used to search for transits. In this section, we briefly describe the method used to pre-process the light curves of TESS and CHEOPS before the analysis to ensure an accurate derivation of the required parameters.

2.1.2.1 TESS

The photometric data from TESS observations used in this work were reduced by the Science Processing Operations Center (SPOC; Jenkins, 2020) pipeline and released to the public through the Mikulski Archive for Space Telescopes (MAST) portal*.

Two types of flux data are stored in the light curve files. The Simple Aperture Photometry (SAP) flux is calculated by simply summing together the brightness of pixels located within the defined aperture. As it is a direct extraction from the observed brightness it is subject to instrumental systematics. The Presearch Data Conditioning SAP (PDCSAP) light curves are corrected to remove these effects, the instrumental systematics, the outliers, discontinuities, contamination from nearby stars and the fact that the aperture doesn't encapsulate all the flux from the target. The contamination can be accessed via the CROWDSAP keyword in the light curve files, which provides an estimation of the level of contamination within the aperture relative to the measured flux. The aperture correction is accessible via the FLFRCSAP keyword, which gives the flux of the target object that is outside the aperture. We use the PDCSAP light curves throughout this thesis, as they are specifically generated for planet searching (Smith et al., 2012; Stumpe et al., 2014) and as such provide cleaner data for that purpose.

The light curves reduced by the SPOC pipeline also include a quality parameter for each measurement that is used to identify data points that have been impacted by abnormal occurrences, for example, attitude changes, momentum dumps, or thruster firings (Tenenbaum & Jenkins, 2018). This parameter is set to a number corresponding to the anomaly, and to zero if the measurement is unaffected by known events. To enhance data reliability, we excluded all non-zero quality data points and any NaN values from the light curve before detrending and processing the data.

Mitigating stellar activity signals is particularly important for TESS, as its long observation periods make it sensitive to fluctuations inherent to the activity cycles of the star. Assuming that stellar spots are the main contributor to the photometric modulation of the star, the highest measured flux corresponds to the least stellar activity (i.e., fewer spots). Therefore, we use this value as a reference to normalise all light curves relative to the 'clean' flux.

To extract the maximum, we first apply a moving median filter (spanning 32 points) to smooth the light curves and remove local outliers. We then identify the highest flux value

*https://mast.stsci.edu/.

from the filtered curve. An example can be seen in Figure 2.1, which shows the light curve of WASP-18 from the sector 2 of TESS (see chapter 4 for the details of this work). The highest flux value from the median-filtered light curves (marked as a blue point in Figure 2.1) serves as the normalisation constant. This way, we take into account the fact that different observations at different times correspond to different phases of the activity cycle, reducing the risk of observing during a particularly high activity period and introducing biases, instead keeping all relative fluxes consistent.

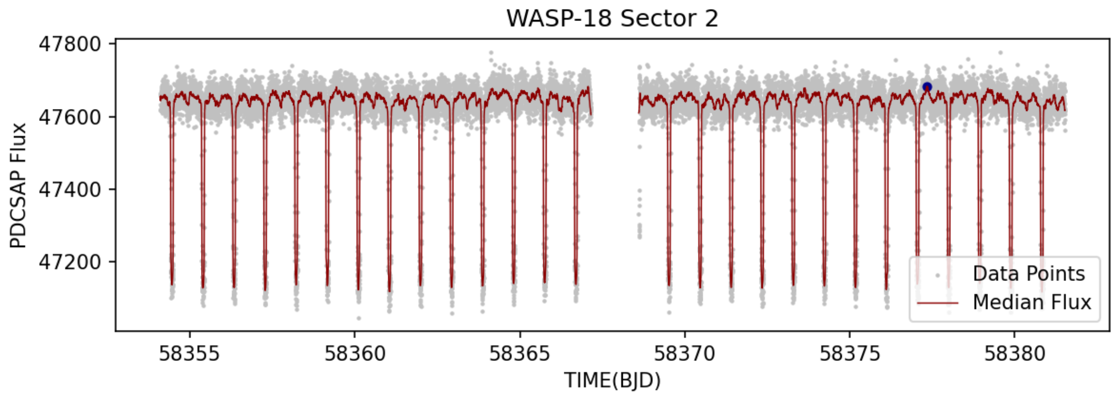

FIGURE 2.1: Plot of the PDC light curves of WASP-18 with NaNs and quality flagged points removed with the moving median filter shown in red and the maximum value highlighted in blue.

The normalised curves are then divided into individual transits by selecting all points within three transit durations of the mid-transit time, removing the remaining out-of-transit data between segments. This approach reduces the volume of data to be processed and eliminates long-term trends, while still capturing short-term variations. For each transit light curve, a low-order polynomial model is applied to account for these short-term trends. Most transits favour a first-order polynomial according to the BIC, while some favour a second-order polynomial. We then perform a uniform shift of the individual light curves by setting the average out-of-transit flux to 1 and detrend using the fitted polynomials to correct any remaining trends. Figure 2.2 illustrates this process, showing the first transit of WASP-18b before and after normalisation. This approach is used to pre-process the TESS data in chapters 3 and 4 and was used in the works published in Rosário et al. (2022) and Rosário et al. (2024).

An alternative approach to this pre-processing would be fitting a GP to the out-of-transit data without separating the light curves (see Section 2.2.4). However, at the time of this analysis, the implementation of this approach was not optimised to run with the

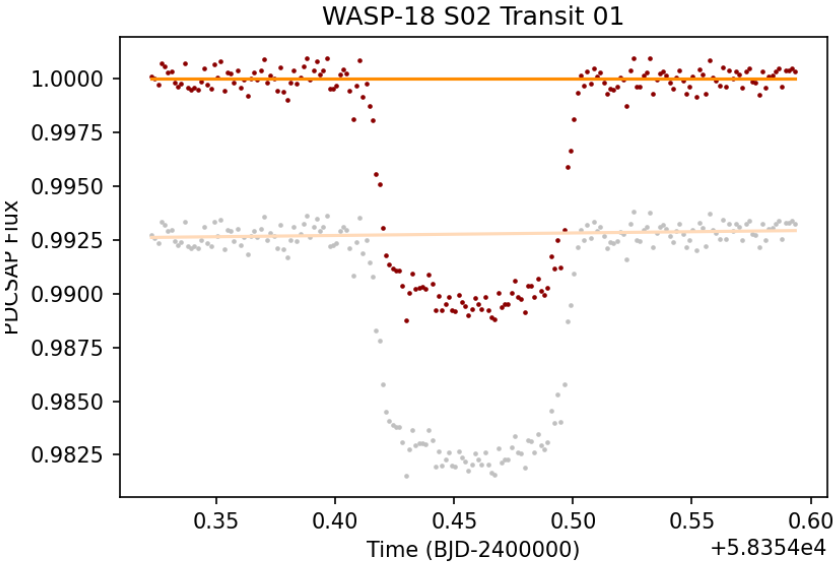

Figure 2.2: Example plot of the first transit of WASP-18b in sector 2 of TESS. The normalised values are shown in a darker color.

high amount of data points. Another possibility to mitigate computational costs without losing the out-of-transit data would be the binning of those data points, since the stellar activity time scales are much longer than the duration of a transit.

2.1.2.2 CHEOPS

CHEOPS data are available through the Data and Analysis Center for Exoplanets (DACE) and the CHEOPS mission archive*. The data are processed using the CHEOPS data reduction pipeline† (DRP; Hoyer et al., 2020), whose calibration process removes the bias from reading electronics and corrects for image gain, dark current effects and non-uniform pixel response. It further corrects the light curves for environmental effects, including background contamination, smearing and cosmic ray impacts. The corrected light curves are available in different aperture radii, ranging from 15 to 40 pix in steps of 1 pixel, with 33 pix corresponding to the default aperture. The light curve files produced by the DRP include the time of the observation, the flux measurement and also the roll angle time series, quality flags, and the background time series used for the corrections.

In this work we use the publicly available code `pycheops` (Maxted et al., 2022) to perform a preliminary cleaning of the CHEOPS data. We retrieve the light curves from

*https://cheops-archive.astro.unige.ch/archive_browser/
†DRP version 13

DACE using `pycheops` with the `decontaminate` setting enabled, which removes flux contributions from background stars. To eliminate outliers, we apply a 5σ clipping, where σ is defined as the mean absolute deviation from a median-smoothed light curve. The process of detrending the light curves varies depending on the data. Therefore, in Section 3.4.1, we provide a detailed explanation of the detrending model applied to HD 15337.

2.1.3 The limb darkening effect

One of the main phenomena seen in transit light curves is limb darkening. Stellar limb darkening is a variation of the stellar disc brightness from the centre to the limb. At the centre, where the brightness is the highest, the observer is seeing the photons emitted by the deeper and hotter layers of the photosphere. At the limb, only the cooler layers are seen, which emit less light and appear darker to the observer (see Figure 2.3).

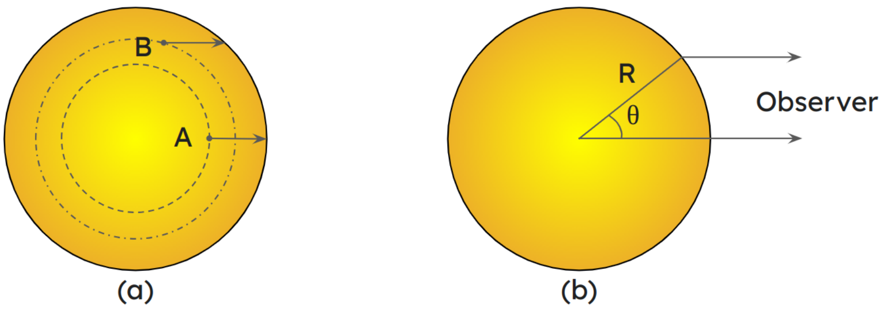

FIGURE 2.3: *Left:* Schematics of the limb-darkening effect. Photons emitted from layer A are unable to escape from the star near the limb. The photons that escape from layer B are less bright, and lead to the darkening seen by the observer. *Right:* Definition of the limb-darkening angle that defines the limb-darkening profile.

This effect causes the transit to appear deeper at mid-transit, since the planet is blocking the brightest part of the stellar disc (see Figure 2.4). As the limb darkening affects the shape of the transit, it becomes crucial to assess it accurately during the transit modelling.

The limb darkening can be modelled by several different laws, which aim to represent the limb-darkening profile as a function of θ, the angle between the line of the observer and the normal to the stellar surface (see Figure 2.3). These laws introduce a small set of parameters, the limb-darkening coefficients, that are dependent on the stellar properties and are usually included in the transit modelling. Some examples of limb-darkening models are the linear law (Milne, 1921), the quadratic law (Kopal, 1950; Mandel & Agol, 2002), the power-2 law (Hestroffer, 1997; Maxted, 2018) and the non-linear or four-parameter law (Claret, 2000). In this work we will use the quadratic law for both TESS and CHEOPS as

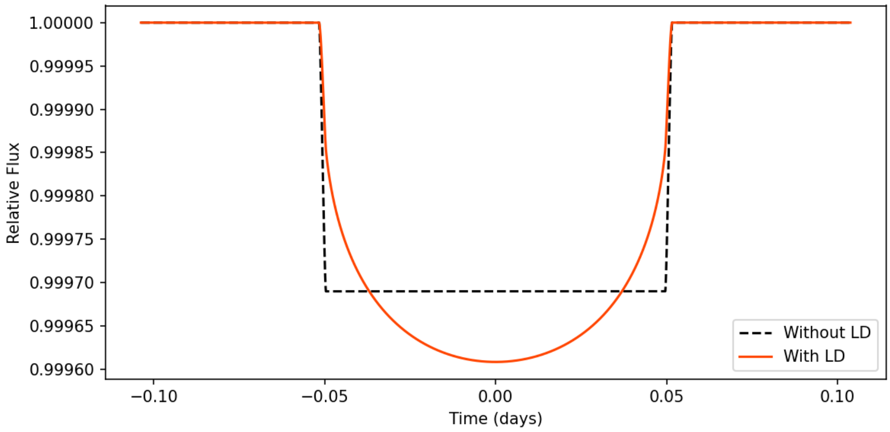

FIGURE 2.4: The effect of the limb darkening in the transit model using the transit parameters from HD 15337 b (see Chapter 3). The observed depth is not constant throughout the transit duration, with the maximum depth happening in the middle, when the light coming from the centre of the stellar disc is being blocked.

used in similar works (e.g. Maciejewski et al., 2020; Hoyer et al., 2022). The power-2 law is a suitable alternative (e.g. Barros et al., 2022b) that has been shown to have a better match to the stellar intensities retrieved from stellar atmospheric models (Morello et al., 2017; Short et al., 2019) at the expense of a slightly more difficult fit.

The quadratic law is given by equation 2.1:

$$I(\mu)/I_c = 1 - u_1(1-\mu) - u_2(1-\mu)^2 \tag{2.1}$$

where I_c is the intensity at the centre of the disc, u_1 and u_2 are the limb-darkening coefficients and $\mu = \cos\theta$ as per Figure 2.3 (with $\mu = 1$ at the centre of the disc). The coefficients u_1 and u_2 can be fixed and obtained through tabulated values (e.g. Claret, 2017), but these values do not always reproduce the true stellar intensity profiles and may introduce some bias in the results while also underestimating the uncertainties (e.g. Csizmadia et al., 2013; Espinoza & Jordán, 2015). Therefore, in this work we compute the limb darkening profiles through the Limb Darkening Toolkit (LDTk, Parviainen & Aigrain, 2015), which creates a custom profile through the effective temperature $T_{\rm eff}$, gravity g and metallicity [Fe/H] of the star, based on the spectrum library from Husser et al. (2013) and the response function of the instrument.

2.2 Analysis of radial velocities time-series

The techniques to extract radial velocities from stellar spectra have been improving significantly in the last few years, accompanying the improvement in the instrumental side that allows more and more precise data. In this section, we briefly discuss the most commonly used techniques for reducing the data and obtain RV values from the reduced spectra along with additional information that helps disentangling instrumental and astrophysical effects, enabling the planetary signals to be identified.

2.2.1 The cross-correlation function (CCF)

One of the most widely used methods to extract RVs is the cross-correlation function (CCF) method (Baranne et al., 1996). The observed spectrum is cross-correlated with a template spectrum (or mask), which highlights the positions of the absorption lines. The relative radial velocity is obtained by fitting an inverted Gaussian shape to the CCF and taking the minimum point of the fitted function. Deeper and sharper spectral lines lead to more precise RV measurements. As such, it is common that a weighted mask is used to give more weight to these deeper and sharper lines and improve the result (e.g. Pepe et al., 2002).

The CCF is also a key source of information for other properties that can be used to separate planetary and stellar signals, for example the full width at half maximum (FWHM), which describes the width of a Gaussian function between the two points where the curve is at half its maximum, and the bisector span (BIS) which is a measure of the asymmetry of the CCF (Queloz et al., 2001, see Figure 2.5).

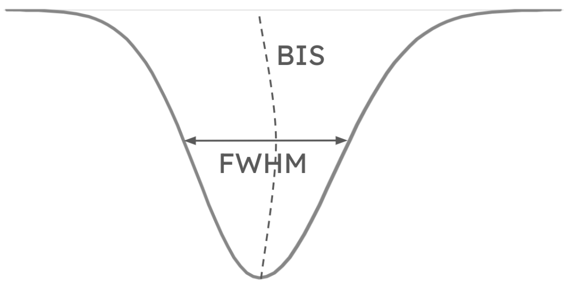

FIGURE 2.5: Simplified schematic of the Gaussian shape of a cross-correlation function (CCF) and the respective full width at half maximum (FWHM) and bisector span (BIS).

2.2.2 Impact of stellar variability

The RV method measures relative radial velocities by detecting Doppler shifts in a star's spectral lines. Various astrophysical and instrumental effects, such as gravitational redshift, convective blueshift, line asymmetries, and instrumental drifts, can introduce RV offsets or shifts (e.g. Dumusque et al., 2012; Fischer et al., 2016). While some of these effects evolve over long timescales and are less disruptive to short-period planet searches, stellar activity can introduce noise on timescales closer to the signals produced by small planets.

Therefore, the biggest challenge to the measurement of accurate and precise relative RVs is stellar activity. The rotation period of a star can be of the same order of magnitude as short-period planets, introducing periodic signals that can produce false positives (e.g. Huélamo et al., 2008; Forveille et al., 2009; Santos et al., 2014; Simpson et al., 2022) or dilute the real planetary signal (e.g. Santos et al., 2000; Faria et al., 2020; Barragán et al., 2023), leading to under- or overestimation of the planetary RV signal amplitude.

Active regions such as spots and faculae are tied to the stellar surface and rotate with the star, causing periodic variations in brightness and radial velocity signals that match the stellar rotation period or its harmonics. These signals, influenced by the stellar magnetic cycle, can reach amplitudes of several m/s, comparable to or even exceeding the RV signals of small exoplanets (e.g. Santos, 2008; Meunier et al., 2010; Da Silva et al., 2012; Aigrain et al., 2012), making planet detection and characterisation particularly challenging.

2.2.3 Activity indicators

Removing the effect of stellar induced signals from the RV series is a difficult process and is one of the major challenges in current exoplanet science regarding the RV method. The more the precision aimed at, the more relevant stellar activity becomes. While they have some similarities, planetary and stellar signals have some key differences that can be used to disentangle them. Some spectral lines and some characteristics of the CCF are more sensitive to stellar activity effects and not to planetary signals, and are therefore referred to as activity indicators.

Commonly, planetary bodies do not modify the shape or the width of the CCF and only produce a shift. In contrast, stellar activity can distort the CCF, affecting its symmetry and the full width at half maximum (FWHM). As the star rotates, the active regions move in and out of view, altering the spectral line profiles and introducing skewness to the CCF, which distorts its symmetry (e.g. Queloz et al., 2001; Anglada-Escudé et al., 2016;

Haywood, 2016; Simola et al., 2019; Lafarga et al., 2020; Costes et al., 2021). Therefore, while a periodic signal caused by an external body is primarily seen in the RV series, it is less likely to appear in the FWHM or BIS series, which are more sensitive to stellar activity (e.g. de Beurs et al., 2022).

Other activity indicators can be obtained from the stellar spectrum itself. One of the most widely used indicators used to quantify variations in stellar activity is the S-index (Wilson, 1978), which in general terms is the ratio between the core emission in the Ca II H & K lines and the continuum. These lines are related to chromospheric heating and are therefore sensitive to stellar activity events, particularly faculae (Noyes et al., 1984), being adequate especially for stars of the F, G and K types (Cincunegui et al., 2007). The S-index can be converted to the chromospheric emission ratio, denoted by R'_{HK} (Noyes et al., 1984), and is widely used in a logarithmic scale ($\log R'_{\mathrm{HK}}$) to search for activity signals in RV data.

2.2.4 Detrending RVs with Gaussian processes

With the significant impact that stellar variability has in small planet detection and characterisation (e.g. Santos et al., 2014; Costes et al., 2021; Simpson et al., 2022), one of the main targets of the scientific community is to develop algorithms that allow for the removal of such signals and the consequent improvement on the precision of measured planetary-nature RV signals.

One of the better approaches to model stellar activity is through the use of a Gaussian process regression (GP; e.g. Haywood et al., 2014; Rajpaul et al., 2015; Faria et al., 2016; Cloutier et al., 2019). GPs are particularly well suited to model deterministic processes with unknown functions, which is the case with most of the stellar activity phenomena affecting RV data.

The choice of the appropriate covariance function, or simply *kernel*, is key to model the physical processes that the GP is representing. Here we present the quasi-periodic covariance function from Rajpaul et al. (2015), which is an improvement on the simpler and more conventional squared-exponential covariance function as it includes a degree of periodicity as we expect to see in stellar activity. This *kernel* is adequate to model variability associated with rotational spot modulation, which is one of the main components of stellar activity in radial velocity data (Barros et al., 2020). Other *kernel* functions can be utilised, like the variation of the quasi-periodic *kernel* proposed by Perger et al.

(2021) which adds a cosine component to the *kernel* function, or the Matérn 3/2 *kernel* (Rasmussen & Williams, 2006), used in photometry decorrelation in previous works (Leleu et al., 2021; Barros et al., 2022b; Bonfanti et al., 2024).

The quasi-periodic *kernel* can be represented by the following expression seen in Demangeon et al. (2021) and referenced therein, which is a more physical-oriented adaptation from the purely mathematical expression shown in Rajpaul et al. (2015).

$$K(t_i, t_j) = A^2 \exp\left[-\frac{(t_i - t_j)^2}{2\tau_{\text{decay}}^2} - \frac{\sin^2(\frac{\pi}{P_{\text{rot}}}|t_i - t_j|)}{2\gamma^2}\right] \tag{2.2}$$

The GP hyperparameters can be used as indicators of the physical phenomena that are being modelled. A is the amplitude of the GP, while P_{rot} is the period of recurrence of the covariance, which for this case can be taken as the periodicity of the activity signal the GP is modelling. In most cases this is simply the stellar rotation period, but other periodic signals from magnetic cycles can be modelled the same way. τ_{decay} is the aperiodic coherence, which in physical terms is related to the decay timescale of the active regions (Haywood et al., 2014). In the same way, γ is the periodic coherence, that can be seen as a measure of the number of active regions within a single period. These coherence values show the correlation between values over several periods (aperiodic) and within a single period (periodic).

2.3 Data analysis overview

Data analysis is performed by fitting a mathematical model to the observations to determine the most likely set of model parameters. This is achieved through Bayesian analysis and the use of random sampling methods to explore the parameter space and evaluate multiple parameter combinations. In this section, we go through the Bayesian analysis framework and the random sampling methods that we use in our analyses.

2.3.1 Bayesian inference framework

The Bayesian inference approach consists of applying Bayes' theorem to perform statistical inference, using prior information and observed data to draw conclusions about the probability of a given hypothesis or output. The Bayes' theorem is given in equation 2.3 and calculates the posterior probability $P(\theta|D, M)$ of the model M given the observed data D

and a set of parameters θ, based on the likelihood $P(D|\theta, M)$ and the prior information $P(\theta|M)$. The evidence $P(D|M)$ is used to normalise the posterior probability.

$$P(\theta|D, M) = \frac{P(D|\theta, M) \cdot P(\theta|M)}{P(D|M)} \tag{2.3}$$

2.3.1.1 Prior distributions

The prior, given by $P(\theta|M)$ in equation 2.3, is the probability of the given parameters in the model M before considering the observed data. It represents prior knowledge about the parameters and the model, such as physical constraints or specific parameter ranges.

The most commonly used prior distributions in Bayesian inference are the uniform and the Gaussian distributions, although other priors can be used, like the Jeffreys prior, the beta distribution or the log-normal distribution. The uniform distribution is a generally uninformative prior, only limited by its range, that represents a weak previous knowledge about the parameter in question and is used often as a conservative way to avoid introducing bias in the results. It can be written as $\mathcal{U}(a, b)$, where a and b are the lower and upper limits of the interval, and its probability is given by $(b-a)^{-1}$ inside the interval and 0 outside of it.

The Gaussian (or normal) distribution is the most typical case of an informative prior, where the mean and standard deviation of a parameter are known from a previous analysis. This kind of prior allows the propagation of the uncertainty of the previous analysis and together with the new data it leads to an updated posterior distribution. It is defined as $\mathcal{N}(\mu, \sigma)$, where μ is the mean and σ is the standard deviation. The probability of a Gaussian distribution of a parameter θ_i is given by equation 2.4.

$$\mathcal{N}(\mu, \sigma) = \frac{1}{\sigma\sqrt{2\pi}} \exp\left(-\frac{(\mu-\theta_i)^2}{2\sigma^2}\right) \tag{2.4}$$

In this work (Chapter 3), the beta distribution is used as a prior for eccentricity, following the findings of Kipping (2013). It is part of the exponential distribution type and its probability can be defined as

$$P_\beta(e; a, b) = \frac{1}{B(a, b)} e^{a-1}(1-e)^{b-1} \tag{2.5}$$

,

where a and b are the two parameters that define the distribution and B is the beta function, which is used to ensure the total probability equals 1. The main advantage of this parametrisation is that it can reproduce a vast range of different distributions with only two parameters, making it especially versatile and adaptable to the specific case of the eccentricity distribution (Kipping, 2013). It is limited to the interval [0,1].

2.3.1.2 Likelihood

The likelihood $P(D|\theta, M)$ represents the compatibility of the acquired data D with the model M and a given parameter set. In other words, it is the probability of observing the data under the given model parameters. Assuming that each data point is independent from the others, the joint likelihood of the data is given by the product of the individual likelihood of each data point (equation 2.6 below), and it is a function of the model parameters.

$$P(D|\theta, M) = \prod_i^N P(D_i|\theta, M) \tag{2.6}$$

Since we assume the model M is true, the individual data points only differ from the predicted model if there is an associated measurement error. Therefore, assuming the data is normally distributed, the individual likelihood is given by a Gaussian distribution with a standard deviation σ corresponding to the data uncertainty. Using equation 2.4 we can rewrite equation 2.6 as

$$P(D|\theta, M) = \prod_i^N \frac{1}{\sigma_i\sqrt{2\pi^2}} \exp\left(-\frac{[\bar{F}_i - F_i(\theta)]^2}{2\sigma_i^2}\right) \tag{2.7}$$

where $\bar{F}_i$ is the observed value, σ_i is the corresponding uncertainty, and $F_i(\theta)$ is the theoretical value given by the model with a set of parameters θ.

2.3.1.3 Marginal likelihood

The marginal likelihood, or evidence, given by the denominator $P(D|M)$, is the probability of observing the data D given the model M and is used as a normalisation factor in the Bayes' theorem. The marginal likelihood is primarily used for model comparison, as it evaluates how well the model explains the data without being restricted to specific parameter values. It does not influence the estimation of parameters within a single model. Instead, it integrates out the parameters, thereby reflecting the overall support for the model itself. The marginal likelihood is defined as the integral of the likelihood multiplied by the prior over the entire parameter space:

$$P(D|M) = \int P(D|\theta, M)\, P(\theta|M)\, d\theta \tag{2.8}$$

This calculation evaluates how well the model explains the data while taking into account the prior distribution of its parameters.

2.3.1.4 Posterior distribution

The posterior distribution $P(\theta|D, M)$ is the updated joint probability of a set of parameters θ, given the model M and the data D, and is the result of equation 2.3. To obtain the marginal posterior of each parameter individually, the joint posterior is integrated over all other parameters in a process known as marginalization (equation 2.9):

$$P(\theta_i|D, M) = \int P(\theta|D, M)\, P(\theta|M)\, d\theta \tag{2.9}$$

This integral sums over all possible values of the remaining parameters to compute the marginal posterior of θ_i. Therefore, with a high number of free parameters it becomes necessary to use methods like random sampling to obtain the posterior. In the next section, we will go through the Markov chain Monte Carlo algorithm, one of the most common choices to perform random sampling in probability analysis.

2.3.2 Markov chain Monte Carlo algorithm

Markov chain Monte Carlo (MCMC) is a class of algorithms that use Markov chains to generate random samples from a target distribution, with the goal of estimating the posterior distributions of a set of parameters (Sharma, 2017). Markov chains describe a series of events where the probability of each event depends on the outcome of the previous event, and are broadly used in statistical and probability analysis. The MCMC sampler starts a chain by drawing a random sample X from the initial distribution of all parameters and evaluates the posterior probability of the retrieved sample. At each step, a new candidate sample is proposed based on an initial distribution, and the acceptance of this new sample is determined by an acceptance probability based on the ratio of posterior probabilities. If accepted, the new sample is added to the chain, otherwise, the sampler retains the current point. Through this iterative process, the chain of samples converges to approximate the target distribution (e.g. Gregory, 2005). The MCMC algorithm requires a high number of samples to ensure the final distribution is not influenced by the starting set of parameters. The initial steps, called the burn-in period, are typically discarded for the same reason.

In this thesis, the MCMC sampling is implemented using the `emcee` package (Foreman-Mackey et al., 2013), which employs the affine-invariant ensemble sampler introduced by Goodman & Weare (2010). While the Metropolis-Hastings algorithm (Robert et al., 2004) is a generally used MCMC approach, the affine-invariant method used in `emcee` is particularly efficient for high-dimensional parameter spaces and scenarios where parameters show strong correlations (e.g. Foreman-Mackey et al., 2013).

2.3.3 Bayesian Information Criterion

In Bayesian analysis there is often the need to match different models to the available data and select the one that represents the data the best. The most common approach to compare models comes from their posterior probability distributions. Through the Bayes theorem, it can be rewritten as the product of the ratio of the probability of each model $P(M)$ by the ratio of their marginal likelihoods $P(D|M_i)$, which is often referred to as the Bayes factor (Kass & Raftery, 1995). The Bayes factor (equation 2.10) is difficult to calculate when there are many unknowns or large amounts of data, and many different variations have been created (see Alston et al., 2005, and references therein).

$$\frac{P(D|M_1)}{P(D|M_2)} = \frac{P(M_1)}{P(M_2)}\frac{P(M_1|D)}{P(M_2|D)} \tag{2.10}$$

The Bayesian Information Criterion (BIC; Schwarz, 1978) is a model selection criterion developed as an alternative over the Bayes factor, being an approximation of the latter. The BIC can be calculated through

$$BIC = k \ln n - 2 \ln \hat{L} \tag{2.11}$$

where $\hat{L} = P(D|\hat{\theta}, M)$ is the maximum of the joint likelihood function of a model M, n is the number of data points or the sample size, and k is the number of free parameters of the model. The BIC is sensitive to the amount of data and to the number of free parameters, and it is designed to favour the simpler model and penalise models with higher numbers of free parameters. The BIC is calculated individually for each model, and the model with the lowest absolute BIC is the most favoured, however, it is not the absolute value in itself that provides any conclusion. In reality, it is the difference between both BIC values (ΔBIC) that allows us to interpret how strong the evidence is. Most authors define $\Delta BIC \gtrapprox 5-6$ as the threshold for which the evidence is considered significant (e.g. Kass & Raftery, 1995; Efron et al., 2001; Liddle, 2007).

The BIC is widely used in model comparison for transit and RV analyses especially when finding and characterising new exoplanets, for example, when modelling activity signals (e.g. Morris et al., 2021; Bonfanti et al., 2024) or searching for orbital decay (e.g. Turner et al., 2021b; Barros et al., 2022b; Harre et al., 2023).

Chapter 3

Characterisation of small planets: the HD 15337 system

This chapter was published in: Rosário, N. M., et al., *Precise characterisation of HD 15337 with CHEOPS: A laboratory for planet formation and evolution*, Astronomy & Astrophysics 686 (2024): A282.

3.1 Introduction

This chapter focuses on the characterisation of small planets and the techniques used to study their structure and composition. The rapid increase in dedicated space missions such as CoRoT, Kepler, TESS and CHEOPS has led to the discovery of several multi-planet systems with two or more planets in the super-Earth ($R_{\mathrm{p}} = 1 - 2\ R_{\oplus}$) and sub-Neptune ($R_{\mathrm{p}} = 2 - 4\ R_{\oplus}$) region of the mass-radius diagram. These multi-planet systems (e.g., GJ 9827, Prieto-Arranz et al., 2018) are particularly important to understand the formation and evolution of exoplanetary systems, as well as our own Solar System, by examining the differences in structure and composition between each planet. Since these planets orbit the same star, they must have formed under the same initial conditions, therefore, discrepancies in atmosphere structure and bulk density could be attributed to different formation location and evolutionary processes.

HD 15337 (TIC 120896927, TOI-402) is a bright K1 dwarf star that hosts two small planets spanning both sides of the radius valley (see Section 1.2). The planets were initially discovered by TESS and confirmed with HARPS radial velocity measurements in two independent analyses (Gandolfi et al., 2019; Dumusque et al., 2019). The inner planet, HD 15337 b, is a short-period ($P = 4.76$ d) super-Earth, while HD 15337 c orbits the star with a 17.2-day period. The discovery papers found two planets with similar masses, with Gandolfi et al. (2019) reporting masses of $M_\mathrm{b} = 7.51^{+1.09}_{-1.01}\ M_\oplus$ and $M_\mathrm{c} = 8.11^{+1.82}_{-1.69}\ M_\oplus$ and Dumusque et al. (2019) finding values of $M_\mathrm{b} = 7.20 \pm 0.81\ M_\oplus$ and $M_\mathrm{c} = 8.79 \pm 1.68\ M_\oplus$ for planets b and c, respectively. In contrast, HD 15337 b was found to have a significantly smaller radius ($R_\mathrm{b} = 1.64 \pm 0.06\ R_\oplus$ in Gandolfi et al., 2019 and $R_\mathrm{b} = 1.699^{+0.062}_{-0.059}\ R_\oplus$ in Dumusque et al., 2019) than HD 15337 c ($R_\mathrm{c} = 2.39 \pm 0.12\ R_\oplus$ in Gandolfi et al., 2019 and $R_\mathrm{c} = 2.522^{+0.106}_{-0.102}\ R_\oplus$ in Dumusque et al., 2019).

The two planets have nearly identical masses but different sizes, indicating differences in structure and composition. While they were most likely formed in the same region of the protoplanetary disc, the smaller radius of the inner planet suggests that it lost its original gas envelope, which is still present in the outer planet. A temporal analysis of XUV-driven atmospheric escape by Dumusque et al. (2019) confirms that HD 15337 b could not have kept its gas envelope, whereas its outer companion should have been able to maintain its atmosphere. This makes the system an important laboratory for studying atmospheric evolution, as photoevaporation of the primordial atmosphere is one of the most widely accepted explanations for the radius valley.

3.2 Observations

3.2.1 TESS

HD 15337 was observed by Camera #2 of TESS (see Section 1.3.2) with a two-minute cadence in Sectors 3 and 4 (between September 20 and November 15, 2018) during Cycle 1 of the TESS mission. More recently, it was observed again during the first extended mission in Sector 30, from September 22 to October 21, 2020. The data from the first two sectors were published and analysed in Gandolfi et al. (2019) and Dumusque et al. (2019).

The corrected and normalised PDCSAP light curves (see Section 2.1.2) for HD 15337 are plotted in Figure 3.1 with the overplotted fit model showing the location of the transits.

3.2.2 CHEOPS

The observations of TESS and the discovery of the two planets across the radius valley made HD 15337 a promising target for follow-up observations. The higher precision of CHEOPS photometric data compared to TESS allows for a reduction in radius uncertainty, which is

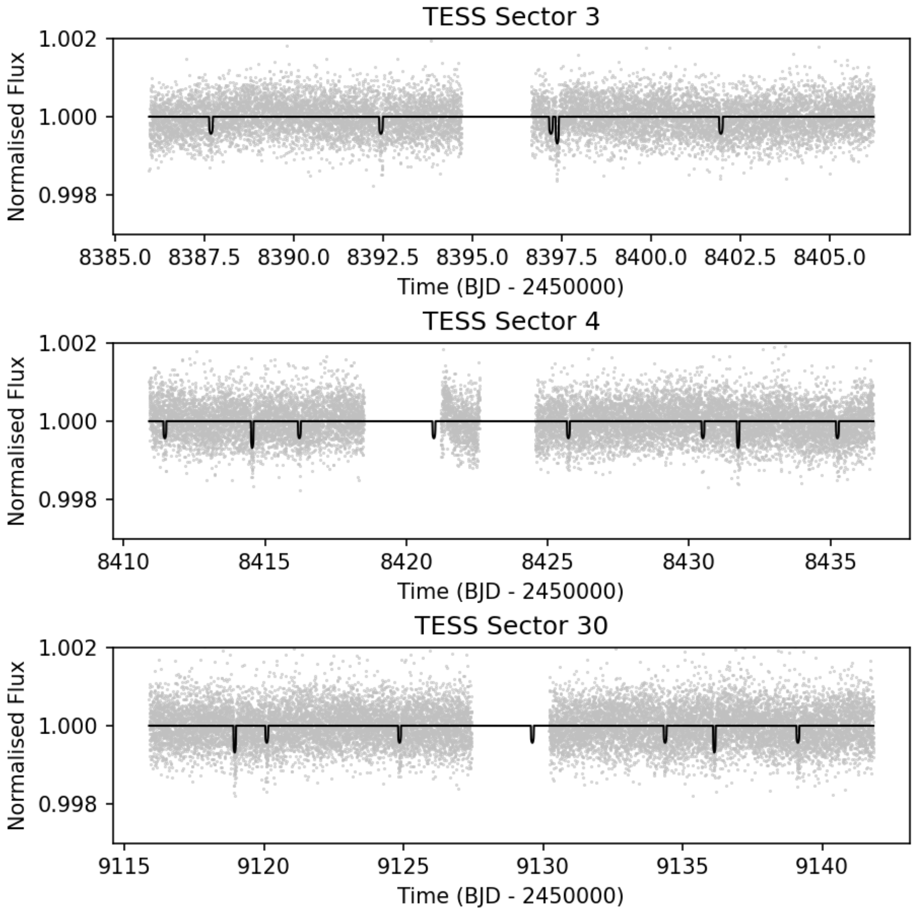

Figure 3.1: Plot of the normalised PDCSAP flux obtained from TESS observations of HD 15337.

especially relevant to better constrain the mass and size of the planets' gas envelopes (Otegi et al., 2020). As a result, we obtained six visits of HD 15337 as part of the Guaranteed Time Observation (GTO) programme, spanning a total time of around 2.2 days. From the six visits, three observed transits of HD 15337 b, two of HD 15337 c, and one visit captured an overlapping transit of both planets. The light curves from all six visits are shown in Figure 3.2, with the fit model overplotted for each. Observation details are listed in Table 3.1.

According to the data reduction report, the default aperture is best suited for our case, so we chose the corresponding light curves to use in this analysis (see Section 2.1.2 for details on the data reduction and pre-processing). We used the same aperture for all visits to maintain consistency and avoid potential discrepancies caused by different apertures (which could happen when using the optimal apertures).

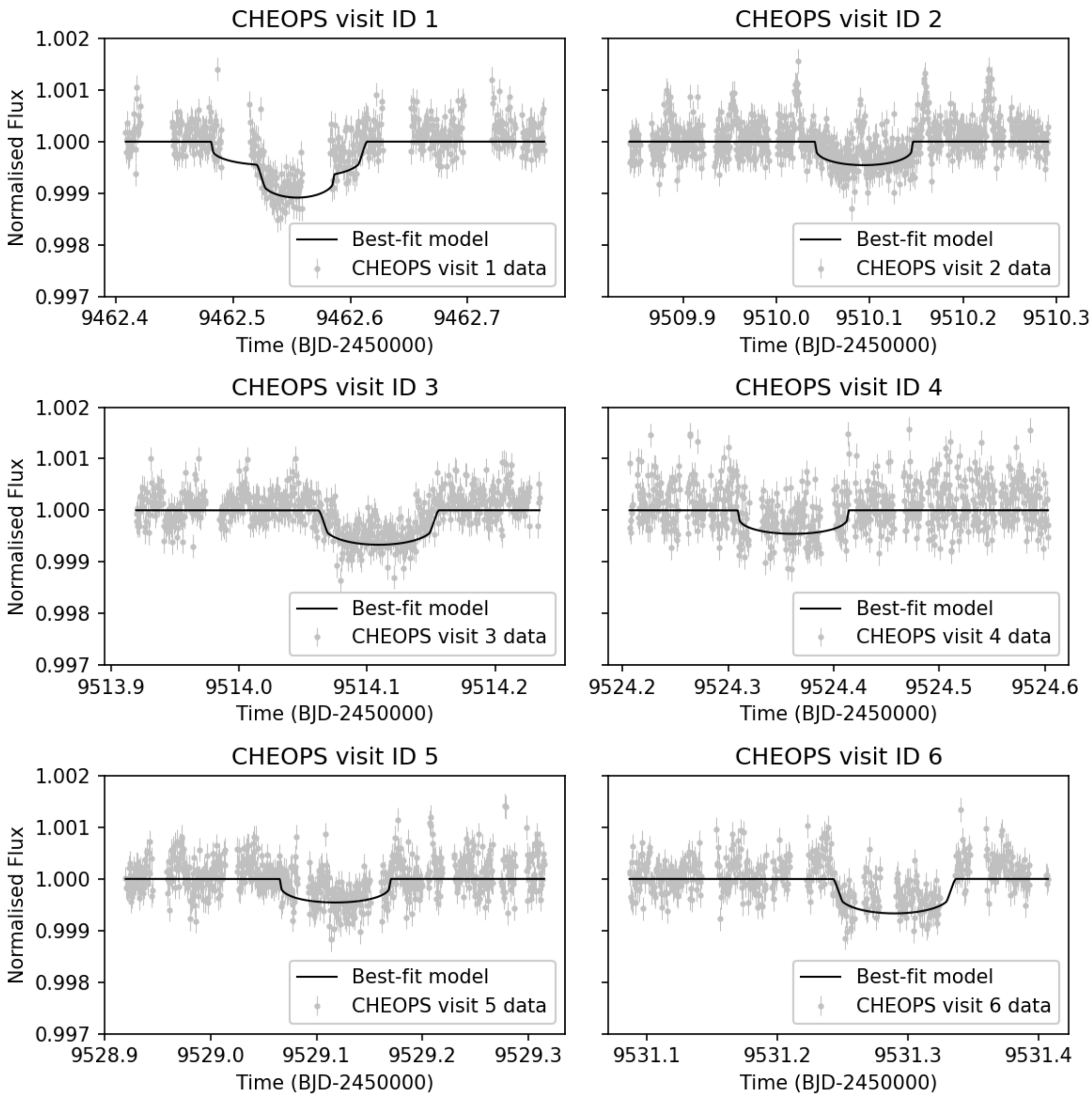

FIGURE 3.2: Plot of the normalised flux obtained from the six CHEOPS visits of HD 15337.

TABLE 3.1: CHEOPS observation log for HD 15337. The first column shows the number of the observation as referred to in this thesis, the second column shows the planet transits observed in each visit, and the remaining columns show the file key of each CHEOPS visit, the start date of the observations, the duration, the exposure time of each observation, the efficiency and the number of non-flagged data points on each visit. Originally published in Rosário et al. (2024).

ID	Planets	File Key	Start Date [UTC]	Duration [h]	Exp. Time [s]	Efficiency	No. Points
1	b, c	CH_PR100031_TG044201_V0200	2021-09-04T21:41:56	8.57	38.6	66.2%	530
2	b	CH_PR100031_TG045301_V0200	2021-10-22T08:05:36	10.76	38.6	91.5%	919
3	c	CH_PR100031_TG045401_V0200	2021-10-26T09:56:35	7.58	38.6	94.8%	671
4	b	CH_PR100031_TG045302_V0200	2021-11-05T16:50:36	9.51	38.6	83.4%	740
5	b	CH_PR100031_TG045303_V0200	2021-11-10T09:56:37	9.51	38.6	81.5%	723
6	c	CH_PR100031_TG045402_V0200	2021-11-12T13:57:57	7.69	38.6	75.6%	543

3.2.3 HARPS

The first HARPS spectroscopic observations of HD 15337 were originally reported in Gandolfi et al. (2019) and Dumusque et al. (2019). We used the 87 publicly available measurements from the ESO archive (between 15 December 2003 and 6 September 2017) and obtained additional 32 new spectra using HARPS (between 9 July and 12 September 2019), as part of a collaboration with the KESPRINT follow-up program for TESS transiting targets.

We used the dedicated data reduction software (DRS; Lovis & Pepe, 2007) to reduce the spectra and obtain the required values. We performed a cross-correlation of the spectra using a K5 numerical mask (Baranne et al., 1996; Pepe et al., 2002) to extract the RV measurements and the FWHM and BIS and we further used the same software to extract the $\log R'_{\rm HK}$ indicator from the spectra (refer to Section 2.2.3 for a description of each indicator and their role in stellar activity corrections).

Due to the fibre change in HARPS, the RVs obtained after June 2015 show an offset caused by this change. To account for the offset, the RVs are divided in two different independent sets, before and after the fibre change.

The HARPS RVs are further corrected for secular acceleration using the formulation from Kuerster et al. (2003). We calculated an average secular acceleration of 0.05189 $\mathrm{ms^{-1}yr^{-1}}$ during the HARPS observation period, using available data from Gaia DR2 (Soubiran et al., 2018) and EDR3 (Gaia Collaboration, 2020). After applying the correction, we found a maximum variation in the radial velocity of approximately +0.82 $\mathrm{ms^{-1}}$ for the last data point in the time series, relative to the first measurement.

3.2.4 PFS

HD 15337 was also observed with the Planet Finder Spectrograph (PFS; Crane et al., 2006, 2008, 2010) as part of the Magellan-TESS Survey (MTS; Teske et al., 2021). The observations were scheduled between 12 February 2019 and 20 December 2019 and a total of 48 new spectra were retrieved. The data reduction in order to obtain the RVs was performed by a custom pipeline based on Butler et al. (1996), which is described in more detail in Teske et al. (2021). The PFS RVs were included as a separate dataset in our analysis.

3.3 Stellar characterisation

The work presented in this section was performed by the stellar characterisation group of the CHEOPS consortium. As such, only the high level process and the main results necessary to understand the rest of the analysis are presented here and more details can be found in Rosário et al. (2024).

3.3.1 Stellar parameters

The estimation of the stellar spectroscopic parameters is based on a combined HARPS spectra using the ARES+MOOG equivalent width (EW) method, described in more detail in Sousa (2014). This analysis uses the EWs of selected iron lines from the spectrum and applies a minimisation algorithm on the ionisation and excitation equilibrium, which leads to the optimal set of parameters. The derived stellar parameters and abundances are shown in Table 3.2.

TABLE 3.2: Overview of fundamental stellar parameters for HD 15337. Adapted from Rosário et al. (2024).

Parameter [unit]	Value	Source
Name	HD 15337	Reference
Gaia DR3 ID	5068777809824976256	Gaia Collaboration et al. (2023)
G (*Gaia*) (mag)	8.865 ± 0.00276	Gaia Collaboration et al. (2023)
$T_{\rm eff}$ (K)	5131 ± 74	Rosário et al. (2024)
$\log g$ (cgs) [spec]	4.37 ± 0.08	Rosário et al. (2024)
$\log g$ (cgs) [Gaia]	4.48 ± 0.04	Rosário et al. (2024)
[Fe/H] (dex)	0.03 ± 0.04	Rosário et al. (2024)
[Mg/H] (dex)	0.09 ± 0.06	Rosário et al. (2024)
[Si/H] (dex)	0.07 ± 0.05	Rosário et al. (2024)
$v$mic (km s^{-1})	0.87 ± 0.13	Rosário et al. (2024)
$R_{\rm s}$ ($R_\odot$)	0.855 ± 0.008	Rosário et al. (2024)
$M_{\rm s}$ ($M_\odot$)	0.840 ± 0.041	Rosário et al. (2024)
$t_{\rm s}$ (Gyr)	$9.6^{+3.8}_{-3.9}$	Rosário et al. (2024)

3.3.2 Stellar companion

HD 15337 has a dim stellar companion with a magnitude ratio of $\Delta m \approx 9.33$ mag at 832 nm, detected by speckle imaging with an angular separation of 1.4 arcseconds (Ziegler et al., 2020; Lester et al., 2021). The presence of this companion slightly affects the measured transit depth due to contaminating flux, leading to a small underestimation of the observed radius.

The effect on the radius can be estimated by calculating the dilution factor (X_R), defined by Ciardi et al. (2015) as the ratio between the true radius and the observed radius. Assuming that both planets orbit the primary, this factor can be calculated using Equation 3.1 (Ciardi et al., 2015), where F_{total} is the total flux and F_1 is the flux of the primary,

$$X_R = \sqrt{\frac{F_{\text{total}}}{F_1}} \tag{3.1}$$

This assumption can be verified by estimating the maximum transit depth observed in the extreme case where the planets orbit the secondary star and completely block its light. With a $\delta_{\text{max}} \approx 185$ ppm, we find that this depth is approximately half the transit depth of the smallest planet (HD 15337 b). This indicates that the observed depth is only possible if both planets orbit the primary star. we calculate a dilution factor of 1.00009 for HD 15337. This value is negligible compared to the precision in transit depth measurements achievable by CHEOPS. We therefore do not expect this companion to impact the conclusions or the results from our transit and internal structure analysis.

3.4 Data analysis

In this work, we perform a combined fit of both RV and photometry data. The photometric detrending of the TESS light curves is performed beforehand using the methodology described in Section 2.1.2, while the detrending of the CHEOPS light curves, along with corrections for stellar activity and instrumental systematics, is incorporated into the model, ensuring that their uncertainties are propagated to the final error bars. Although more computationally intensive, the joint fit provides a more accurate and precise determination of shared parameters (such as eccentricity and period), resulting in a more precise estimate of each planet's mass and radius.

In this section, we define the models that are used in the joint analysis, which will be discussed in subsequent sections. We present the methods for detrending the CHEOPS light curves, the transit model, and the radial velocity model, including the Gaussian process used to correct the RVs.

3.4.1 CHEOPS detrending model

The location of the CHEOPS satellite, in a nadir-locked low-Earth orbit, causes the field stars to rotate around the target star in the CHEOPS image with the variation of the spacecraft's orbital position. This implies that the measured flux may vary with the roll angle of the spacecraft, requiring a prior assessment of the correlation between the flux and the roll angle. In particular, we observe that the background flux variations are more abrupt when approaching an Earth occultation, which occurs when the Earth crosses the telescope's field of view. The gaps visible in the CHEOPS light curves (Figure 3.2) are often caused by this effect, although they can also be caused by South Atlantic Anomaly (SAA) crossings (e.g. Hoyer et al., 2020; Lendl et al., 2020; Maxted et al., 2022; Barros et al., 2022b).

The position of CHEOPS, in its orbit and relative to the Sun, is also important, as both Earth occultations and manoeuvres needed to move between two targets can cause temperature fluctuations in the telescope. This effect, explained in more depth in Morris et al. (2021), is observed as a ramp effect at the beginning of observations, as the telescope adjusts to the new temperature. This temperature variation must be taken into account in the detrending of the data.

Choosing the detrending parameters

The `pycheops` pipeline (Maxted et al., 2022) provides a diagnostic plot (Figure 3.3) showing the light curves as well as correlations between the background flux, the centroid position and the roll angle. This allows for a preliminary validation of which time series are relevant for decorrelation. We also use the built-in function `shouldIdecorr`, which performs an initial model comparison using the Bayesian Information Criterion (BIC) (see Section 2.3.3), to validate the chosen decorrelation parameters. We found the most important parameters to decorrelate against are the background flux, the roll angle, the centroid position and the temperature of the telescope tube (given by the ThermFront2 Sensor temperature value included in the data files), therefore, we include the corresponding time series in our decorrelation model.

Several methods can be used for decorrelation, one of which is the use of Gaussian processes (e.g. Barros et al., 2020, 2022b). However, due to the amount of data to analyse from transits and RVs, the GP regression would require substantial computational resources and time, so we opt for a more simple spline decorrelation, which sequentially fits the

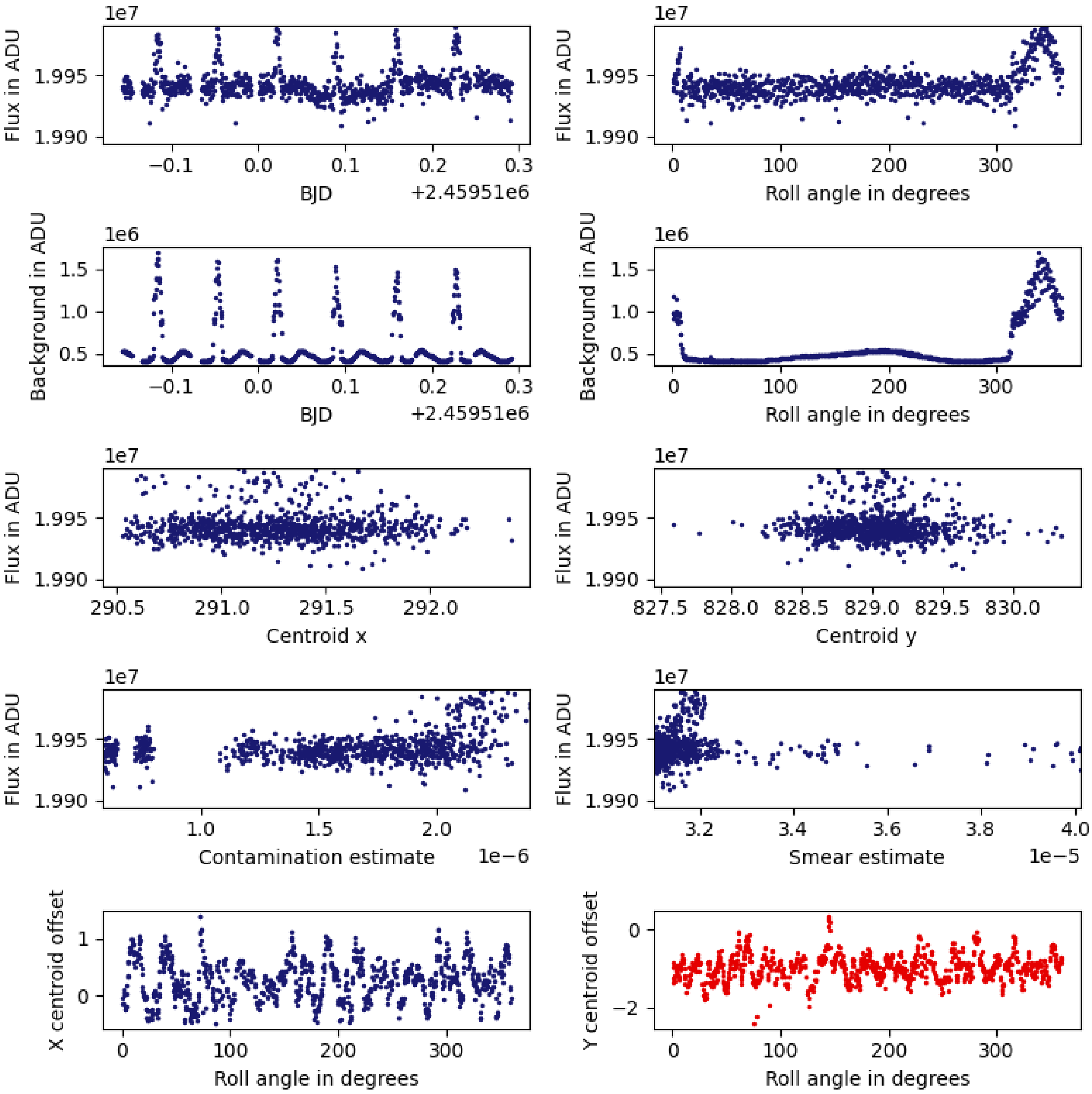

Figure 3.3: Example of the diagnostic plot provided by `pycheops` for the second visit of CHEOPS of HD 15337. From left to right, and top to bottom, the individual figures plot: the raw flux time series, the flux against the roll angle, the background flux time series, the background flux against the roll angle, the flux against the centroid position in x and y, the flux against the contamination, the flux against the smear estimate and the centroid position (x and y) against the roll angle.

residuals against each of the decorrelation time series chosen before, simultaneous with the joint transit and RV fit.

3.4.2 Radial velocity analysis

The top plot in Figure 3.4 displays the RV time series, corrected for the offset caused by the HARPS fibre change. For visualization purposes and to provide an initial overview of the RV measurements, the first HARPS subset (before the fibre change) is defined as the reference set and the remaining sets (including the PFS set, which is originally centred around zero) are shifted to the same reference. In this preliminary analysis, the offsets are determined as the difference between the median of each set and the median of the reference set. A long-term trend can be observed in the RV plot, possibly caused by long-term stellar activity or a long-period companion. The analysis of this trend will be discussed in more detail in Section 3.7, however, for the preliminary periodogram analysis, the trend is modelled using a second-order polynomial.

3.4.2.1 Periodogram analysis of the RV series

The remaining plots in Figure 3.4 show the RV generalised Lomb-Scargle (GLS; Zechmeister & Kürster, 2009) periodograms. The main peak in the periodogram of the raw RVs shows a strong signal around the period of HD 15337 b as per Gandolfi et al. (2019) and Dumusque et al. (2019), but there is no significant peak near the expected period of HD 15337 c, suggesting that its signal is likely overshadowed by the stronger signal of HD 15337 b and other signals caused by stellar activity or other stellar or planetary companions. To tackle this problem, we first subtract the long-term trend from the data (second periodogram of Figure 3.4) and then model the planetary signal of HD 15337 b with a Keplerian orbit model using the `radvel` Python package (third periodogram), also subtracting it from the RV data. With these two main signals removed and looking at the residuals, there is now a significant peak corresponding to the period of HD 15337 c along with other periodic signals at higher periods. We remove the signal from planet c in the same way as done for planet b, and the residuals then show a more clear peak around 36.5 days, which is close to the stellar rotation period found by Gandolfi et al. (2019).

The following step is to determine how to remove the stellar signals from the RVs. Using the periodograms in Figure 3.5, we can identify the signals in the FWHM, BIS and log R'_{HK} activity indicators (see Section 2.2.3) that can be attributed to the star. Looking at each individual row, it is evident that the $\log R'_{\rm HK}$ periodogram has strong peaks around the stellar rotation period seen in the RV periodogram but no peaks near the planet periods, while being sensitive to the stellar active regions, making it an excellent candidate for the decorrelation of the RVs and for modelling the stellar signal.

The RVs obtained with the PFS spectrograph can be found in Teske et al. (2021), however there was no information about the activity indicators for this specific set, therefore only the HARPS time series are used for the decorrelation.

3.4.2.2 Radial velocity model

We use a RV model consisting of three sub-models. First we have the planetary model, which is a Keplerian orbit model implemented through the `radvel` Python package (Fulton et al., 2018), parametrised by the systemic velocity v_0, the period P, the semi-amplitude of the RV signal K, and the products $e\sin\omega$ and $e\cos\omega$, which are alternative parametrisations of the eccentricity e and the argument of the periastron ω that improve the rate of convergence of low-eccentricity systems (Ford, 2005).

The second part of the model is the instrumental model, which models the instrumental noise and trends that appears in the data. We kept the initial data set as the reference, setting the reference v_0 and then define an offset between the other data sets and the reference (ΔRV), one for the post-fibre change HARPS measurements ($\Delta{\rm RV}_{{\rm HARPS}_1}$) and another for the PFS dataset ($\Delta{\rm RV}_{\rm PFS}$). The long-term trend in the RV series is modelled with a long-period sinusoidal function. A second-order polynomial can also be used to model this trend. During this analysis, both models were tested, but since no statistically significant differences were found, both were deemed suitable to model this trend. The sinusoidal model is parametrised by its period $P_{\rm sin}$, semi-amplitude $K_{\rm sin}$ and reference time $T_{0,\rm sin}$. Adding to this, there is also an instrumental detrending part in the model of the indicator time series, with a second-order polynomial being used to remove the long-term variations in the $\log R'_{\rm HK}$ series. A jitter parameter is included in both the RV and the $\log R'_{\rm HK}$ instrumental models to account for additional instrumental uncertainty.

For the stellar activity model, we use two independent GPs, each with its own quasi-periodic kernel as described in Section 2.2.4. As we want to use the $\log R'_{\rm HK}$ series to help constraining the stellar activity effect in the RVs, the two GPs share the same $P_{\rm rot}$, $\tau_{\rm decay}$ and γ, with the amplitude A being different. Then, one of the GPs is fit to the $\log R'_{\rm HK}$

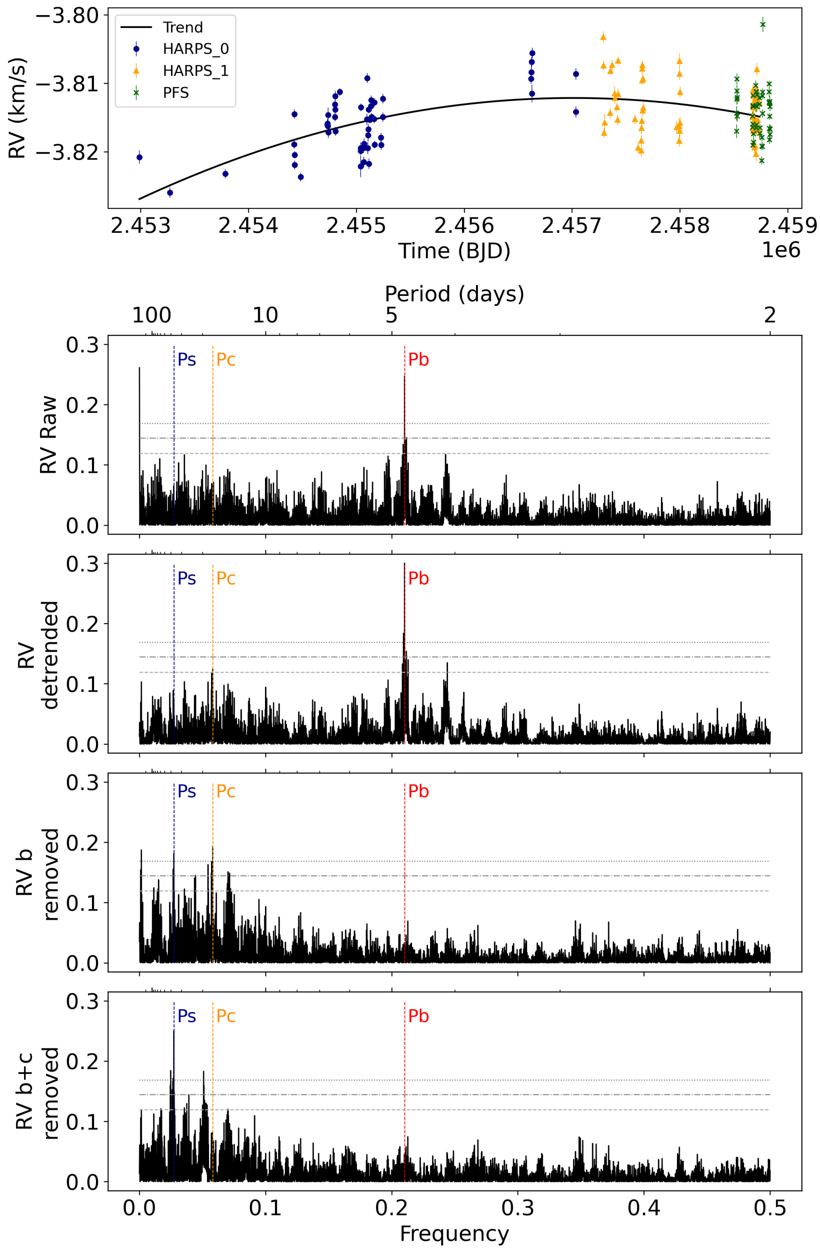

FIGURE 3.4: Plot of the full RV time series and corresponding GLS periodograms. In the top plot the blue dots show the reference HARPS set, the orange triangles show the HARPS RVs after the fibre change and the green crosses show the PFS RVs. The first periodogram is computed with the full RV set before any additional corrections other than the offsets. The second periodogram shows the periodogram after removing the long-term trend. The third and last periodograms are computed after removing the planetary signals from HD 15337 b and c, respectively. The dashed vertical lines show the approximate periods of planet b (red), planet c (orange) and stellar rotation (blue).

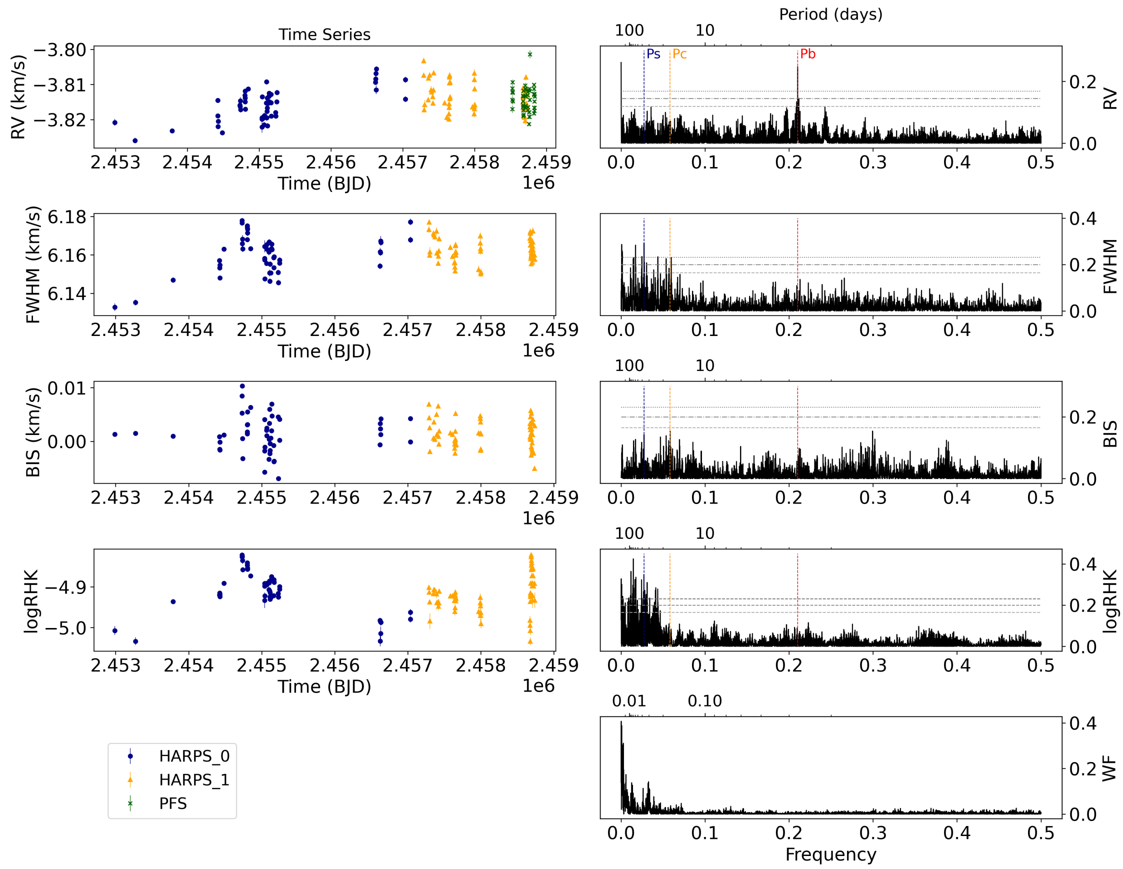

Figure 3.5: *Left:* plot of the offset-corrected time series of the RV observations of HARPS and PFS, as well as the activity indicators of the HARPS RVs. *Right:* corresponding GLS periodograms. The vertical dashed lines show the approximate periods of the known planets and stellar rotation as in Figure 3.4. The dashed horizontal lines show the 10% (dashed line), 1% (dot-dashed line), and 0.1% (dotted line) false-alarm probabilities as per Zechmeister & Kürster (2009). Figure and caption from Rosário et al. (2024).

series and the other is fit to the RV series. The GPs are implemented with the `george` package (Ambikasaran et al., 2015).

3.4.3 Transit model

The transit models are implemented with the `batman` package (Kreidberg, 2015). Each planet is modelled with a Keplerian orbit model parametrised by the period P, the mid-transit time T_0, the planet-star radius ratio $R_\mathrm{p}/R_\star$, the cosine of the orbital inclination $\cos i$, the stellar density $\rho_\star$ and the same eccentricity terms used in the RV model, $e\sin\omega$ and $e\cos\omega$.

The limb-darkening effect, described in Section 2.1.3, is also included using the quadratic law with coefficients u_1 and u_2. The limb darkening depends on the wavelength, so different coefficients have to be used for TESS and CHEOPS.

The decorrelation of the CHEOPS light curves described previously in Section 3.4.1 is performed simultaneously with the joint fit. We include an offset parameter for the median flux in each light curve, ensuring all light curves are normalised to the same reference. The TESS light curves are pre-processed and detrended separately (see Section 2.1.2), so the only parameter that is included is the median flux offset ΔF_{TESS} as done for the CHEOPS curves. While the TESS curves can also be detrended simultaneously, the large amount of data significantly increases computational demands. Removing out-of-transit points from the TESS curves substantially reduces the time and resources required for the analysis. For the same reason, we opt not to include an additional GP to detrend the TESS curves individually, as the computational cost outweighs the minor improvement in precision. The detrending steps done before should account for star spots and long-term activity signals and are deemed sufficient for the purpose of this analysis.

3.4.4 MCMC joint model fit of transit and RV data

The full analysis of the available data is performed using the code LISA (Demangeon et al., 2018, 2021; Barros et al., 2022a), which allows for a simultaneous fit of the RV model and the transit model, as well as any decorrelation and detrending models associated with the datasets.

All the models described earlier are run using an MCMC algorithm implemented with the `emcee` package (Foreman-Mackey et al., 2013), described in 2.3.2. We run a pre-minimisation routine based on the Nelder-Mead simplex algorithm (Nelder & Mead, 1965) to ensure adequate initial parameters and improve convergence efficiency. Additionally, the number of walkers is set to four times the number of free parameters in each run.

The prior distributions are selected to be uniform in the vast majority of the main parameters. We use the joint prior defined in Demangeon et al. (2021) for the transit parameters, which is a reparametrisation of T_0 and $\cos i$ into the impact parameter b and the orbital phase ϕ. The uniform priors on the period and orbital phase define the range within which the model searches for the transit, so we define uniform priors centred in the expected mid-transit time and within the limits of the CHEOPS observation window. The limits on b are imposed to allow a grazing transit if necessary, under the constrain that $b < 1 + R_{\mathrm{p}}/R_{\star}$, ensuring the planets are transiting. A polar prior, also defined in Demangeon et al. (2021), is used to reparametrise $e \sin \omega$ and $e \cos \omega$ into e and ω, facilitating the definition of physically motivated priors. We define a beta distribution based on the relationship from Kipping (2013) as the prior distribution for e (see Section 2.3.1.1), which takes into account the higher probability of low eccentricity planets and is shown to represent better the underlying distribution of eccentricities. We use the `LDTk` package to obtain the best values of the limb darkening coefficients for each instrument as described in Section 2.1.3. We set a Gaussian prior for the limb-darkening parameters in the transit model, with the mean and standard deviation obtained from the results of the LDTk calculation. In the RV model, the priors for v_0 and the offsets ΔRV are set as Gaussian with a conservative standard deviation of 0.01 $\mathrm{km\,s^{-1}}$.

As there is limited prior information about the hyperparameters of the GP that is used to model the stellar activity, we define all respective priors as uniform. The amplitude boundaries are set so that the difference between the highest and lowest points in the corresponding time series is inside the range. For P_{rot} the limits are set between 10 and 200 days, which allows the parameter space to be widely explored while keeping the rotation period within physically reasonable values. The same limits are applied to τ_{decay}. The γ parameter is estimated to be around 0.5 in Dubber et al. (2019), so we define a prior between one order of magnitude below and above that value. Wide uniform priors are also used for the parameters of the sinusoidal function used to model the long-term trend.

3.5 RV and transit results

We run the model for a total of 15000 steps, divided into two sub-runs, as this helps with memory constraints during the run due to the large amount of data being processed and the high number of chains in the MCMC. In the first part of the run we let the model run for 5000 burn-in steps to find the global maximum of the posterior function. The results from this initial run are then used to restart the chains and sample the posterior maximum over 10000 steps.

The main results of the run are shown in Table 3.3. The value of each parameter corresponds to the median of the posterior distribution from the MCMC run with the error bars given by the lower and upper values of the 68% confidence interval. The plot in Figure 3.8 shows the phase-folded fit of the transits. The higher precision and lower dispersion of the CHEOPS data points are clearly visible. The transit model gave a radius of $R_{\mathrm{b}} = 1.770^{+0.032}_{-0.030}\ R_{\oplus}$ for HD 15337 b and $R_{\mathrm{c}} = 2.526^{+0.075}_{-0.086}\ R_{\oplus}$ for HD 15337 c. The RV model fit is displayed in Figure 3.9, resulting in a mass of $M_{\mathrm{b}} = 6.519^{+0.41}_{-0.40}\ M_{\oplus}$ for HD 15337 b and $M_{\mathrm{c}} = 6.79^{+1.30}_{-1.14}\ M_{\oplus}$ for HD 15337 c.

TABLE 3.3: HD 15337 system parameters from the joint fit of transits and RVs. Adapted from Rosário et al. (2024).

Parameters	Prior	Posterior
Model stellar parameters		
$\rho_\star$ ($\rho_\odot$)	$\mathcal{N}(1.344, 0.076)$	$1.334^{+0.075}_{-0.079}$
$u_{1,\mathrm{TESS}}$	$\mathcal{N}(0.47621, 0.00145)$	$0.4761^{+0.0015}_{-0.0012}$
$u_{2,\mathrm{TESS}}$	$\mathcal{N}(0.12172, 0.00220)$	$0.1219^{+0.0024}_{-0.0027}$
$u_{1,\mathrm{CHEOPS}}$	$\mathcal{N}(0.61973, 0.00133)$	$0.6198^{+0.0013}_{-0.0012}$
$u_{2,\mathrm{CHEOPS}}$	$\mathcal{N}(0.0696, 0.00182)$	$0.0696^{+0.0018}_{-0.0019}$
RV model parameters		
v_0 ($\mathrm{km\,s^{-1}}$)	$\mathcal{U}(-4.0, 0.0)$	$-3.8292^{+0.0033}_{-0.0042}$
Derived stellar parameters		
$M_\star$ ($M_\odot$)	–	0.829 ± 0.038
$R_\star$ ($R_\odot$)	–	0.855 ± 0.008
T_{eff} (K)	–	5131 ± 74
Model parameters of HD 15337 b		
$R_\mathrm{b}/R_\star$	$\mathcal{U}(0.01, 0.03)$	$0.01898^{+0.00030}_{-0.00026}$
P_b (days)	$\mathcal{U}(4.7555, 4.7565)$	$4.7559804^{+0.0000062}_{-0.0000037}$
$T_{0,\mathrm{b}}$ (BJD-2457000)	$\mathcal{U}(1411.457, 1411.467)$	$1411.4623^{+0.0008}_{-0.0013}$
e_b	$\beta(0.867, 3.03)$	$0.058^{+0.022}_{-0.016}$
b_b	$\mathcal{U}(0.0, 2.0)$	$0.17^{+0.13}_{-0.11}$
K_b ($\mathrm{km\,s^{-1}}$)	$\mathcal{U}(0.0, 0.01)$	0.00282 ± 0.00015
Derived parameters of HD 15337 b		
$i(^\circ)$	–	$89.30^{+0.48}_{-0.57}$
e	–	$0.058^{+0.022}_{-0.016}$
$\omega(^\circ)$	–	$71.62^{+52.51}_{-40.30}$
R_b ($R_\oplus$)	–	$1.770^{+0.032}_{-0.030}$
M_b ($M_\oplus$)	–	$6.52^{+0.41}_{-0.40}$
ρ_b ($\mathrm{g\,cm^{-3}}$)	–	$6.46^{+0.52}_{-0.51}$
Model parameters of HD 15337 c		
$R_\mathrm{c}/R_\star$	$\mathcal{U}(0.01, 0.04)$	$0.02707^{+0.00091}_{-0.00077}$
P_c (days)	$\mathcal{U}(17.180, 17.181)$	$17.180546^{+0.000021}_{-0.000026}$
$T_{0,\mathrm{b}}$ (BJD-2457000)	$\mathcal{U}(1414.545, 1414.555)$	$1414.55162^{+0.0015}_{-0.0014}$
e_c	$\beta(0.867, 3.03)$	$0.096^{+0.059}_{-0.045}$
b_c	$\mathcal{U}(0.0, 2.0)$	$0.89^{+0.08}_{-0.07}$
K_c ($\mathrm{km\,s^{-1}}$)	$\mathcal{U}(0.0, 0.01)$	$0.00192^{+0.00036}_{-0.00032}$
Derived parameters of HD 15337 c		
$i(^\circ)$	–	88.41 ± 0.07
e	–	$0.096^{+0.059}_{-0.045}$
$\omega(^\circ)$	–	$56.63^{+77.89}_{-63.30}$
R_c ($R_\oplus$)	–	$2.526^{+0.086}_{-0.075}$
M_c ($M_\oplus$)	–	$6.79^{+1.30}_{-1.14}$
ρ_c ($\mathrm{g\,cm^{-3}}$)	–	$2.30^{+0.51}_{-0.41}$
Additional Model Parameters		
$\Delta RV_{\mathrm{HARPS\_1}}$ ($\mathrm{km\,s^{-1}}$)	$\mathcal{N}(0.022, 0.01)$	$0.0187^{+0.0020}_{-0.0019}$
ΔRV_{PFS} ($\mathrm{km\,s^{-1}}$)	$\mathcal{N}(3.815, 0.01)$	3.8137 ± 0.0021
P_{sin} (days)	$\mathcal{U}(5500, 170000)$	19557^{+3425}_{-2612}
K_{sin} ($\mathrm{km\,s^{-1}}$)	$\mathcal{U}(0, 0.025)$	$0.0177^{+0.0044}_{-0.0038}$

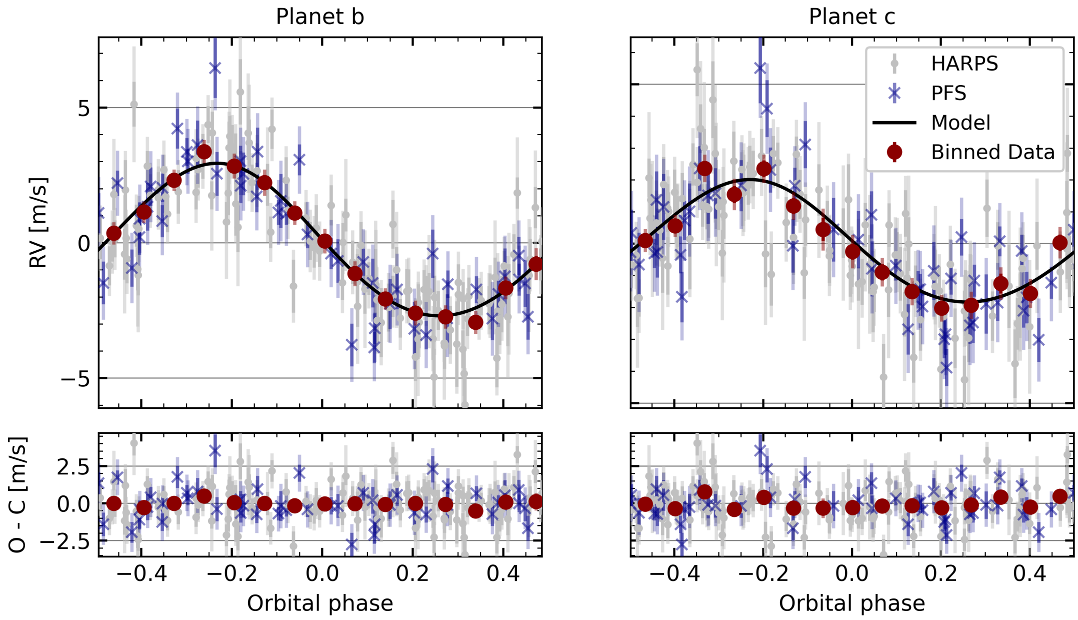

Figure 3.6: Phase-folded radial velocity curves. The grey dots show the HARPS measurements and the blue crosses show the PFS RVs. The binned data is shown in the red circles and the model corresponding to the median of the posterior of each parameter of the Keplerian signal is overplotted in black. *Left:* HD 15337 b; *right:* HD 15337 c. Originally published in Rosário et al. (2024).

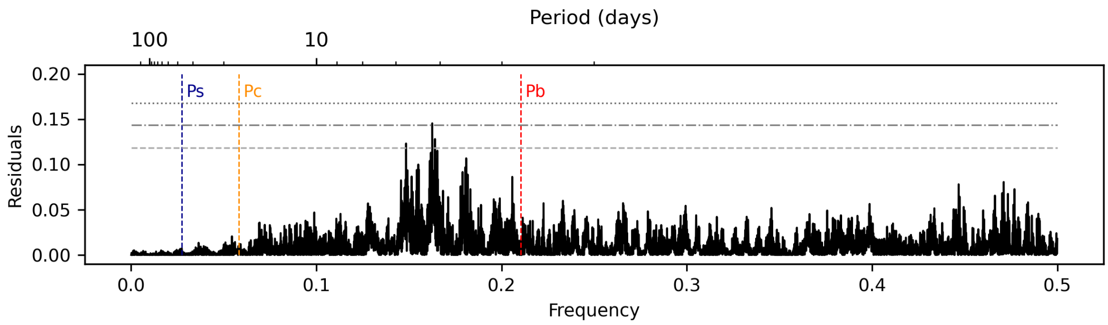

Figure 3.7: Periodogram of the residuals from the RV fit. Horizontal lines show the FAP thresholds as in Figure 3.5. Originally published in Rosário et al. (2024).

The most crucial values we want to obtain from this work are mass and radius, and the precision of these values will be vital for the subsequent calculation of these planets' internal structures. The radius shows a precision below 3% in both planets, which corresponds to the desired threshold (e.g. Otegi et al., 2020; Rauer et al., 2024). The mass of HD 15337 b measured with this approach has a high precision, with an uncertainty of only 6.5%, significantly lower than measured before. However, even with the joint fit and the stellar activity corrections, we are unable to improve on the uncertainties in the mass of HD

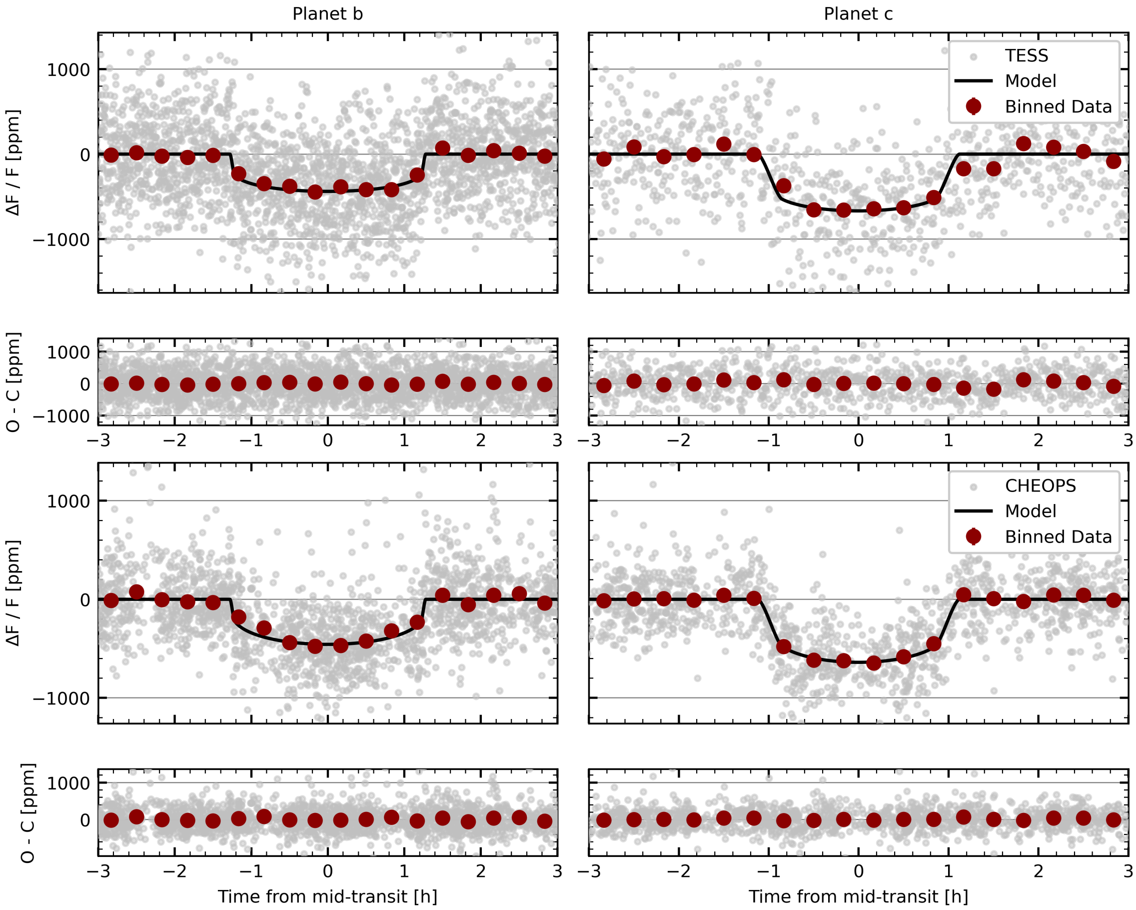

FIGURE 3.8: Phase-folded light curves from TESS (upper panels) and CHEOPS (lower panels) and correspondent residuals. A binning of 20 minutes is shown in the red circles and the model corresponding to the median of the posterior of each parameter transit model is overplotted in black. *Left:* HD 15337 b; *right:* HD 15337 c. Originally published in Rosário et al. (2024).

TABLE 3.4: Summary of the results and comparison with previous studies of HD 15337.

Parameter	Gandolfi et al. (2019)	Dumusque et al. (2019)	Teske et al. (2021)	Rosário et al. (2024)
HD 15337 b				
R_b ($R_\oplus$)	1.64 ± 0.06 (3.7%)	$1.699^{+0.062}_{-0.059}$ (3.6%)	1.67 ± 0.14 (8.4%)	$1.770^{+0.032}_{-0.030}$ (1.7%)
M_b ($M_\oplus$)	$7.51^{1.09}_{-1.01}$ (14.0%)	7.20 ± 0.81 (11.3%)	6.88 ± 0.97 (14.1%)	$6.52^{+0.41}_{-0.40}$ (6.2%)
ρ_b ($\mathrm{g\,cm^{-3}}$)	$9.30^{+1.81}_{-1.58}$ (18.2%)	$8.05^{+1.93}_{-1.61}$ (22.0%)	–	$6.46^{+0.52}_{-0.51}$ (8.0%)
HD 15337 c				
R_c ($R_\oplus$)	2.39 ± 0.12 (5.0%)	$2.52^{+0.11}_{-0.10}$ (4.1%)	2.47 ± 0.23 (9.3%)	$2.526^{+0.086}_{-0.075}$ (3.2%)
M_c ($M_\oplus$)	$8.11^{+1.82}_{-1.69}$ (21.6%)	8.79 ± 1.68 (19.1%)	6.76 ± 2.94 (43.5%)	$6.79^{+1.30}_{-1.14}$ (18.0%)
ρ_c ($\mathrm{g\,cm^{-3}}$)	$3.23^{+0.90}_{-0.72}$ (25.1%)	$3.02^{+1.09}_{-0.87}$ (32.5%)	–	$2.30^{+0.50}_{-0.41}$ (20.0%)

15337 c, which stand at 18%. Our results are summarised in Table 3.4, which compares the mass, radius and density obtained in this analysis with the previous studies and shows the improvement in precision.

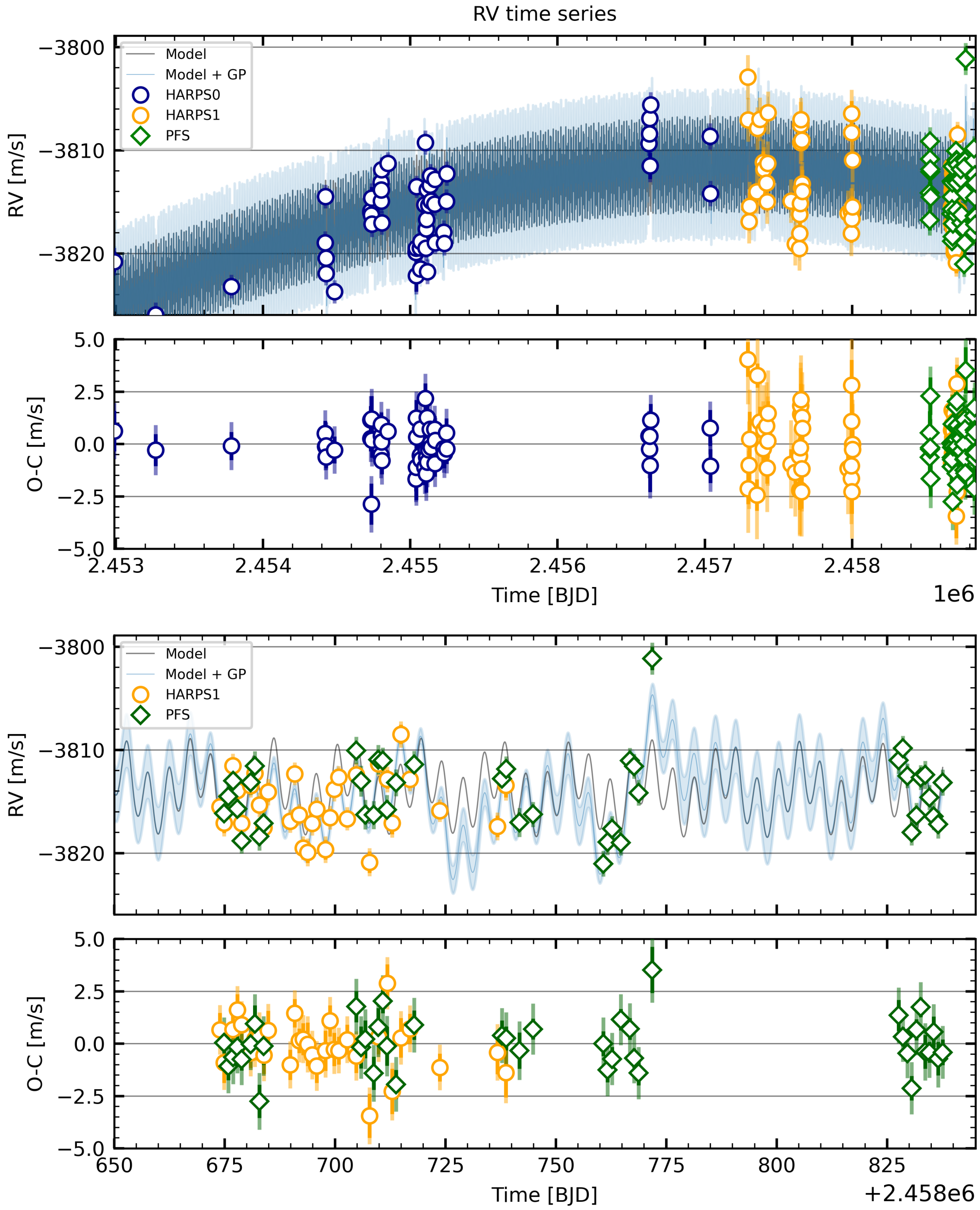

FIGURE 3.9: Full RV time series for HD 15337. Each color represents one of the different datasets, with the blue line representing the model corresponding to the median of the posterior of each parameter model. The shaded light-blue area shows the uncertainty associated to the GP model for the stellar activity corrections. *Bottom panels*: Zoom on the most recent HARPS and PFS data. Originally published in Rosário et al. (2024).

3.6 Internal structure analysis of the HD 15337 system

The internal structure analysis presented in this section was performed by a team from the University of Bern in the CHEOPS consortium.

In this work, we use the model introduced in Leleu et al. (2021) to compute the internal structure of the two planets in the HD 15337 system. The model consists of two parts: the forward model and the Bayesian retrieval model. The forward model calculates the radius of the planet based on the RV semi-amplitude, composition and stellar abundances. The retrieval model, on the other hand, employs a Bayesian inference framework to sample the parameter space of internal structure parameters and takes the sampled parameters, the RV semi-amplitude and the stellar composition, comparing the resulting transit depth with the observed value. In this framework, both planets are run at the same time, taking into account their possibly similar formation history.

The forward model assumes a spherically symmetrical planet composed of four layers: an iron-suflur core modelled with the equations of state (EoS) from Hakim et al. (2018), a silicate mantle with the EoS of Sotin et al. (2007), a water layer using EoS from Haldemann et al. (2020), which includes solid, liquid, gas and supercritical phases, and an gas envelope of pure H/He according to Lopez & Fortney (2014). To help breaking the high degeneracies of this type of model, it can also be assumed that the Si/Mg/Fe ratios of each planet are the same as the host star (Thiabaud et al., 2015). It is however important to note that, as shown in Adibekyan et al. (2021), the relationship between the star and planet composition might be different than the 1:1 ratio we assume. The implications of this assumption will be further discussed when analysing the results of the HD 15337 system in Section 3.7.

The Bayesian retrieval model uses the stellar age, mass, radius, effective temperature and abundances of the star and the transit depth, period and RV semi-amplitude of the planet. The stellar parameters are used as the main input to compute the thickness of the H/He layer, which also depends on the irradiation of the star. The model outputs the following parameters: the mass fractions of the core ($\mathrm{fm_{core}}$) and water layer ($\mathrm{fm_{water}}$) relative to the solid part of the planet, the molar fractions of Si and Mg in the mantle ($\mathrm{Si_{mantle}}$ and $\mathrm{Mg_{mantle}}$) and iron in the core ($\mathrm{Fe_{core}}$), the mass of the gas layer in logarithm scale ($\log \mathrm{M_{gas}}$) and the thickness of the gas layer. Additional parameters can be inferred from these, like the iron mass fraction in the mantle.

The retrieval model requires the calculation of the planet radius for millions of parameter combinations to infer the posterior distributions. This process is shown to be extremely consuming in terms of both time and computation resources. Therefore, the novelty lies in the use of a deep neural network (DNN) to increase the efficiency of the calculation and speed up the process. More details in the DNN setting used in the model can be seen in Leleu et al. (2021). An improved version of the model used in this work is publicly available* and is described in detail in Egger et al. (2024). The main difference in this updated framework is the use of the BICEPS model from Haldemann et al. (2024) as the forward model.

The priors of the free parameters are all set as uniform within physically realistic limits and listed in Table 3.5. We set the upper limit of the water mass fraction prior as 0.5, since it is assumed to never be higher than 50% (Thiabaud et al., 2014; Marboeuf et al., 2014). The prior on the mass of the gas envelope is uniform in a log scale. The mass fraction priors are not defined as independent priors. Instead, samples are drawn uniformly from the triangular simplex under the condition that the total mass fractions must equal one.

$$\mathrm{fm}_{\mathrm{core}} + \mathrm{fm}_{\mathrm{mantle}} + \mathrm{fm}_{\mathrm{water}} = 1 \tag{3.2}$$

Figures 3.10 and 3.11 show the corner plots with the posterior distributions of the internal structure analysis of HD 15337 b and c, with the errors corresponding to the 5th and 95th percentiles. The remaining mass fractions and compositional abundances can be obtained directly from this set of parameters during post-processing. A summary of all results is listed in Table 3.5.

The core mass fraction of both planets is similar, giving a value of $0.14^{+0.13}_{-0.12}$ for planet b and $0.11^{+0.13}_{-0.10}$ for planet c. According to the model, planet b appears to have a thin water layer with a mass fraction ($\mathrm{fm}_{\mathrm{water}}$) of $0.10^{+0.10}_{-0.08}$, while planet c shows a posterior favouring higher values (despite unconstrained by the data), with a water mass fraction of $0.28^{+0.20}_{-0.24}$. The latter is also shown to have a significant gas layer with a mass of $\mathrm{m}_{\mathrm{gas}} = 0.03^{+0.04}_{-0.02}\ M_{\oplus}$ and a thickness of $0.60^{+0.18}_{-0.29}\ R_{\oplus}$.

*https://github.com/joannegger/plaNETic

Table 3.5: Priors used for the internal structure modelling and corresponding posteriors with error bars corresponding to the 5% and 95% percentiles. Originally published in Rosário et al. (2024).

Parameters	Prior	Posterior
HD 15337 b		
$\mathrm{fm}_{\mathrm{core,b}}$	$\mathcal{U}(0.0, 1.0)$	$0.14^{+0.13}_{-0.12}$
$\mathrm{fm}_{\mathrm{mantle,b}}$	$\mathcal{U}(0.0, 1.0)$	$0.75^{+0.15}_{-0.14}$
$\mathrm{fm}_{\mathrm{water,b}}$	$\mathcal{U}(0.0, 0.5)$	$0.10^{+0.10}_{-0.08}$
$\log \mathrm{m}_{\mathrm{gas,b}}$ ($\mathrm{M}_\oplus$)	$\mathcal{U}(-12, \log(0.5\ \mathrm{M_b}))$	$-9.02^{+3.02}_{-2.68}$
$\mathrm{Si}_{\mathrm{mantle,b}}$		$0.40^{+0.08}_{-0.06}$
$\mathrm{Mg}_{\mathrm{mantle,b}}$		$0.44^{+0.11}_{-0.10}$
$\mathrm{Fe}_{\mathrm{core,b}}$	$\mathcal{U}(0.81, 1.00)$	$0.90^{+0.09}_{-0.08}$
HD 15337 c		
$\mathrm{fm}_{\mathrm{core,c}}$	$\mathcal{U}(0.0, 1.0)$	$0.11^{+0.13}_{-0.10}$
$\mathrm{fm}_{\mathrm{mantle,c}}$	$\mathcal{U}(0.0, 1.0)$	$0.60^{+0.19}_{-0.26}$
$\mathrm{fm}_{\mathrm{water,c}}$	$\mathcal{U}(0.0, 0.5)$	$0.28^{+0.20}_{-0.24}$
$\log \mathrm{m}_{\mathrm{gas,c}}$ ($\mathrm{M}_\oplus$)	$\mathcal{U}(-12, \log(0.5\ \mathrm{M_c}))$	$-1.53^{+0.40}_{-0.74}$
$\mathrm{Si}_{\mathrm{mantle,c}}$		$0.41^{+0.08}_{-0.06}$
$\mathrm{Mg}_{\mathrm{mantle,c}}$		$0.44^{+0.11}_{-0.10}$
$\mathrm{Fe}_{\mathrm{core,c}}$	$\mathcal{U}(0.81, 1.00)$	$0.90^{+0.09}_{-0.08}$

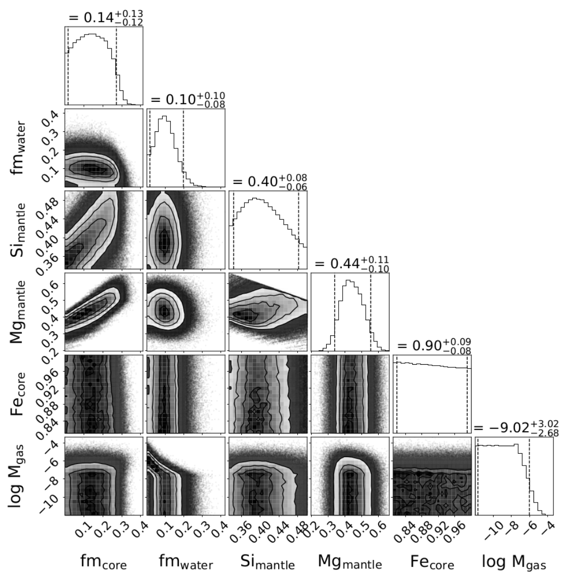

Figure 3.10: Posterior distribution of the internal structure parameters for HD 15337 b. Originally published in Rosário et al. (2024).

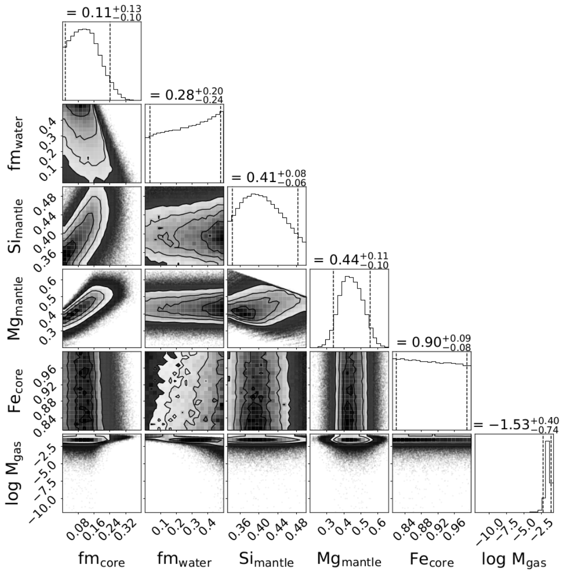

Figure 3.11: Same as Figure 3.10 but for HD 15337 c. Originally published in Rosário et al. (2024).

3.7 Discussing the results

Mass and radius precision and impact in internal structure

One of the goals of this work is to improve the precision on radius and mass of the planets. As mentioned before, current internal structure models, like the one used in this work, are highly degenerate and the same radius and mass can lead to several different combinations of layers. A good precision in radius and mass is therefore relevant to reduce the number of possible outcomes (e.g. Dorn et al., 2017; Otegi et al., 2020). It has been shown by Otegi et al. (2020) that an improvement in the mass uncertainties can significantly improve the constrain in the core mass fraction of planets with a density higher than the Earth, while an improvement in the radius precision has an impact in the constrain of the atmosphere layer, especially in the case of sub-Neptunes. With the new CHEOPS results and the increased precision compared to TESS, the radius of HD 15337 b went from the $\sim 3.5\%$ uncertainty from Gandolfi et al. (2019) and Dumusque et al. (2019) to just 1.7%, making it one of the more precise radius measurements for super-Earths. HD 15337 c also had an improvement on the error bar for the radius, reaching a precision around 3% (see Table 3.4).

The results in Table 3.4 also show the precision level on the mass of HD 15337 b is significantly improved with the new RV data, going from 11-14% in Gandolfi et al. (2019) and Dumusque et al. (2019), to around half that value (6.2%). The improvement in HD 15337 c is not as significant, with an uncertainty of 18% compared to 19-22% from the previous papers.

The additional data points from HARPS and PFS also improve the constrain on the long-term trends and stellar activity signals which lead to a better fit of the RV signal of the two planets with smaller error bars.

Internal structure and composition

The mass-radius (MR) diagram plotted in Figure 3.12 shows the position of HD 15337 b and HD 15337 c compared to other well characterised small planets. Two main populations are seen, with HD 15337 b located on the upper limit of the super-Earth population that is below the radius valley (Fulton et al., 2017), lying close to the pure silicate line, hinting at a silicate heavy composition. HD 15337 c is part of the sub-Neptune population, which

https://exoplanetarchive.ipac.caltech.edu, retrieved on April 27, 2023.

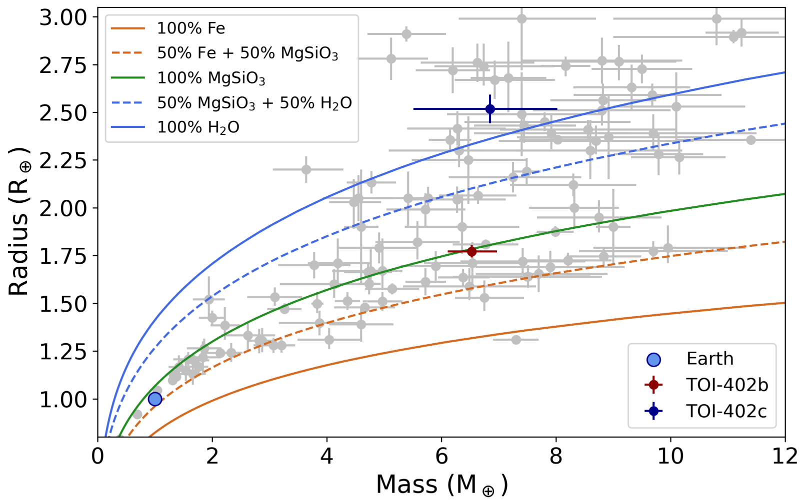

Figure 3.12: Mass-radius plot showing the position of HD 15337 b and HD 15337 c compared to other small exoplanets. The composition models from Zeng et al. (2016) overplotted considering the following compositions: 100% iron (solid orange line); 50% iron and 50% silicate (dashed orange line); 100% silicate (solid green line), 50% silicate and 50% water (dashed blue line); 100% water (solid blue line). Originally published in Rosário et al. (2024).

is located on the other side of the radius valley. It is above the predicted 100% water line, which means the solid models are not enough to explain the radius and therefore it likely harbours a gas envelope. This matches the results from the Bern model in Section 3.6, since there is a H/He layer in planet c with a potentially significant water layer. The line of 100% silicate shown in the plot is purely theoretical as it is not physically reasonable to have 100% silicate planets and as such, the internal structure of HD 15337 b predicted by the Bern model is vastly different and shows a relatively high iron mass fraction, both in the core and the mantle.

The Bern model considers liquid phases in the inner core and the water layer, fixing the temperature to 300 K and pressure to 1 bar outside the water layer, modelling the gas envelope as a separate layer. However, HD 15337 b orbits close to its star and the high irradiation leads to a high equilibrium temperature (∼1000 K), meaning that it is unlikely that the water layer in this planet is fully condensed. A possibility that has to be taken into account in hotter planets is that of a molten mantle layer containing water. The model proposed in Dorn & Lichtenberg (2021) tackles this scenario and the authors conclude that the presence of water in the mantle can lead to an underestimation of the water mass fraction when constrained only by radius and mass, adding an additional scenario to an already complex problem. The water content of a planet and the form it takes is not only relevant to the ever present search for another Earth but also affects dynamic and structural properties, such as the level of internal differentiation (Bonati et al., 2021) and composition of the atmosphere (Gaillard et al., 2021). Using the results from Dorn & Lichtenberg (2021), we predicted that HD 15337 b could have a water mass fraction 15-20% higher than shown in this analysis.

As mentioned before, the degeneracy of the current internal structure models requires additional constrains to try and solve the different outcomes. This can be done by assuming equal values in the abundances of the planets and the star, like we do in the original analysis. However, according to Adibekyan et al. (2021), this relationship is unlikely to be a 1:1 linear correlation, and the Si/Mg/Fe abundances may not match the ones from the star exactly. We made a second analysis of the internal structure in order to compare with the case where the abundances are not constrained. The posterior distributions of this second analysis is found in Figures 3.13 and 3.14.

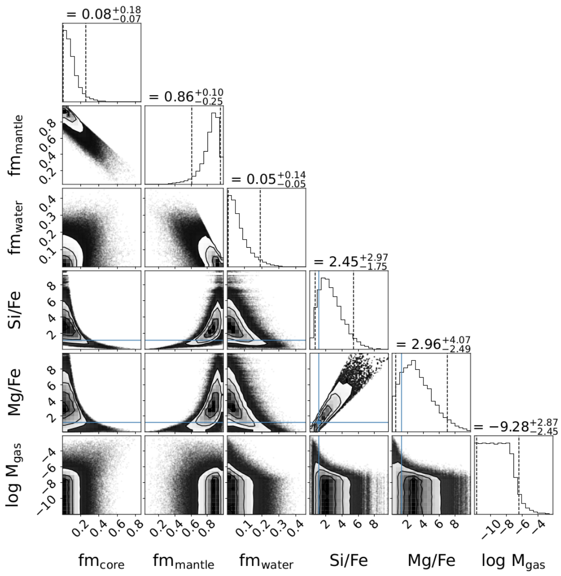

FIGURE 3.13: Posterior distribution of the internal structure parameters for HD 15337 b assuming unconstrained abundances.

With unconstrained abundances, we expect the degeneracy of the models to be even more prominent. While there is a similar range of values in the posterior of the core mass fraction, the distribution appears to favour smaller mass fractions in both planets. The water mass fraction for HD 15337 b is now unconstrained and indistinguishable from zero at 2σ and there is an increase in the maximum values of the mantle mass fraction. The mass of the gas layer of HD 15337 c does not show a significant change.

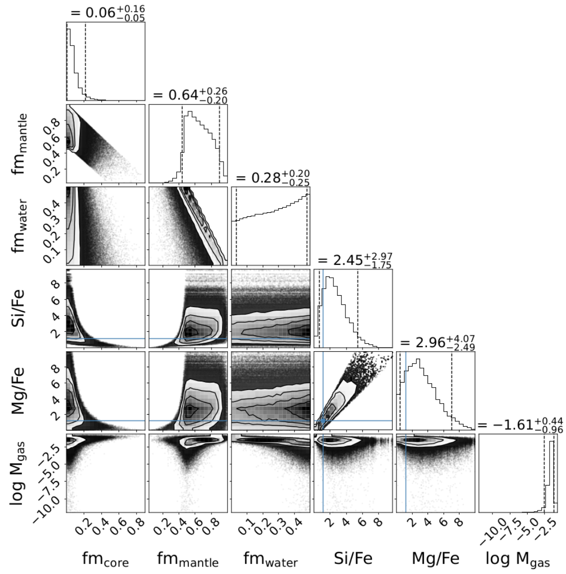

Figure 3.14: Same as Figure 3.10 but for HD 15337 c.

Long-term RV trend

The top plots in Figures 3.4 and 3.5 show a long-term trend with unknown origins in the RV data. In this part of the work we explore possible origins for this trend, with the focus of getting the best possible model to correct the RVs.

One of the main possibilities is that the trend is caused by stellar activity. The trend is present in the FWHM time series as well, which hints towards a signal caused by either stellar activity or a stellar companion. We check the correlation between the RV and the FWHM time series using the Pearson correlation factors and found a strong linear correlation with a p-value of 5×10^{-7}. While we attempt to find the same trend in the $\log R'_{\mathrm{HK}}$ series, it appears that it is not present, with a p-value of 0.25 hinting at no linear correlation between RVs and $\log R'_{\mathrm{HK}}$.

Another possibility is that the star has a close gravitationally bound companion that is producing a stronger RV signal than those of planetary nature. If this companion is planetary in nature, it would not be expected to cause a trend in the FWHM time series, as planetary-mass objects do not significantly alter the stellar line profile. However, if the companion is a star, its spectral contribution could cause detectable variations in the FWHM, particularly if it is an unresolved binary companion. A planetary companion cannot be entirely ruled out, as there is no definitive proof that the observed RV and FWHM trends are caused by the same phenomenon. Additionally, the FWHM trend could be instrumental in origin and thus persist even if the RV signal is induced by a planet.

As explained before, the trend is modelled using a long-period sinusoidal function which yields a period of $53.6^{+9.4}_{-7.2}$ years and a semi-amplitude of $0.0177^{+0.0044}_{-0.0038}$ $\mathrm{km\,s^{-1}}$, at least 10 times greater than the transiting planet signals in the RVs. Based on these values, we estimate the minimum mass of a possible companion responsible for this signal, finding a minimum mass of $M \sin i = 4\ M_{\mathrm{Jup}}$. It is important to note that this star does have a known companion, as discussed in Section 3.3.2. However, it is highly unlikely to be the source of this trend. Given its estimated orbital period of 540 years (Lester et al., 2021), this companion would not be expected to produce a detectable trend over the 16-year period of HARPS observations, unless its orbit is highly eccentric.

We also estimate the amplitude of the signal the known companion would cause in the RVs of the primary star, using the mass ratio of 0.14 from Lester et al. (2021) to estimate the mass of the secondary. The amplitude would be an order of magnitude higher than what is seen in the data. However, it is important to note that the sinusoidal model effectively represents a circular orbit, whereas an eccentric orbit could still theoretically produce a similar trend, making the true origin of the signal uncertain. As mentioned before, a second-degree polynomial was also considered, as in Gandolfi et al. (2019), and it provides consistent results (at 1σ) when comparing with the sinusoidal model. Ultimately, the sinusoidal model offers more constraints and a more direct interpretation in the case of a gravitationally bound companion, making it the preferred choice.

Summary and conclusions

In summary, with this work we provide an improved constrain on radius, mass and internal structure of HD 15337 b and c, achieving important thresholds of precision that allow a strong basis for further studies. Further observations from missions such as PLATO or JWST could improve the results of the internal structure models and maybe confirm the presence of a water layer in planet b or provide a better insight into the atmospheric characterisation.

Chapter 4

Characterisation of hot Jupiters

This section was originally published as: Rosário, N. M., et al., *Measuring the orbit shrinkage rate of hot Jupiters due to tides*, Astronomy & Astrophysics 668 (2022): A114 (Rosário et al., 2022).

4.1 Introduction

When a planet orbits too close to its star, the proximity of the two bodies generates a strong interaction between them, owing to both intense irradiation and powerful tidal forces. As discussed in Chapter 1, tidal interaction can have a variety of effects, and in this part of the work we focus on the effect it has on the planet's orbit. Characterising the orbit can reveal vital information about stellar physics and planet-star interaction and help understand planet migration and system dynamics.

In the next sections, we analyse two candidates that are predicted to show signs of orbital decay due to tides. We present the process leading to the selection of the most promising targets, update their planetary parameters using recent data from TESS, and search for transit timing variations (TTVs) to potentially confirm tidal decay in these systems, updating the tidal quality factor of the star with the new results.

4.2 Target selection

It was proposed that planets orbiting cooler stars may experience stronger tidal dissipation due to their larger convective envelopes, causing a rapid decay of the planets' orbits (e.g. Weinberg et al., 2017; Patra et al., 2020). Therefore, studying the presence of tidal decay in stars with different temperatures can help compare the decay rate and confirm this

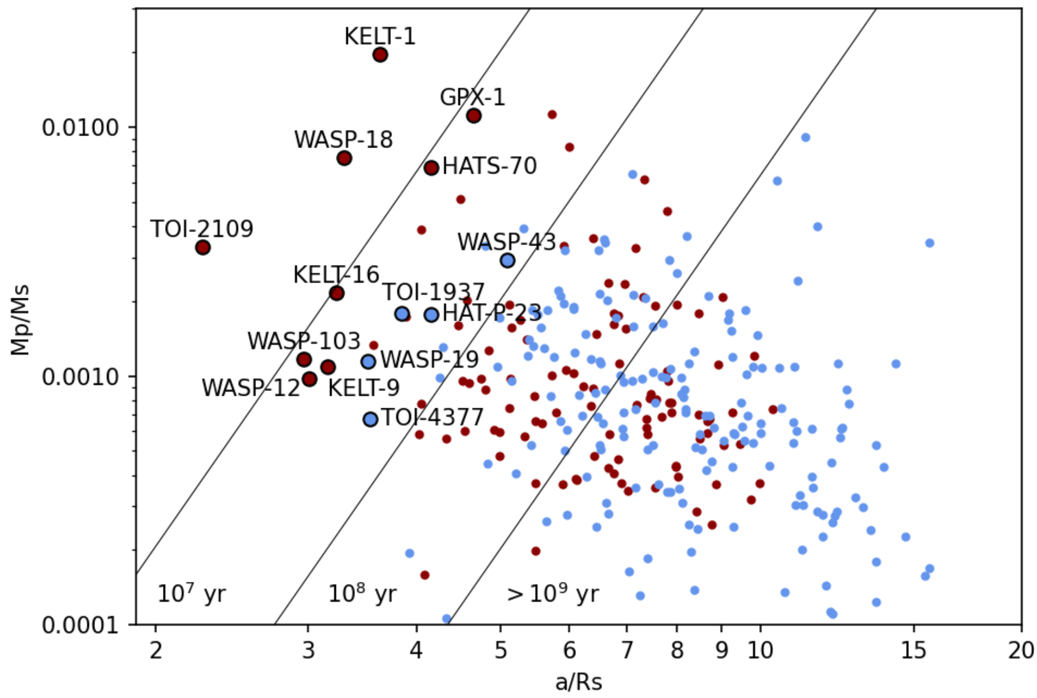

FIGURE 4.1: Main candidates to detect orbital decay, plotted with the expected decay timescale assuming a $Q'_\star = 10^6$ and a period of 1 day, highlighting the most promising candidates. The red dots represent stars with $T_{\text{eff}} > 6000K$, with blue dots used for cooler stars.

hypothesis. The targets highlighted in Figure 4.1 are the main candidates to be part of the study and they provide ideal conditions in a theoretical basis to find orbital decay due to tides. TOI-2109 (Wong et al., 2021) has the shortest known orbital period of any hot Jupiter around a Sun-like star ($P = 0.672$ days), making it a prime candidate for tidal decay. However, as its discovery is fairly recent, it lacks data over a large enough time frame that would allow the detection of change in period. Nevertheless, it is one of the main targets for current and future missions to obtain more transits and monitor its orbit. WASP-12b (Hebb et al., 2009a) was the first hot Jupiter with confirmed orbital decay due to tidal interaction. Previous extensive analysis of WASP-12b phase curve have found strong evidence of a decaying orbit (e.g. Turner et al., 2021b; Wong et al., 2022; Akinsanmi et al., 2024) and at the time of publication of this work, two recent analyses with TESS data had just been released, reducing the impact of a new study (Turner et al., 2021b; Wong et al., 2022).

Recent analyses using TESS and CHEOPS data have also searched for tidal effects in WASP-103b (e.g. Gillon et al., 2014; Barros et al., 2022b), and Barros et al. (2022b) confirmed the presence of tidal deformation, making it into the first hot Jupiter with measured deformation from transit light curves. This target, as WASP-12b, is excluded from this study due to recent works overlapping with our goal of improving constrains on orbital decay.

The same can be said about KELT-9b (Gaudi et al., 2017), KELT-16b (Oberst et al., 2017), WASP-4b (Wilson et al., 2008) and WASP-43b (Hellier et al., 2011a), which are potential decay targets with recent publications using TESS data at the time this work was developed (Turner et al., 2021a; Davoudi et al., 2021; Mancini et al., 2022; Harre et al., 2023).

Finally, KELT-1b (Siverd et al., 2012) has a very high mass ($M = 27.7\ M_{\rm Jup}$) and falls in a mass range that makes its classification as a super-massive planet or a low-mass brown dwarf particularly unclear, with different criteria resulting in different classifications (e.g. Siverd et al., 2012; Maciejewski et al., 2018; Baştürk et al., 2023). The high mass ratio would make KELT-1b one of the prime candidates to experience tidal decay. However, the rotation period of the star indicates a fully synchronised or close to synchronised companion-host system (Siverd et al., 2012; Von Essen et al., 2021), leading us to exclude this candidate from our target list.

With its high $M_{\rm p}/M_\star$ ratio, WASP-18 is identified as one of the best targets to measure tidal decay amongst the initial selection of hot stars. Furthermore, TESS observed the system in a total of four sectors, providing a significant amount of new transits to work with, and has been the topic of multiple decay studies with a large history of observations (e.g. Shporer et al., 2019; Maciejewski et al., 2020). For our second target we chose WASP-19, one of the most promising targets orbiting cooler stars. It was observed by TESS in two sectors and has been studied for several years (e.g. Mancini et al., 2013; Espinoza et al., 2019), including observations from several instruments in photometry and spectroscopy, owing in part to the star's significant activity levels.

4.2.1 WASP-18

WASP-18b (TIC 100100827; Hellier et al., 2009; Southworth et al., 2009) is one of the most massive known hot Jupiters, with a mass of $10.2 \pm 0.35\ M_{\rm J}$ and a radius of $1.24 \pm 0.08\ R_{\rm J}$ (Cortés-Zuleta et al., 2020). The planet orbits a bright F-type star with a magnitude of

$V = 9.3$, a mass of $1.29 \pm 0.06\ M_{\odot}$ and a temperature of 6432 ± 48 K (Cortés-Zuleta et al., 2020) ,putting it into the hot star category defined before.

The system has been extensively characterised in previous studies (e.g. Shporer et al., 2019; Maciejewski et al., 2020), and according to the theoretical models it is expected to be one of the fastest decaying hot Jupiters known. Despite this, no clear evidence of decay has been found for WASP-18b until now. Wilkins et al. (2017) found no evidence of decay in an initial study and while McDonald & Kerins (2018) included an early transit observed by *Hipparcos*, reporting a weak sign of decay at 1σ, the high uncertainty in the timing of the *Hipparcos* transit can significantly affect the result and constrain a more precise measurement of the decay rate. Shporer et al. (2019) and Maciejewski et al. (2020) more recently used the first TESS observations of WASP-18 (sectors 2 and 3), but the results were consistent with the earlier findings, with no evidence of orbital decay in WASP-18b.

4.2.2 WASP-19

WASP-19b (TIC 35516889, Hebb et al., 2009b) is one of the most promising tidal decay targets orbiting colder stars. It has a mass of $1.15 \pm 0.08\ M_{\mathrm{J}}$ and a radius of $1.41 \pm 0.05\ R_{\mathrm{J}}$ (Cortés-Zuleta et al., 2020) and orbits a very active G-type star, with a mass of $0.97 \pm 0.09\ M_{\odot}$ and a temperature of 5616 ± 66 K (Cortés-Zuleta et al., 2020). WASP-19b has one of the shortest periods recorded to date, orbiting its star every 0.78 days, which could indicate a strong tidal interaction and a faster decay. However, the star's high activity levels make it challenging to detect TTVs and measure orbital decay reliably, and previous studies have yielded inconsistent results for this system. Several authors have analysed WASP-19b transits to search for TTVs (e.g. Mancini et al., 2013; Espinoza et al., 2019). Later, Patra et al. (2020) incorporated additional transit observations, reporting a potential period change. However, this hypothesis was challenged by Petrucci et al. (2020), whose independent analysis based on additional transit data showed a strong preference for a constant period model. There have been inconsistencies in the extracted transit parameters as well, with Tregloan-Reed et al. (2013) finding inconsistent radius measurements in consecutive light curves, that could be attributed to the presence of star spots during the transits. With the additional precise timings from TESS, we aim to further constrain the transit parameters and to the decay rate, providing a stronger evidence towards the presence or absence of orbital decay.

4.3 TESS observations and data pre-processing

4.3.1 Observations

TESS observed WASP-18 at a 2 minute cadence in four sectors (2, 3, 29 and 30) between 2018 and 2020, covering a total of 92 transits (Figure 4.2). We also obtained the 56 transits from the TESS observations of WASP-19, observed at the same cadence in sectors 9 and 36, from 2019 to 2021 (Figure 4.3).

As done for the analysis of HD 15337 system in Chapter 3, we use the PDCSAP corrected light curves in this work and follow the same preliminary removal of bad quality measurements (see section 2.1.2 for more details).

The PDCSAP light curves after the removal of low quality points and NaNs are plotted in Figures 4.2 and 4.3 for WASP-18 and WASP-19 respectively. Some incomplete transits are present, particularly when close to the central gaps separating the two physical orbits from TESS. These incomplete transits are removed during the light curve preprocessing outlined in the next section to be conservative, since a precise derivation of the transit timing is difficult when there is an incomplete transit and it may introduce biases (Barros et al., 2013).

4.3.2 Pre-processing and stellar activity correction

The TESS light curves are obtained through almost continuous observations of the target star, meaning that there are a lot of out-of-transit data points. These measurements are taken into account as a way to obtain the out-of-transit flux, relative to which the transit depth is calculated. In the case of WASP-19 particularly, the light curves show significant variability in the measured flux throughout the observation window (see Figure 4.3), which can be linked to the high levels of stellar activity. In order to mitigate the effect of the stellar activity and the long-term fluctuations seen in the light curves, we employ the pre-processing methodology presented in Section 2.1.2.

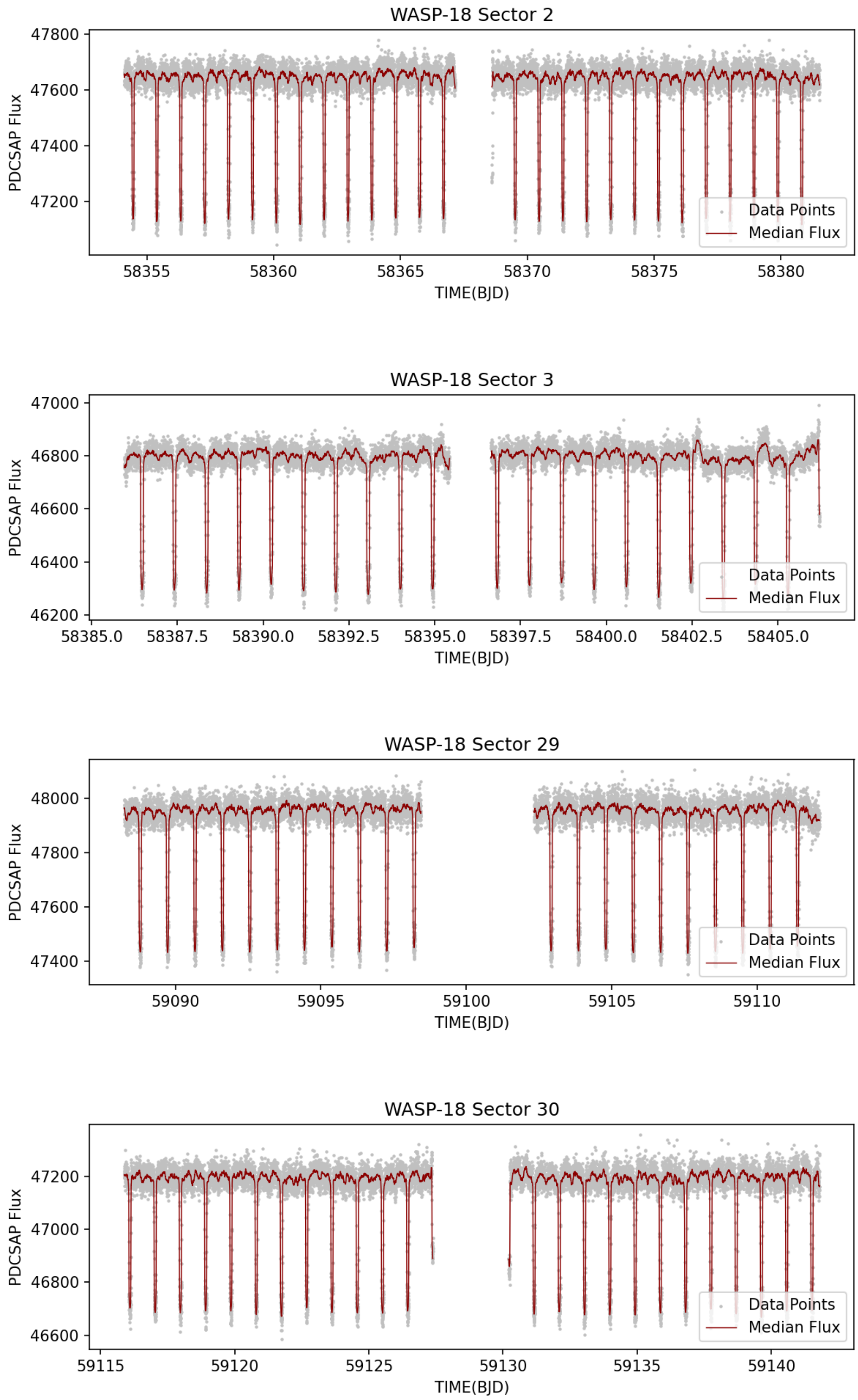

FIGURE 4.2: Plot of the PDC light curves of WASP-18 with NaNs and quality flagged points removed. A moving median filter over 32 points is shown in red. Originally published in Rosário et al. (2022).

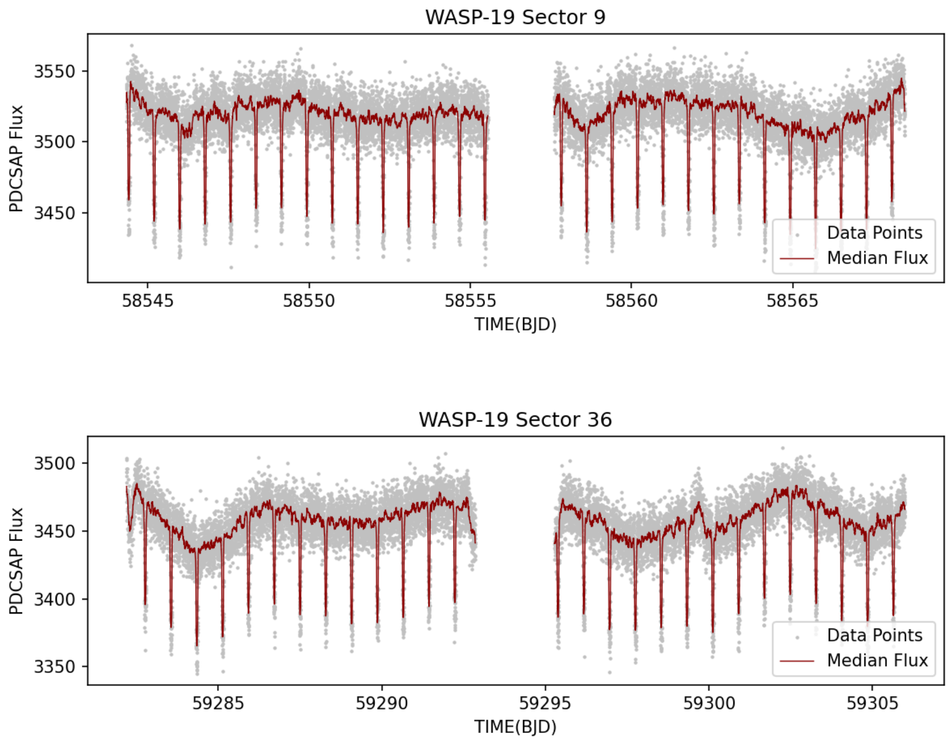

Figure 4.3: Same as Figure 4.2 for WASP-19. Originally published in Rosário et al. (2022).

4.4 Data analysis

This work is divided in two main parts. We first perform a fit of the transit model using `batman` to the TESS data and derive precise transit parameters for each planet. Refining the transit shape parameters allows for a better estimation of the individual transit times, which are then used together with other times found in the literature to perform a TTV analysis and constrain the change in period and the tidal decay parameters of each planet.

4.4.1 Transit analysis

In the transit part of the analysis, we fit all detrended individual transits simultaneously for P, T_0, $R_\mathrm{p}/R_\star$, $\cos i$ and the limb-darkening coefficients u_1 and u_2 using the quadratic law described in Section 2.1.3. As both WASP-18b and WASP-19b orbit very close to their star, the time it takes to circularise their orbit (circularisation timescale) is significantly shorter than the age of the systems, in the order of 15 Myr for WASP-18b and 2 Myr for WASP-19b. With both orbits expected to be circular at the current age, we assume a fixed eccentricity of $e = 0$ with a fixed $\omega = 90°$. To further validate our assumption, we also perform a fit using Gaussian priors for e and ω, with the mean and error obtained from previous analyses of secondary eclipses in the literature (WASP-18b, Nymeyer et al. 2011; WASP-19, Hellier et al. 2011b) and use the BIC to compare both models. The circular model is shown to be preferred for both planets over the one with free eccentricity, and for this reason we use the circular model in the analyses described next.

TABLE 4.1: System parameters and priors used in the transit modelling. Originally published in (Rosário et al., 2022).

Parameter	Prior	Derived Value
WASP-18b		
T_0 (BJD)	$\mathcal{U}(2458021.125, 2458023.125)$	2458022.125237(37)
P (days)	$\mathcal{U}(0.44145, 1.44145)$	0.941452397(44)
$R_p/R_\star$	$\mathcal{U}(0.04776, 0.14776)$	0.09765 ± 0.00017
$a/R_\star$	$\mathcal{U}(1.0, 5.0)$	3.456 ± 0.017
i (°)	$\mathcal{U}(60, 90)$	$83.58^{+0.25}_{-0.24}$
u_1	$\mathcal{N}(0.361712, 0.1)$	0.300 ± 0.020
u_2	$\mathcal{N}(0.158463, 0.1)$	0.159 ± 0.037
WASP-19b		
T_0 (BJD)	$\mathcal{U}(2456020.704, 2456022.704)$	2456021.70386(50)
P (days)	$\mathcal{U}(0.28884, 1.28884)$	0.78883896(14)
$R_p/R_\star$	$\mathcal{U}(0.09233, 0.19233)$	$0.14541^{+0.00070}_{-0.00077}$
$a/R_\star$	$\mathcal{U}(1.0, 5.0)$	$3.533^{+0.039}_{-0.037}$
i (°)	$\mathcal{U}(60, 90)$	$79.17^{+0.33}_{-0.31}$
u_1	$\mathcal{N}(0.435405, 0.1)$	$0.403^{+0.061}_{-0.062}$
u_2	$\mathcal{N}(0.132505, 0.1)$	$0.118^{+0.084}_{-0.082}$

For the transit analysis we employ the MCMC approach with the `emcee` ensemble sampler in Python, detailed in Section 2.3.2. As in the HD 15337 analysis, we define a number of walkers that is 4 times the number of fitted parameters and ran the sampler for 10000 steps. We then discard the initial 1000 samples as burn-in before retrieving the posterior distributions. We define uniform priors for every parameter, with the exception of the limb-darkening coefficients, which are set with Gaussian priors centred in the values from LDTk (with a conservative standard deviation of 0.1), and we add a first-degree polynomial model in the fit to propagate detrending errors and remove any leftover short-term trends in the individual curves.

The priors used in the transit analysis and the correspondent best-fit posteriors are summarised in Table 4.1. The phase-folded light curves with the best-fit transit model for WASP-18b and WASP-19b are shown in Figures 4.4 and 4.5, respectively. For both targets, the updated planetary and transit parameters generally agree with the results from the literature. In the case of WASP-18b, we obtain an agreement with the results of Maciejewski et al. (2020) at a 1σ confidence level for the radius and about 2σ for the other parameters, noting that two of the sectors we use in the analysis are already included in their analysis as well. The transit parameters described in Shporer et al. (2019) have a slightly larger deviation which can be caused by the non-zero eccentricity used in their model.

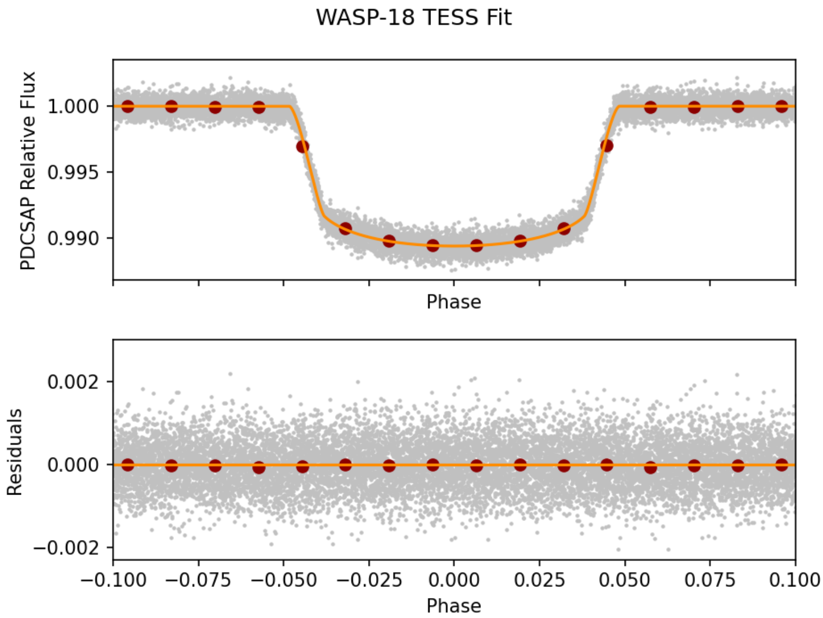

Figure 4.4: Best fit model for WASP-18b phase-folded light curve of all TESS transits. Originally published in Rosário et al. (2022).

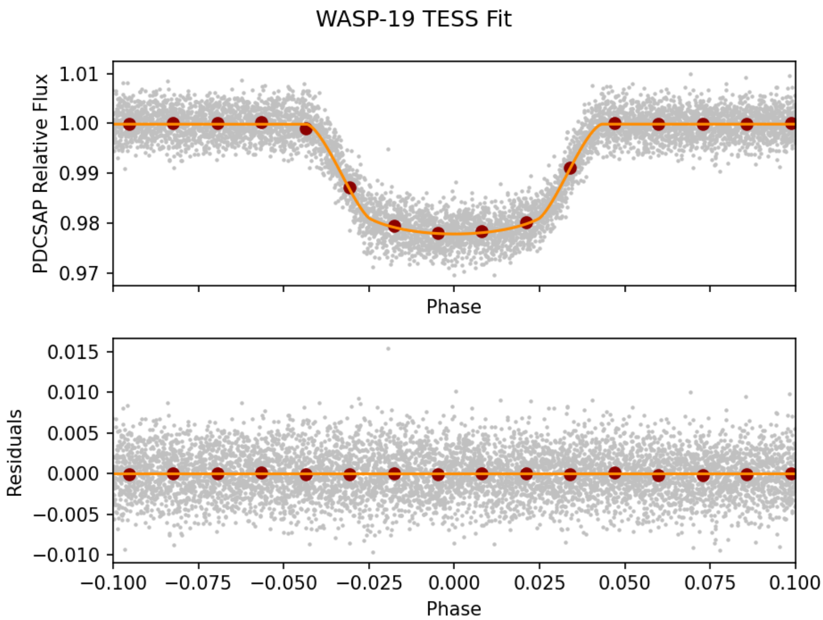

Figure 4.5: Best fit model for WASP-19b phase-folded light curve of all TESS transits. Originally published in Rosário et al. (2022).

WASP-19b transit parameters (except for the radius) agree within 1σ with the ones reported by Espinoza et al. (2019), which are already shown to be in good agreement with the results of Hebb et al. (2009b), Tregloan-Reed et al. (2013) and Mancini et al. (2013). However, the radius we found is inconsistent with the values found in the literature. Wong et al. (2020) found an increase of 10-15% in the transit depth when analysing the data from TESS sector 9, obtaining a value of 23240 ± 260 ppm. To further assess the inconsistencies in the depth estimations, we perform individual fits of sectors 9 and 36 and obtain a considerable depth difference of around 3% between the two sectors, with 21590^{+267}_{-297} ppm in sector 9 and 20996^{+299}_{-344} ppm in sector 36. Our transit depth estimation using both TESS sectors does not deviate as much from the previous ones as the one from Wong et al. (2020), but we still found an increase of over 4% in depth compared to Espinoza et al. (2019) using both TESS sectors (21145^{+211}_{-222} ppm), and over 6% with sector 9 alone. According to Wong et al. (2020), the apparent larger radius may be due to an increase in star spots on the surface during sector 9 observations. Our reduced difference when using only sector 9 data could be attributed to our initial correction with individual transit segments and posterior normalisation, which are designed to reduce the effect of spots. However, the different values obtained for sector 36 suggest the stellar activity is definitely high and producing large fluctuations in the measured transit depths.

Following the initial transit analysis, we perform the individual fit of the transit timings. We set $r_{\rm p}/R_\star$, $a/R_\star$ and i as free parameters in this analysis and fix the previously obtained values for P, u_1 and u_2. For the free parameters, we set Gaussian distributions based on the posteriors from the previous results as the priors for this part of the analysis, and we set a uniform prior for the individual mid-transit timings $T_{\rm mid}$. We use an MCMC approach with the same settings as before, run over 5000 steps for each transit, discarding the initial burn-in. The transit timings are listed in Tables A.1 and A.2 in Appendix A, together with the times retrieved from previous studies in the literature.

4.4.2 Timing and orbital decay analysis

In this section we present the TTV analysis performed to constrain the orbital decay rate of WASP-18b and WASP-19b using our derived times and those obtained from the literature. We note that, while the times were originally published in the references described in the tables in Appendix A, the values used for WASP-18b were derived by Maciejewski et al. (2020) as part of their updated photometric analysis.

In this analysis, we compute the transit time $T_{\rm mid}$ using two models: a Keplerian orbit model, which accounts for a constant orbital period P and a linear ephemeris E (equation 4.1 below), and a quadratic ephemeris model, which assumes a circular orbit with a constant period change rate, given by its derivative over time $\dot{P} = dP/dT$ (equation 4.2). We fit each model to the available times and then use the BIC to determine the best-fit model and parameters.

$$T_{\rm mid} = T_0 + P \times E \tag{4.1}$$

$$T_{\rm mid} = T_0 + P \times E + \frac{1}{2}\dot{P} \times P \times E^2 \tag{4.2}$$

As discussed in Section 1.5, the rate of change is related to the stellar tidal quality factor $Q_\star$. A higher $Q_\star$ indicates a lower tidal dissipation efficiency, meaning a slower rate of orbital decay.

The fitting is performed with an MCMC algorithm, using the same code as the previous transit fits. We define a uniform prior for $\dot{P}$ and Gaussian distributions as priors for $T_{\rm mid}$ and P, using the previously calculated values from Table 4.1 as mean and standard deviation. We define a uniform prior for the $\dot{P}$ with a wide enough interval to allow some freedom in both the positive and negative side, as a potential increase in orbital period cannot be excluded yet.

Table 4.2 presents the results of the orbital decay fits, comparing the BIC values of the linear and quadratic models. The linear model is preferred for both planets: -4.09 against 0.73 for WASP-18b and -3.91 against 0.85 for WASP-19b. This indicates that there is still no statistically significant evidence for a change in the orbital period of these planets. The plots in Figures 4.6 and 4.7 show the best-fit quadratic ephemeris models, where the shaded region corresponds to the 1σ confidence interval. The corresponding posterior distributions are shown in Figure 4.8.

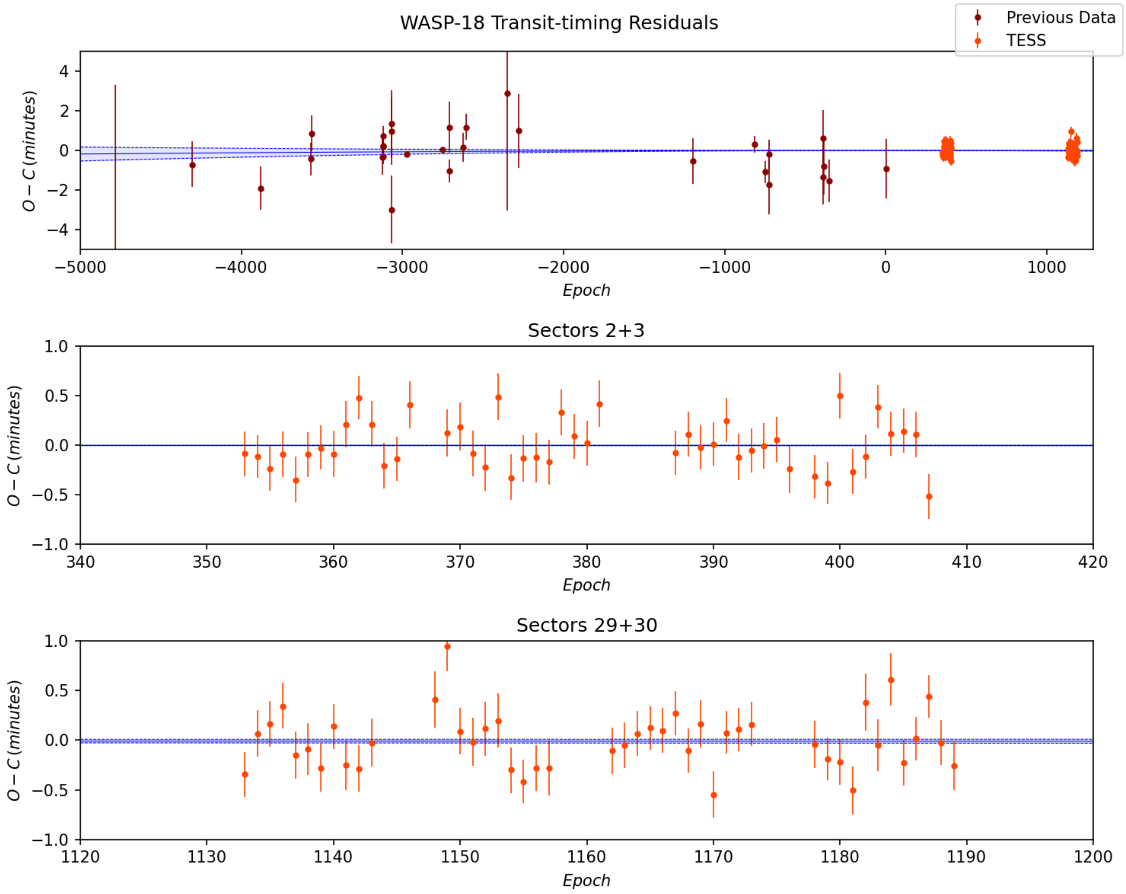

FIGURE 4.6: Transit difference (O-C) against the epoch, counted from the initial reference time for WASP-18b. Previous results from the literature (see Table A.1 for reference) are shown in dark red while our results from TESS are shown in orange. The blue line shows the fitted TTV model with the blue shaded area showing the error margin for $\dot{P}$. Upper plot: complete view of all the transits used in the fit. Middle and lower plot: zoom of the transit timings of TESS, derived in this work. Originally published in Rosário et al. (2022).

TABLE 4.2: Best fit results for the TTV analysis, with the linear ephemeris model and the quadratic model of orbital decay. $Q'_\star$ is given as a lower limit. Uncertainties for time and period given in brackets for the last two digits. Originally published in Rosário et al. (2022).

	WASP-18b		WASP-19b	
Parameter	Linear	Quadratic	Linear	Quadratic
T_0 (BJD)	2458022.125226(16)	2458022.125234(22)	2456021.703698(20)	2456021.703704(21)
P (days)	0.941452407(14)	0.941452400(20)	0.788839004(13)	0.788839038(25)
$\dot{P}$ ($\mathrm{d\,d^{-1}}$)	-	$(-0.11 \pm 0.21) \times 10^{-10}$	-	$(-0.35 \pm 0.22) \times 10^{-10}$
$\dot{P}$ ($\mathrm{ms\,yr^{-1}}$)	-	-0.14 ± 0.27	-	-0.29 ± 0.45
$Q'_\star$ lower limit	-	$> (1.42 \pm 0.34) \times 10^7$	-	$> (1.26 \pm 0.10) \times 10^6$
BIC	-4.03	0.73	-3.91	0.85

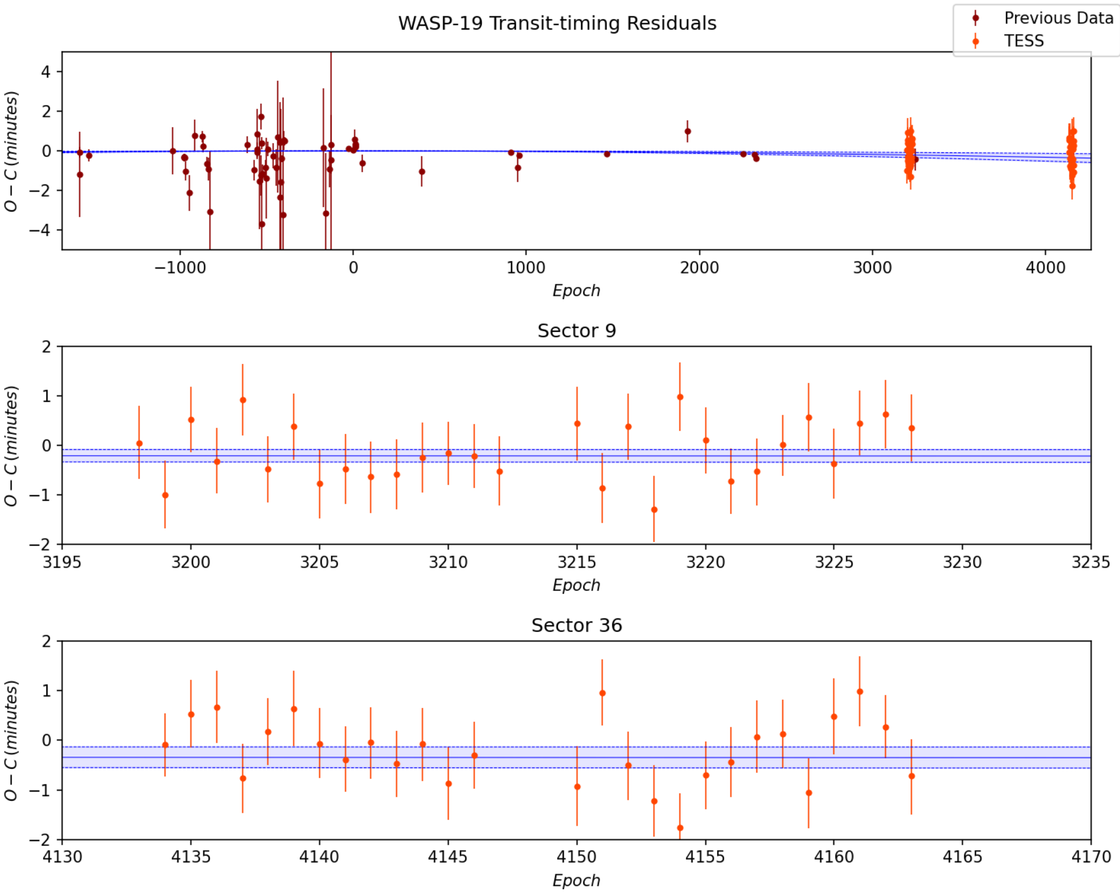

Figure 4.7: Same as Figure 4.6 for WASP-19b. See Table A.2 for the reference of the previous times. Originally published in Rosário et al. (2022).

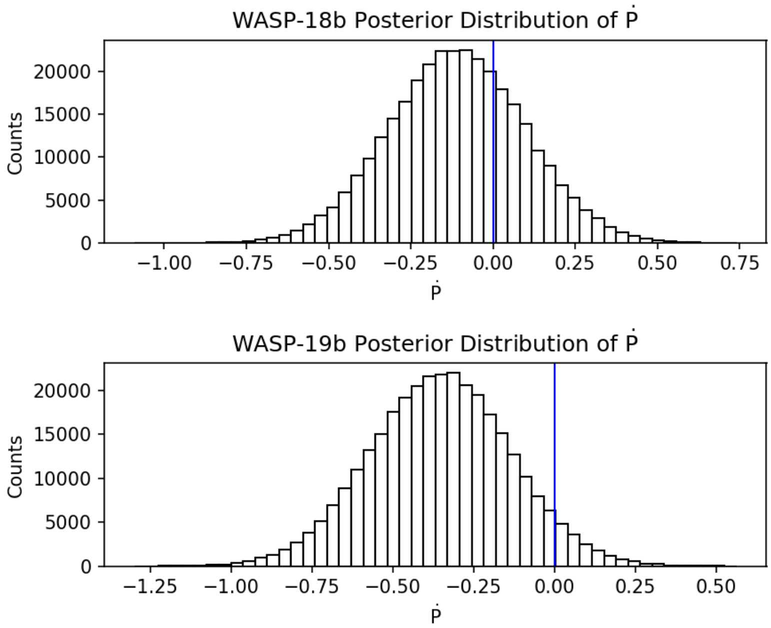

Figure 4.8: Plot of the posterior distribution of $\dot{P}$ from the quadratic ephemerides fit of WASP-18b (upper) and WASP-19b (lower) TTVs. The vertical lines show the location of $\dot{P} = 0$ for reference. Originally published in Rosário et al. (2022).

4.5 Discussion of the TTV analysis

Table 4.3: Comparison of $\dot{P}$ and $Q'_\star$ values from recent works. All upper or lower limits are evaluated at a 95% confidence level (2σ). Originally published in Rosário et al. (2022).

Source	$\dot{P}$	$Q'_\star$
WASP-18b		
Wang et al. (2024)	$(0.23 \pm 0.24) \times 10^{-10}$	-
This work (Rosário et al., 2022)	$(-0.11 \pm 0.21) \times 10^{-10}$	$> (1.42 \pm 0.34) \times 10^{7}$
Maciejewski et al. (2020)	$(0.11 \pm 1.17) \times 10^{-10}$	$> 3.9 \times 10^{6}$
Patra et al. (2020)	$(-1.2 \pm 1.3) \times 10^{-10}$	$> (1.7 \pm 0.4) \times 10^{6}$
Shporer et al. (2019)	$(-0.60 \pm 2.18) \times 10^{-10}$	$> 1.73 \times 10^{6}$
WASP-19b		
Wang et al. (2024)	$(-0.52 \pm 0.09) \times 10^{-10}$	-
Ivshina & Winn (2022)	$(-1.12 \pm 0.37) \times 10^{-10}$	-
This work (Rosário et al., 2022)	$(-0.35 \pm 0.22) \times 10^{-10}$	$> (1.26 \pm 0.10) \times 10^{6}$
Petrucci et al. (2020)	$< -0.73 \times 10^{-10}$	$> (1.23 \pm 0.231) \times 10^{6}$
Patra et al. (2020)	$(-2.06 \pm 0.42) \times 10^{-10}$	$= (5.0 \pm 1.5) \times 10^{5}$

The value of $\dot{P}$ found in our analysis of the WASP-18b TTVs does not allow for a detection of orbital decay being statistically zero at a 1σ confidence level. This is supported by the model comparison test using the BIC, which favours the model with a constant period.

The most recent studies of WASP-18b (Maciejewski et al., 2020; Wang et al., 2024) show values consistent with our findings with no evidence of a decaying period. Initial estimations of the tidal quality parameter reported a minimum value of $Q'_\star > 10^6$ at a confidence level of 95% (Wilkins et al., 2017). The TESS data from the first two sectors improved this constrain, with Shporer et al. (2019), Maciejewski et al. (2020) and Patra et al. (2020) reporting new minimum values in the same order of magnitude (see Table 4.3). We improve this constraint by an order of magnitude with the additional data of TESS sectors 29 and 30, bringing the minimum value to $Q'_\star > (1.42 \pm 0.34) \times 10^7$ within a 2σ confidence level, corresponding to a $\dot{P}$ upper limit of -0.45×10^{-10}. Finally, Wang et al. (2024) recently performed an updated analysis of the decay rate and confirmed our results favouring a constant period model. Our results indicate that for the minimum $Q'_\star$, the spiral in-fall timescale (the time it takes for the planet to fall into the star) is around 5×10^7 yr, which is longer than expected. WASP-12b, the first planet with a detectable period change due to tides, has a $Q'_\star = (1.50 \pm 0.11) \times 10^5$ (Wong et al., 2022), which is two orders of magnitude lower than the minimum value we found for WASP-18b. It orbits an F-type star, with an effective temperature of 6150 K and a mass similar to

WASP-18. If equation 1.12 is correct, and if we assume that in theory $Q'_\star$ should be the same for similar-type stars, then WASP-18b should decay quicker than WASP-12b due to the larger planet-star mass ratio. The absence of detectable orbital decay in WASP-18b indicates that, despite comparable stellar type and mass, $Q'_\star$ is markedly different across the systems, implying that tidal dissipation processes may differ inside similar-type stars.

WASP-19b has a decay rate that is different from zero within the 1σ level, with $\dot{P} = (-0.35 \pm 0.22) \times 10^{-10}$, but not significant at 2σ. As a result, the BIC still favours the constant period model and we are unable to confirm tidal decay in this system with the current data. Our result is significantly different from that of Patra et al. (2020), which were able to detect a period change of $\dot{P} = (-2.06 \pm 0.42) \times 10^{-10}$. As done for WASP-18b, we derive a lower limit for $Q'_\star$ of $(1.26 \pm 0.10) \times 10^6$ at a 95% confidence level, together with an upper limit of $\dot{P} < -0.71 \times 10^{-10}$ (see Table 4.2).

This system has been extensively studied, not only in the search for tidal decay but also due to the high star activity that is present, and the results are not yet conclusive. While Patra et al. (2020) shows indication of a change in period in WASP-19b, Petrucci et al. (2020) discards that hypothesis when including additional transits. We opted to exclude these transits from our analysis and include only the new TESS transits, since we found a substantial scatter and higher normalised residuals in the additional transits near the TESS observations. More recently, while looking for apsidal motion in the system, Bernabo et al. (2024) ruled out tidal decay in the system. The works of Ivshina & Winn (2022) and Wang et al. (2024) also report results for $\dot{P}$ that are consistent with zero and support a constant period model.

The transit depth found in TESS transits, as we briefly discussed, is substantially higher than previously reported by other authors (Hebb et al., 2009b; Tregloan-Reed et al., 2013; Mancini et al., 2013; Espinoza et al., 2019). There are several possible causes for this, one of which being the presence of starspots. Tregloan-Reed et al. (2013) did some research on the subject and found variations in successive light curves caused by spots. However, Wong et al. (2020) could not find evidence of spot-crossing events in individual transits. Espinoza et al. (2019) suggested that rotational variability caused by giant spots could affect the transit depth and the observations. Systematic errors are also a possible cause for differences in the transit shapes, as suggested in Patra et al. (2020) and Petrucci et al. (2020), which further claims that large errors in the transit timing estimation can result from high uncertainty in the orbit's inclination. Consequently, the uncertainty caused by stellar activity warrants caution when confirming or ruling out tidal decay in WASP-19b.

Summary and conclusions

In this work, we analysed TESS transit data to search for tidal decay in two hot Jupiters, WASP-18b and WASP-19b. We performed an initial fit of individual transits to obtain precise mid-transit timings, followed by fitting an orbital decay model including both our timings and those from the literature.

Our analysis found no statistically significant evidence of tidal decay in either system. We updated the minimum values of $Q'_\star$, revealing a two-order-of-magnitude difference between the lower limit for WASP-18 and the value previously reported for WASP-12. This indicates that even within stars of similar spectral types and ages, stellar physics may vary significantly. Better constraining of $Q'_\star$ is crucial to address the reasons behind the different $Q'_\star$ values and give us new information about stellar interiors. Currently, no evidence can be found for tidal decay in these systems and additional transit observations are required to detect or further constrain orbital decay.

Chapter 5

Love number as a proxy for core mass

In the last part of this thesis we investigate the relationship between the second-order Love number for displacement h_2 (see Section 1.5) and the core mass fraction of hot Jupiters. Since h_2 is related to an observable quantity through measurements of tidal deformation, it raises the possibility of using observations to better constrain internal structure models for giant planets. For this, we investigate the theoretical models that can be used to calculate the Love number and their potential in constraining the core mass fraction (CMF) given the observables of radius, mass and Love number.

5.1 Calculation of the Love number

In section 1.5, we saw how transit light curves can be used to measure tidal deformation of a close-in planet, which in turn, can be used to calculate the planet's second-order Love number h_2. The Love number measures the response of a body to a perturbing gravitational potential like the effect of tides, and can be described in terms of displacement (h_2) or potential (k_2). The relationship between the two definitions is easy to calculate and is given by equation 1.16.

Let us consider a perturbing potential V_p. The resulting change in the gravitational potential of a body is then given by

$$\Delta V = k_2 V_p \tag{5.1}$$

where ΔV is the change in potential and V_p is the perturbing potential (e.g. Sterne, 1939; Correia & Rodriguez, 2013).

Following the approach from Sterne (1939) for the definition of the potential, we find that k_2 can be given by the following equation (Buhler et al., 2016):

$$k_2 = \frac{3 - \eta(R)}{2 + \eta(R)} \tag{5.2}$$

where $\eta(R)$ is a function describing the potential perturbation and depends on the radius of the planet R. This function can be calculated by integrating the first-order differential equation below (Sterne, 1939)

$$r\frac{d\eta(r)}{dr} + (\eta(r))^2 - \eta(r) - 6 + \frac{6\rho(r)}{\rho_m(r)}(\eta(r) + 1) = 0 \tag{5.3}$$

where $\rho(r)$ is the density at a given distance r from the centre of the planet and $\rho_m(r)$ is the mean density of a sphere with the same radius.

Combining equations 5.2 and 5.3, we see that for a given R, k_2 only depends on the density profile of the planet, which in turn, is a function of the level of differentiation of the interior and therefore, of the size and mass of the core. In a constant density sphere $\rho = \rho_m$, and therefore, the solution of equation 5.3 leads to $\eta(R) = 0$, which in turn leads a Love number value of $k_2 = 3/2$ ($h_2 = 5/2$ from equation 1.16). As the mean density $\rho_m(r)$ is the same for the same radius and mass, a different distribution in the density profile leads to different $\eta(R)$ functions and different values of k_2, making it the key variable to address the calculation of the Love number.

5.2 Density profiles

The main challenge in this work is therefore the modelling of the density profile, which is particularly difficult in the case of hot Jupiters due to the many unknowns about their interiors. For small planets, Earth-like geological and seismic models provide a strong baseline for exoplanet structure models. In the case of giant planets, particularly hot Jupiters, theoretical models exhibit greater uncertainty and a higher degree of degeneracy due to the presence of an extended gas envelope and lack of direct observational data (Fortney & Nettelmann, 2010; Thorngren et al., 2016). Additional factors such as strong irradiation, atmospheric inflation, and potential mass loss further complicate modelling. We therefore investigate different approaches to model the density profile, from simple analytical models to more complex codes, presenting the challenges faced during the modelling and the results obtained while developing this thesis.

5.2.1 Two-layer analytical model

The simpler way to model the density profile is through the use of the two-layer *toy model* as shown in Helled et al. (2014). This can be represented as an analytical model that reproduces the density profile of Jupiter, modelled using realistic equations of state that match the observable values for average density and gravitational moments. The gravitational moments of giant planets in the Solar System have successfully been measured through Doppler radio tracking of the orbits of spacecrafts like Juno (e.g. Folkner et al., 2017; Durante et al., 2020), in the case of Jupiter. The model consists on a constant density core with a discontinuity in the core-envelope boundary, and assumes a quadratic variation for the envelope density. It can be represented by the following equation

$$\begin{aligned} \rho(r) &= \rho_c \quad r \leq R_c \\ \rho(r) &= \rho_e \left[1 - \left(\frac{r}{R}\right)^2\right] \quad r > R_c \end{aligned} \tag{5.4}$$

where R is the total radius of the planet, R_c is the core radius, ρ_c is the density of the core and ρ_e is the density of the envelope for $r = 0$.

We define the bulk density as the mean density of the planet, given by

$$\rho_{\text{bulk}} = \frac{3M}{4\pi R^3} \tag{5.5}$$

where M is the total mass of the planet, and then define two new dimensionless variables, $x = r/R$ and $\bar{\rho} = \rho/\rho_{\text{bulk}}$.

The envelope density at $r = 0$, ρ_e, is calculated by taking the dimensionless profile and ensuring the mean dimensionless density is equal to one. In other words, integrating the density profile should give the total mass of the planet. Doing this leads us to the following expression:

$$\bar{\rho}_e = \frac{5(1 - \bar{\rho}_c x_c^3)}{2 - 5x_c^3 + 3x_c^5} \tag{5.6}$$

The average density $\rho_m(r)$ is calculated by integrating the density function over the volume between 0 and x.

$$\bar{\rho}_m(x) = \frac{\int_0^{x_c} \bar{\rho}_c \; 4\pi x^2 \; dx + \int_{x_c}^{x} \bar{\rho}_e(1-x^2) \; 4\pi x^2 \; dx}{4/3\pi x^3} \tag{5.7}$$

After solving the integral, we obtain the following expression that can then be replaced in equation 5.3 to calculate $\eta(r)$.

$$\begin{aligned} gher\bar{\rho}_m(x) &= \bar{\rho}_c \quad x \leq x_c \\ \bar{\rho}_m(x) &= \frac{5 + \bar{\rho}_e(5x^3 - 2 - 3x^5)}{5x^3} \quad x > x_c \end{aligned} \tag{5.8}$$

As a test case, we computed the analytical profile based on this simple model for WASP-103b, using the values from Barros et al. (2022b), $R_p = 2.027 \pm 0.145 \; R_{\rm Jup}$ and $M_p = 1.460 \pm 0.089 \; M_{\rm Jup}$. We defined a constant core density of $\rho_c = 15$ g cm^{-3} and varied the mass of the core between 10% and 100% of the planet's total mass, using the latter as a non-physical limit case, and then performed a numerical integration of equation 5.3 to calculate k_2 and h_2, as seen in Appendix B. We will focus on h_2 from now on as it is the more useful quantity to compare with values derived from observations (see section 1.5). Figure 5.1 shows three examples of density profiles calculated by this method, for core mass fractions (CMF) of 10%, 50% and 90%, where the discontinuity between the core and the envelope becomes more pronounced as the CMF increases. As the bulk density of the planet is kept constant (the total radius and mass do not change), a higher CMF leads to a lower envelope density and a thinner envelope, which in turn leads to a smaller value for the Love number.

The resulting relationship between h_2 and the CMF with this model is given in Figure 5.2, where we can see a steady decrease in the Love number as the CMF increases. This behaviour matches the theoretical prediction, where a higher Love number corresponds to a more homogeneous planet and a lower Love number means a high concentration of mass in the centre (e.g. Ragozzine & Wolf, 2009; Kramm et al., 2011).

To validate our model, we calculated the expected CMF for Jupiter and Saturn based on their measured Love numbers, using the previously derived relationship. For Jupiter, using a value of $h_2 = 1.565 \pm 0.006$ (Durante et al., 2020), we obtain CMF=0.061 ± 0.005. The mass of Jupiter's core is thought to be in the range of 7-25 $M_\oplus$ (Wahl et al., 2017; Lozovsky et al., 2017), corresponding to a CMF between 0.02 and 0.08, which aligns well with our result. For Saturn, with $h_2 = 1.39 \pm 0.02$ (Lainey et al., 2017), we derive CMF$=$ 0.226 ± 0.028. Reported core mass estimates for Saturn range from 15 to 18 $M_\oplus$ (Militzer et al., 2019; Mankovich & Fuller, 2021), which correspond to a lower CMF than our estimate (between 0.16 and 0.19). This discrepancy may arise because our model assumes a solid, well-defined core, whereas Saturn's core is known to be diffuse rather than a compact structure (e.g. Mankovich & Fuller, 2021; Fortney et al., 2023). Additionally, since the relationship we used was derived based on WASP-103b, it may not apply exactly to other planets. Therefore, these results should be interpreted with caution.

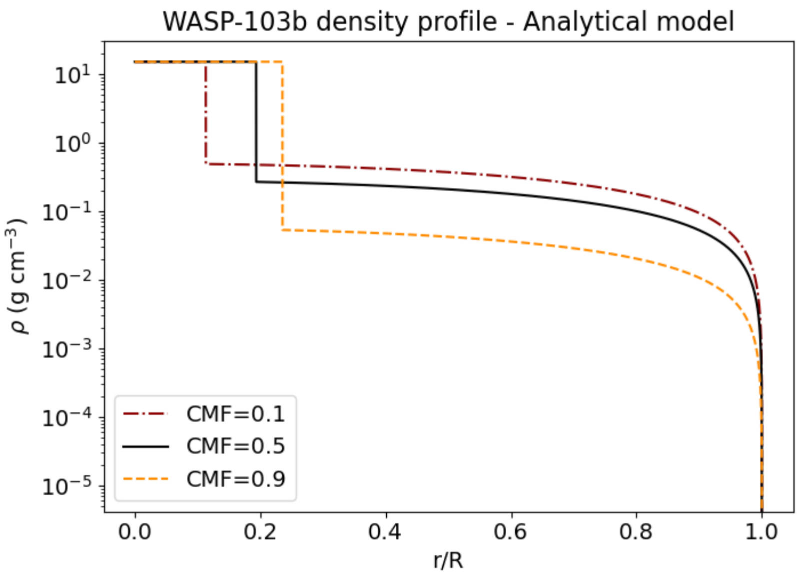

Figure 5.1: Plot of the density profile for WASP-103b with different CMF, using the two-layer analytical model and a constant core density.

WASP-103b was the first planet to have a 3σ detection of tidal deformation through transit photometry (Barros et al., 2022b), reaching a Love number of $h_2 = 1.59^{+0.45}_{-0.53}$. The analysis provided by the authors shows the precision of the Love number measurement is not enough to constrain the core mass fraction and lift the degeneracy in the interior models (Baumeister et al., 2020).

Barros et al. (2024) provides, however, a prediction of the precision that can be obtained with future observations from JWST of WASP-103. Due to the lower signature of the limb darkening in the infrared range, the impact that JWST transits can have in tidal deformation is significant, with the authors reporting an increase in precision to 17σ. With this increase, we used our model to estimate the predicted CMF and were able to constrain it to a value of CMF< 0.12 (see Figure 5.3). The increased precision in the measurement of the Love number offers a key constraint on the internal structure of hot Jupiters and

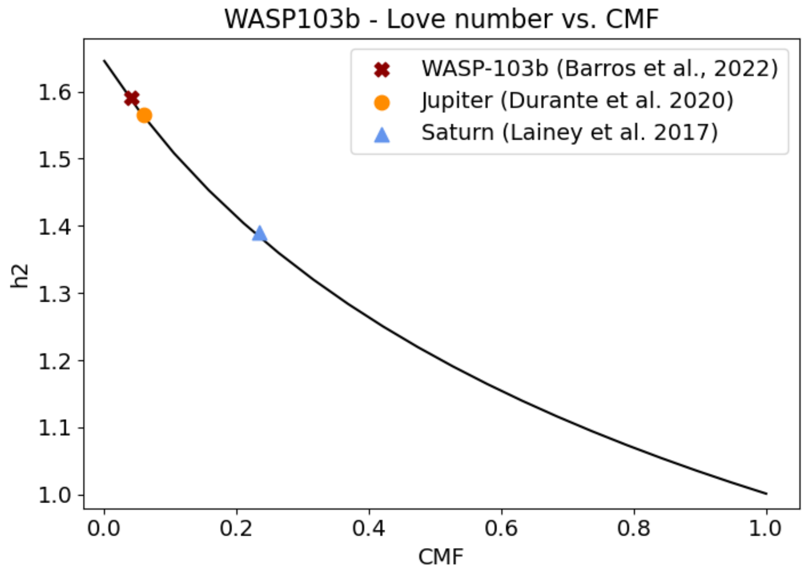

FIGURE 5.2: Plot of the Love number h_2 as a function of the CMF for WASP-103b. We estimated a CMF value for Jupiter and Saturn based on their Love number, using the relationship found by the analytical model for WASP-103b. The individual points show the h_2 and CMF pair for Jupiter (orange circle), Saturn (blue triangle) and WASP-103b (red cross). For clarity, the associated uncertainties are not shown in this plot.

represents an important milestone for future studies. WASP-103 is currently scheduled to be observed by JWST in 2025 and the new observations will potentially pave the way towards the use of the Love number as a way to break the degeneracy in internal structure models. The development of reliable and accurate models is one of the major challenges in exoplanetary science and we can expect significant breakthroughs throughout the next decade.

5.2.2 MESA model

The two-layer model presented before provides a simplified empirical approach to calculate the density profile of the planet based on its core mass and density. However, there are many other factors that can influence a planet's internal structure that are not taken into account, such as the stellar irradiation, the temperature of the planet or the stellar abundances. Furthermore, while the model seems to represent with good accuracy the density profile of Jupiter (Helled et al., 2014), it is not clear the same profile is valid in the same way for every other giant planet, especially ones with different formation and migration histories. Therefore, there is a need for a more complete model of the internal density profile that can be used in a broader range of planets to calculate the Love number and match the incoming observations and detections of tidal deformation.

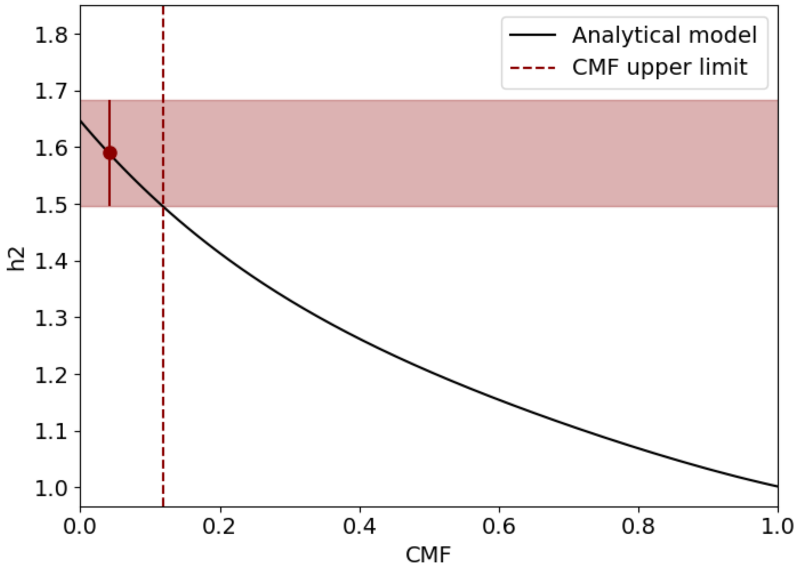

Figure 5.3: Estimated precision of the measurement of the Love number with JWST observations and corresponding CMF upper limit. The shaded area shows the expected error band for the Love number, corresponding to a CMF value between 0 and 0.12 according to our analytical model.

For this, we propose the use of MESA (v12115, Paxton et al., 2018), a stellar evolution code that has been adapted for planet modelling as well (e.g. Batygin & Stevenson, 2013; Storch & Lai, 2014; Buhler et al., 2016; Chen & Rogers, 2016; Kubyshkina et al., 2020; Kubyshkina & Fossati, 2022). MESA is a fairly complex stellar code, and therefore it includes many parameters and many physical processes. The full details on how MESA models giant planets, including the equations of state used and the assumptions made, can be found in Paxton et al. (2013). In short, MESA uses initial values of mass and radius with an adiabatic temperature profile to create the initial model based on the equilibrium equations and the equations of state, which can be user-defined or chosen from the library inside MESA. During the evolution steps, irradiation is calculated as surface heating in the outer mass column with a defined energy generation rate based on flux. Other formulations and user-defined functions are also available and described in the aforementioned paper. MESA further allows the introduction of inert cores that are not evolved in any way and are defined by their mass and radius (or density).

We performed a first attempt with MESA using an adapted version of the script of Kubyshkina et al. (2020), which was originally made for MESA modelling of atmospheric escape in small planets based on the algorithm of Chen & Rogers (2016), but should still be valid for giant planets. We first create the initial model in MESA using a predefined model with 1 $M_{\rm Jup}$ and solar abundances, running for a small number of steps to create the initial conditions. We then adjust the mass of the planet, allowing the atmosphere to accrete (or lose) material until it reaches the target mass, creating a baseline model of the planet. In the following steps, we introduce a solid inert core with a fixed density of $\rho_c = 15$ g cm^{-3} as in the analytical model, evolving the model for another small number of iterations. We vary the mass of the core between 5% and 50% of the planet's total mass, creating individual models for each CMF. The age of the system is then reset, discarding the first steps as burn-in, and the individual models are evolved until the age of the system. A summary of the steps taken during our modelling approach can be seen in the flowchart in Figure 5.4. We then set up the model for the WASP-103b test case using solar abundances of $Z = 0.02$ and $Y = 0.04$ which are used in for both the planet and the star and define the total mass as $M_p = 1.46\ M_{\rm Jup}$, evolving the models for 5 Gyr (Barros et al., 2022b), with stellar irradiation as a source of constant external heat for the entire evolution time.

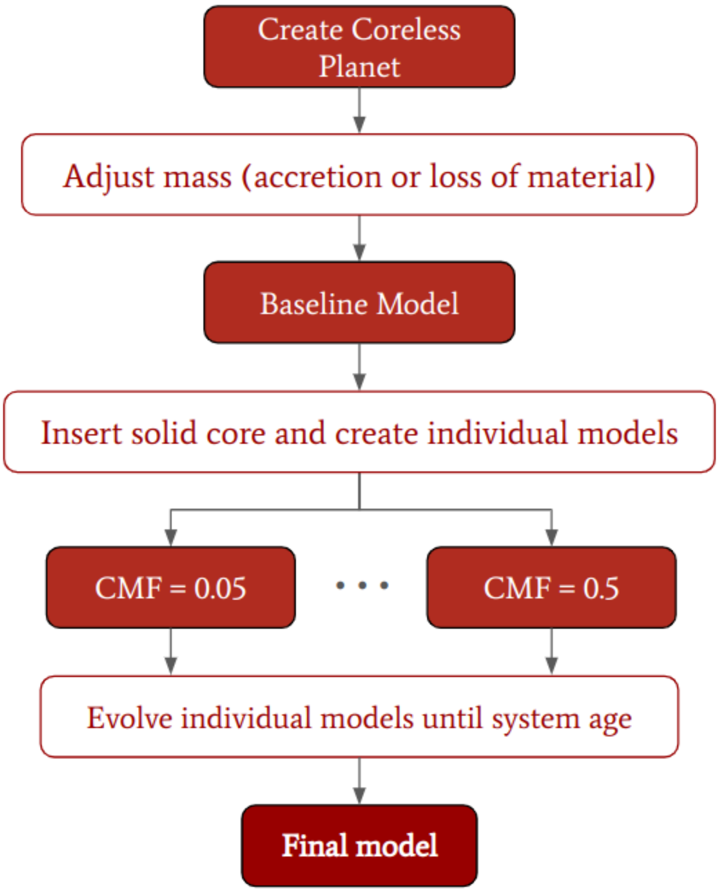

FIGURE 5.4: Flowchart describing the main steps involved in the creation and running of the MESA model. We create the baseline model of a coreless planet and introduce solid cores with a defined mass, building and evolving each individual model until the age of the system.

Preliminary results and discussion

Figure 5.5 shows the density profile obtained from MESA with a CMF of 0.05, plotted with the same profile calculated by the analytical model. The profile shape is consistent within the two models, however, the maximum radius is significantly different, with only 1.13 $R_{\rm Jup}$, 55% of the observed radius of 2.027 $R_{\rm Jup}$ (Barros et al., 2022b). The behaviour is common to all the individual models with different core masses, and the radius obtained with MESA is smaller the higher the CMF, which is to be expected given the lower atmospheric mass fraction. As such, although the final value of the radius varies, none of the models reached the observed radius. This means that the average density is also different, impacting the calculation of the Love number through equation 5.3. In MESA, the radius is not an input as the code calculates the final radius considering the effect of gravity and external heat, solving the equilibrium equations. To confirm there was no mass loss involved, we performed an integration of the profile over the volume and verified the resulting mass matches the input value and the value from observations.

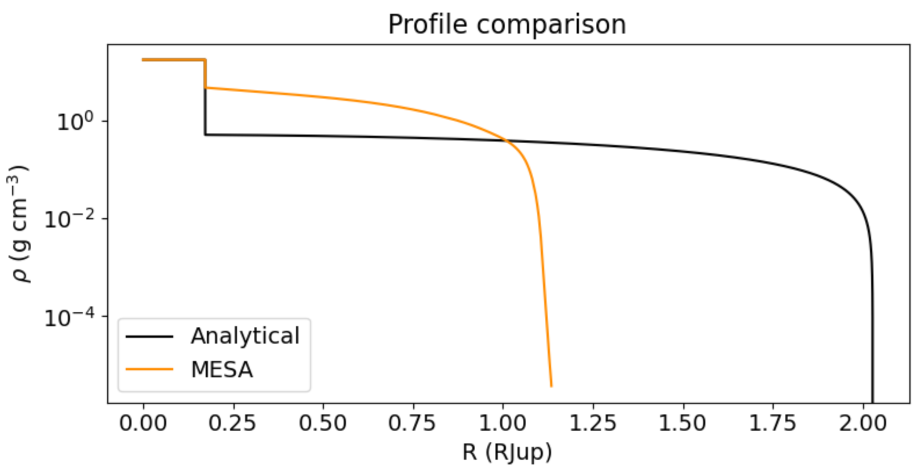

Figure 5.5: Plot of the density profile for WASP-103b with a CMF of 0.05, using the analytical model and the MESA model. We see that the overall shape of the profile is similar, however, the radius of the planet with the MESA model is significantly lower.

The lower radius is likely due to inaccuracies in modeling certain processes related to radius inflation, specifically stellar irradiation, internal heating, or a combination of both. As this work is still in progress, it remains unclear how to properly model these processes in MESA. While stellar irradiation is widely considered a key factor in the radius inflation of hot Jupiters (e.g. Showman & Guillot, 2002; Thorngren & Fortney, 2018; Fortney et al., 2021), modeling the incident flux and selecting the appropriate evolutionary timescale in MESA is not straightforward.

In our current model, we follow the approach of Kubyshkina et al. (2020) and Kubyshkina & Fossati (2022), which estimates the dissipation timescale of the protoplanetary disk and uses the stellar luminosity at that moment to calculate the incident flux. However, different luminosity values result in different irradiation fluxes, potentially affecting the final results. The luminosity computed by our script differs significantly from the reported value, yielding 0.97 $L_{\odot}$, compared to 3.47 ± 0.49 $L_{\odot}$ reported in Barros et al. (2022b). The reason for this discrepancy is unclear and requires further investigation, particularly because the higher luminosity caused convergence issues in MESA, preventing the model from running.

It has been shown before that the observed radius of irradiated hot Jupiters is higher than predicted by evolution models (Bodenheimer et al., 2001; Guillot & Showman, 2002; Fortney et al., 2021). Figure 5.6 presents a plot from Fortney et al. (2021) showing the distribution of observed radii of hot Jupiters by incident flux, coloured by planet mass. The red line represents a model without additional inflation effects, and clearly shows a tendency for the model to underestimate the observed radius. We estimated the incident flux for WASP-103b with $f = L_{\text{bol}}/4\pi d^2$, using the following values from Barros et al. (2022b): $L_{\text{bol}} = 3.47\ L_{\odot}$, $d = 3.0038\ R_{\star}$ and $R_{\star} = 1.716\ R_{\odot}$, reaching an incident flux of $f = 8.22 \times 10^9$ erg s^{-1} cm^{-2}. With this value, the plot in Figure 5.6 estimates a radius of only 1.25 R_{Jup}, which significantly underestimates the observed radius of WASP-103b. This predicted radius is slightly larger than the one obtained in our MESA model, potentially due to the difference in luminosity. However, we can conclude that simply using the reported luminosity in MESA is insufficient to reproduce the observed radius without additional contributions.

While the exact reasons are still unknown, heat transfer physical processes such as turbulent mixing (e.g. Youdin & Mitchell, 2010), hydrodynamical dissipation (e.g. Guillot & Showman, 2002) and vertical advection of temperature caused by deep atmospheric circulation (e.g. Tremblin et al., 2017; Sainsbury-Martinez et al., 2019) have been theorised as a cause for the radius discrepancy. The main challenge is modeling these processes in MESA to produce a radius closer to the observed value. Chen & Rogers (2016) and later Kubyshkina & Fossati (2022) introduce an additional step consisting on an artificial luminosity to inflate the planet while setting an standardized initial entropy. As a first approach, we chose to set up the model without this step to assess the need to include it. Since we do not yet fully understand how these steps work within MESA, we were unable

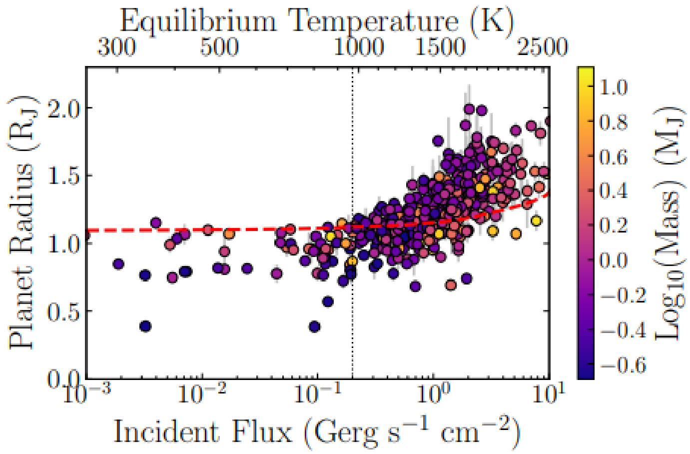

Figure 5.6: Plot of the observed radius as a function of incident flux for several known giant planets, coloured by planetary mass. The red dashed line shows the radius prediction from an evolutionary model for Jupiter-like planets. Figure originally published in Fortney et al. (2021).

to investigate them in detail within the given time constraints to finish this thesis, and more work is required.

Given the issues discussed in the previous paragraphs, we find the Love number from MESA does not follow the same behaviour as predicted by the analytical model (see Figure 5.7). Despite the similar values obtained for small cores (5%), our current MESA models predict an opposite evolution of the Love number with the CMF when compared to the analytical model. Therefore, at the time of writing this thesis, the correct modelling of the radius appears to be the key for a full assessment of the potential of MESA as a forward model for obtaining the density profile.

In summary, the analytical model shows a relationship between h_2 and the CMF that matches the expected results from the theory and provides an consistent value for the CMF of Jupiter, showing a slight deviation in the case of Saturn. While the model is simple, it is based on extensive studies from Jupiter's interior and therefore provides a strong baseline to estimate the CMF based on observed Love numbers. The model from MESA is currently unable to reproduce the observed radius of our test-case planet (WASP-103b) and therefore shows an inconsistent behaviour and we are unable to conclude on the variation of the Love number with parameters such as irradiation and core size. Since MESA has been successfully used before to obtain the Love number and the CMF (e.g. Buhler et al., 2016), further developments are needed to improve our implementation.

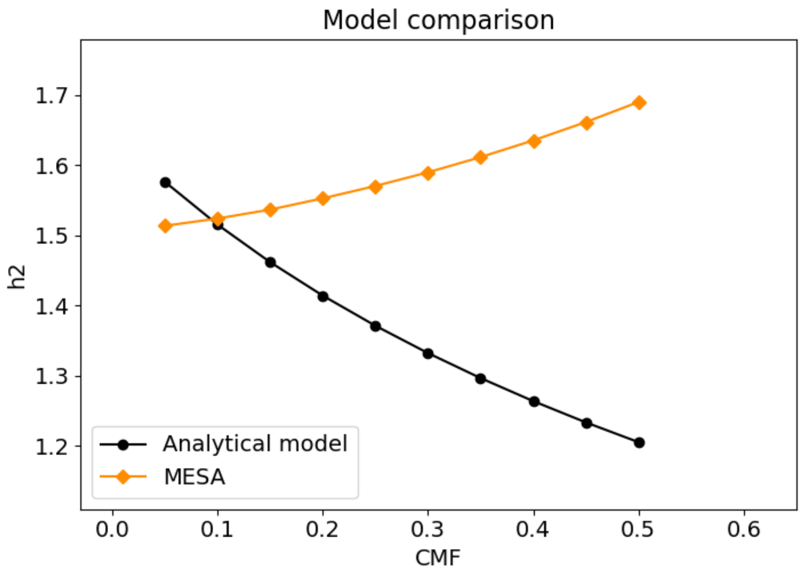

FIGURE 5.7: Comparison of the Love number h_2 obtained for WASP-103b with the MESA model and the analytical model.

Chapter 6

Conclusions and future work

The characterisation of exoplanets is a fundamental aspect in current planetary science. In this work we explored two main approaches for the characterisation of the main parameters of planets and their orbits, applying state-of-the-art methods to new data that allowed for a refinement of those parameters. However, most of this work only scratches the surface of what can be achieved in the future as both technology and knowledge improve. Each one of the works developed during this thesis has potential for future improvements with new data and new models.

In Chapter 3, we presented the joint analysis of the transit and RV data for the two-planet system HD 15337. This system offers valuable insight into the radius valley, with two planets lying on either side of it. Our analysis obtained refined radius and mass, making HD 15337 b one of the most precisely characterised super-Earths to date.

In this work we tackled several challenges in the treatment of both transit and RV data. We detrended and decorrelated the transit data from TESS and CHEOPS, minimising the effect of stellar activity and of both short- and long-term trends. We further applied a GP regression to the RV time series using the R'_{HK} indicator as a proxy for the activity model, successfully removing the short-term effects caused by stellar activity. We addressed an unknown long-term trend in the RV time series which can a priori be caused by an external companion. While no definitive conclusion could be reached, it is still unlikely from our findings that the trend has an external cause, and the most likely scenario is still an activity-induced trend.

Our analysis, based on data from TESS, CHEOPS and HARPS, achieved a radius precision of 1.7% and a mass precision of 6.2%, leading to a precision of only 8.2% in density calculation. The improvement in the estimation of the planet density proves to be crucial in reducing the degeneracy of current internal structure models, which are unable to distinguish the size of each layer and its components when the data is lacking or the error bars are too high. Our internal structure analysis gives a water mass fraction of $0.10^{+0.10}_{-0.08}$, with error bars corresponding to the 5th and 95th percentiles, which is compatible with zero at a 3σ level and therefore is not enough to claim the presence of water in this planet. The second planet, a puffy sub-Neptune, also saw big improvements in the radius precision, reaching a value around 3%, but the same can not be said about the mass error bars which are still in the same order magnitude as previous works. Despite this, we obtained a density of $2.30^{+0.50}_{-0.41}$ g cm^{-3}, consistent with the notion that this planet hosts a gas envelope. This is further validated by our internal structure analysis that shows a significant H/He envelope with a mass around 0.03 $M_{\oplus}$.

While we have pushed the precision of mass and radius measurements to the limits of current instrumentation, internal structure models remain highly degenerate, making it difficult to accurately characterise planetary interiors. The need for additional data to introduce new constraints is evident. Ongoing efforts to characterize planetary atmospheres through spectroscopy could provide insights into elemental abundances, which in turn may help constrain the composition of deeper layers and reduce degeneracy in interior models.

The HD 15337 system hosts two small planets with well-constrained mass and radius, lying on opposite sides of the radius valley, making them valuable test cases for understanding its formation. As a result, this system offers an excellent laboratory for upcoming research on atmospheric evaporation, which could further reveal its role in shaping the radius valley. It has been shown by Dumusque et al. (2019) that HD 15337b could not have kept the atmosphere so close to its star, which suggests that mechanism is responsible for the difference in composition in the two planets. Improved atmospheric models can also help constrain the internal structure, as the current models show a high degeneracy that can not be broken with mass and radius alone, as discussed in section 3.7. While assuming stellar abundances for the planet atmosphere can provide a preliminary constrain, the relationship between the abundances of star and planet is uncertain, with studies showing it does not follow a simple 1:1 relationship (Adibekyan et al., 2021).

Future missions such as PLATO (Rauer et al., 2024) will significantly improve the characterisation of small exoplanets like those in the HD 15337 system. PLATO aims to provide high-precision photometry and improved stellar age estimates, reducing uncertainties in planetary parameters and offering deeper insights into the formation and evolution of planets within the radius valley. Combined with upcoming spectroscopic data from JWST and ARIEL, PLATO's precise radius and age measurements will refine models of planetary formation and evolution, particularly for low-mass planets. The synergy between PLATO, ground-based spectroscopic surveys, and advanced retrieval models will be key to breaking current degeneracies in planetary interior and atmospheric characterisation.

In the second part of our work, we addressed the characterisation of giant planets. Since the models for internal structure of gas giants are not as developed and require different physics, planet-star interaction is one of the best approaches to obtain clues about these planets' composition and interior. We investigated the impact of tidal forces on the orbits of two hot Jupiters, WASP-18b and WASP-19b, in at attempt to find statistically significant signs of orbital decay caused by tides. Tidal decay can be used to constrain stellar physics related to tidal dissipation, which can also provide advancements in researching tidal deformation.

We provide updated values for the stellar tidal parameter Q'_*. Although we did not detect tidal decay in WASP-18 or WASP-19, additional data improved the constraints on Q'_*, indicating that orbital decay in these systems is occurring more slowly than initially predicted by theoretical models. As these models are based on the interaction between binary stars, it shows that planet-star interactions differ significantly. We also compare our results with other systems with close-in hot Jupiters and find that stars of the same type can have different orders of magnitude in Q'_*. For example, the current constrains for WASP-18b are significantly different than the measured Q'_* for WASP-12b, with our result setting a minimum value of $(1.42 \pm 0.34) \times 10^7$, two orders of magnitude higher than the $(1.70 \pm 0.14) \times 10^5$ reported for WASP-12b by Akinsanmi et al. (2024).

CHEOPS has been following both WASP-18 and WASP-19, obtaining new transits and light curves. When searching for tidal decay, the larger the timespan of the observations, the better the prospects of a detection, especially with a high number of observed transits. As newer data becomes available, putting together the transit timings derived in this thesis with the new transits will add new constrains to $Q'_\star$ and increase the probability of a detection.

In the final part of this work, we studied the correlation between the second-order Love number and the core mass fraction of hot Jupiters and how recent measurements can help constrain the interior of these planets. We applied a simple analytical model to obtain the density profile of WASP-103b and estimate its CMF based on the observed values.

During our work we also attempted to use a more complete code (MESA) to model the density profile but the code proved more challenging than anticipated and therefore this investigation is still a work in progress.

Future developments

The analytical model we used is a very simplified approach that can work as a proof of concept, but more detailed models are necessary to obtain an accurate relationship between the internal structure and the Love number. The main potential of this work in the future is the development of a two-part model that can infer the core mass of the planet based on observations. The first part, the forward model, can be achieved by an analytical model like the one used in this thesis, or a more complete code like MESA. The forward model provides the density profile of a planet given the observables like radius, mass and stellar abundances. The second part, the retrieval layer, is implemented on top of the forward model and has several possible approaches, with the use of an MCMC algorithm or the use of machine learning algorithms to train the model with the values obtained from the observed tidal deformation of existing exoplanets. The retrieval layer will then output the posterior probability distributions of key parameters, such as the core mass, given h_2. This process is summarised in Figure 6.1.

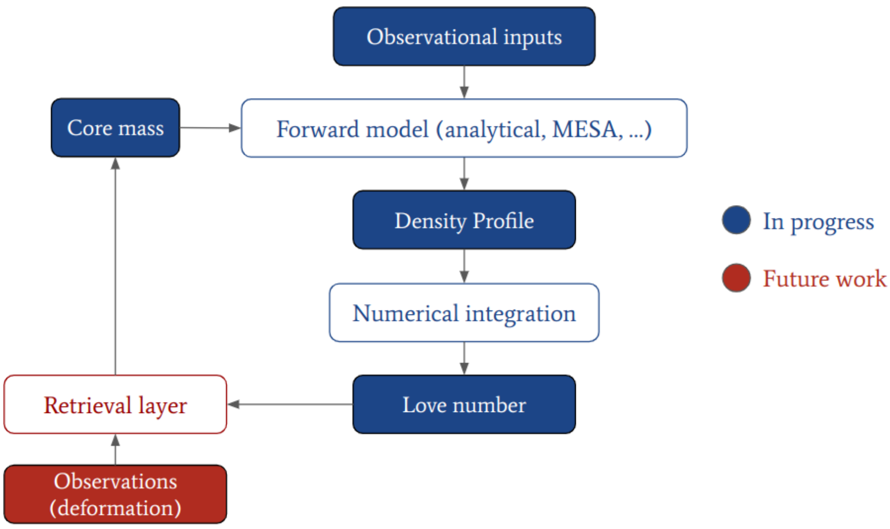

FIGURE 6.1: Schematics showing the process to build the retrieval model.

One of the major challenges at the moment of writing this thesis is the building of the forward model. As mentioned in section 5.2.2, some parts of the modelling are not yet defined, namely the core luminosity and radius inflation mechanisms. Studying the effect of the different variables in the MESA code and attempting to correctly reproduce the observed radius is key to be able to build a robust model that can be used as the base for the retrieval model in the future. Alternative codes and models can also be investigated and compared to the current results. During the development of this work, we considered an adaptation of the models of Zeng et al. (2016) and Padovan et al. (2018) for hot Jupiters to build our forward model, but as the codes are not publicly available we opted for MESA. There is, however, potential to build upon these existing codes in the future and create a robust model to include the Love number measurements and constrain the core and the envelope of both hot Jupiters and rocky planets.

Appendix A

Additional tables

TABLE A.1: WASP-18b transit times with epochs calculated from reference time T_0 = 2458022.1249563. Values marked with * were derived by Maciejewski et al. (2020) using the source light curve.

Epoch	T_{mid} (BJD)	Residuals		Band-pass	Light Curve Reference
−10150	2448466.365700*	+0.0328*	−0.0209*	I	Hipparcos, ESA (1997)
−4784	2453518.21258*	+0.00842*	−0.00666*	I	Pojmanski (1997)
−4304	2453970.113611*	+0.000782*	−0.000815*	0.4 − 0.7 μm	Butters et al. (2010)
−3881	2454368.347146*	+0.000748*	−0.00077*	0.4 − 0.7 μm	Butters et al. (2010)
−3566	2454664.905676*	+0.000582*	−0.000576*	0.4 − 0.7 μm	Hellier et al. (2009)
−3565	2454665.84803*	+0.000629*	−0.00064*	0.4 − 0.7 μm	Hellier et al. (2009)
−3122	2455082.910597*	+0.000598*	−0.000634*	V	Southworth et al. (2009)
−3121	2455083.852439*	+0.000315*	−0.000302*	V	Southworth et al. (2009)
−3120	2455084.793919*	+0.000243*	−0.000244*	V	Southworth et al. (2009)
−3119	2455085.734997*	+0.000267*	−0.000263*	V	Southworth et al. (2009)
−3118	2455086.677153*	+0.000344*	−0.00035*	V	Southworth et al. (2009)
−3068	2455133.7472*	+0.001181	−0.001181	I	Cortés-Zuleta et al. (2020)
−3067	2455134.6914*	+0.001181	−0.001181	I	Cortés-Zuleta et al. (2020)
−3066	2455135.6331*	+0.001181	−0.001181	I	Cortés-Zuleta et al. (2020)
−2975	2455221.3042	+0.0001	−0.0001	3.6 μm	Maxted et al. (2013)
−2751	2455432.1897	+0.0001	−0.0001	4.5 μm	Maxted et al. (2013)
−2710	2455470.7885	+0.0004	−0.0004	I+z	Maxted et al. (2013)
−2707	2455473.6144	+0.0009	−0.0009	I+z	Maxted et al. (2013)
−2621	2455554.5786	+0.0005	−0.0005	I+z	Maxted et al. (2013)
−2604	2455570.584	+0.00045	−0.00048	I+z	Maxted et al. (2013)
−2348	2455811.597*	+0.004097	−0.004097	I	Cortés-Zuleta et al. (2020)
−2279	2455876.5559	+0.0013	−0.0013	z’	Maxted et al. (2013)

Continues on the next page

* Value derived by Maciejewski et al. (2020)

Table A.1 – continued

Epoch	T_{mid} (BJD)	Residuals		Band-pass	Light Curve Reference
−1196	2456896.1478	+0.0008	−0.0008	1.1 − 1.7 μm	Wilkins et al. (2017)
−814	2457255.7832	+0.0003	−0.00029	z	Wilkins et al. (2017)
−746	2457319.801	+0.00039	−0.00038	z	Wilkins et al. (2017)
−726	2457338.6296*	+0.00106*	−0.00108*	r'	Kedziora-Chudczer et al. (2019)
−725	2457339.572103*	+0.000516*	−0.000506*	r'	Kedziora-Chudczer et al. (2019)
−388	2457656.84078	+0.000972	−0.000972	I	Cortés-Zuleta et al. (2020)
−387	2457657.78359	+0.000972	−0.000972	I	Cortés-Zuleta et al. (2020)
−386	2457658.72404	+0.000972	−0.000972	I	Cortés-Zuleta et al. (2020)
−353	2457689.79147*	+0.00075	−0.00075	z'	Patra et al. (2020)
5	2458026.83186*	+0.001042	−0.001042	R	Cortés-Zuleta et al. (2020)
353	2458354.45787421	+0.0001575586	−0.0001564676	0.6 − 1.0 μm	TESS S2
354	2458355.39930413	+0.0001488504	−0.0001511559	0.6 − 1.0 μm	TESS S2
355	2458356.34067383	+0.0001539404	−0.0001580069	0.6 − 1.0 μm	TESS S2
356	2458357.28222453	+0.0001567581	−0.0001626202	0.6 − 1.0 μm	TESS S2
357	2458358.22349873	+0.0001580067	−0.0001633241	0.6 − 1.0 μm	TESS S2
358	2458359.16513058	+0.0001620091	−0.0001548205	0.6 − 1.0 μm	TESS S2
359	2458360.10662774	+0.0001524249	−0.0001600427	0.6 − 1.0 μm	TESS S2
360	2458361.04803607	+0.0001606493	−0.0001632962	0.6 − 1.0 μm	TESS S2
361	2458361.98969784	+0.000163606	−0.000161472	0.6 − 1.0 μm	TESS S2
362	2458362.93133366	+0.0001485966	−0.0001554287	0.6 − 1.0 μm	TESS S2
363	2458363.87260354	+0.0001581918	−0.0001603849	0.6 − 1.0 μm	TESS S2
364	2458364.81376481	+0.0001590161	−0.0001616745	0.6 − 1.0 μm	TESS S2
365	2458365.75526545	+0.0001551888	−0.0001560597	0.6 − 1.0 μm	TESS S2
366	2458366.69709569	+0.0001624828	−0.0001675395	0.6 − 1.0 μm	TESS S2
369	2458369.52125913	+0.0001696489	−0.000165043	0.6 − 1.0 μm	TESS S2
370	2458370.46275328	+0.0001658185	−0.0001689851	0.6 − 1.0 μm	TESS S2
371	2458371.40401605	+0.0001579167	−0.0001617904	0.6 − 1.0 μm	TESS S2
372	2458372.34537126	+0.0001652232	−0.0001639084	0.6 − 1.0 μm	TESS S2
373	2458373.28731853	+0.0001626426	−0.0001615565	0.6 − 1.0 μm	TESS S2
374	2458374.22820482	+0.0001543535	−0.0001656061	0.6 − 1.0 μm	TESS S2
375	2458375.16979404	+0.0001626522	−0.0001585855	0.6 − 1.0 μm	TESS S2
376	2458376.11125522	+0.0001772189	−0.0001689486	0.6 − 1.0 μm	TESS S2
377	2458377.05267219	+0.0001583615	−0.0001536757	0.6 − 1.0 μm	TESS S2
378	2458377.99447371	+0.000163249	−0.00015706	0.6 − 1.0 μm	TESS S2
379	2458378.93575739	+0.0001563332	−0.0001569462	0.6 − 1.0 μm	TESS S2
380	2458379.87716368	+0.0001624613	−0.0001570392	0.6 − 1.0 μm	TESS S2
381	2458380.8188868	+0.0001584449	−0.0001654274	0.6 − 1.0 μm	TESS S2

Continues on the next page

* Value derived by Maciejewski et al. (2020)

Table A.1 – continued

Epoch	T_{mid} (BJD)	Residuals		Band-pass	Light Curve Reference
387	2458386.46725968	+0.0001516065	−0.0001555054	0.6 − 1.0 μm	TESS S3
388	2458387.40884281	+0.0001566545	−0.0001593569	0.6 − 1.0 μm	TESS S3
389	2458388.35020331	+0.0001558977	−0.000153218	0.6 − 1.0 μm	TESS S3
390	2458389.29167884	+0.0001504402	−0.0001515723	0.6 − 1.0 μm	TESS S3
391	2458390.23329699	+0.000153637	−0.0001603253	0.6 − 1.0 μm	TESS S3
392	2458391.17449162	+0.0001584431	−0.0001643114	0.6 − 1.0 μm	TESS S3
393	2458392.11599167	+0.0001552277	−0.0001539209	0.6 − 1.0 μm	TESS S3
394	2458393.05747866	+0.0001625986	−0.0001583644	0.6 − 1.0 μm	TESS S3
395	2458393.99897112	+0.0001548479	−0.0001582581	0.6 − 1.0 μm	TESS S3
396	2458394.94021869	+0.0001668753	−0.000169203	0.6 − 1.0 μm	TESS S3
398	2458396.82307126	+0.0001512507	−0.0001505658	0.6 − 1.0 μm	TESS S3
399	2458397.76447778	+0.000146889	−0.0001459783	0.6 − 1.0 μm	TESS S3
400	2458398.70654418	+0.0001594393	−0.0001563517	0.6 − 1.0 μm	TESS S3
401	2458399.64746347	+0.0001560997	−0.0001559248	0.6 − 1.0 μm	TESS S3
402	2458400.58901982	+0.0001530252	−0.0001545594	0.6 − 1.0 μm	TESS S3
403	2458401.53082095	+0.0001507412	−0.0001534252	0.6 − 1.0 μm	TESS S3
404	2458402.47208663	+0.0001577229	−0.0001532313	0.6 − 1.0 μm	TESS S3
405	2458403.41355656	+0.0001517973	−0.0001556871	0.6 − 1.0 μm	TESS S3
406	2458404.35498739	+0.0001610387	−0.0001595482	0.6 − 1.0 μm	TESS S3
407	2458405.29600312	+0.0001597197	−0.0001557732	0.6 − 1.0 μm	TESS S3
1133	2459088.79056522	+0.0001600377	−0.000157913	0.6 − 1.0 μm	TESS S29
1134	2459089.73230357	+0.00016285	−0.0001653548	0.6 − 1.0 μm	TESS S29
1135	2459090.67382584	+0.0001615088	−0.000156747	0.6 − 1.0 μm	TESS S29
1136	2459091.61540082	+0.0001579316	−0.0001647125	0.6 − 1.0 μm	TESS S29
1137	2459092.55650709	+0.000163614	−0.0001653631	0.6 − 1.0 μm	TESS S29
1138	2459093.49800326	+0.0001791626	−0.000182826	0.6 − 1.0 μm	TESS S29
1139	2459094.43932496	+0.00016946	−0.0001692725	0.6 − 1.0 μm	TESS S29
1140	2459095.38106862	+0.0001587269	−0.0001569717	0.6 − 1.0 μm	TESS S29
1141	2459096.322251	+0.0001754	−0.0001693464	0.6 − 1.0 μm	TESS S29
1142	2459097.26367608	+0.0001623146	−0.000163599	0.6 − 1.0 μm	TESS S29
1143	2459098.20530848	+0.0001658825	−0.0001709083	0.6 − 1.0 μm	TESS S29
1148	2459102.91287775	+0.0001981444	−0.0001957247	0.6 − 1.0 μm	TESS S29
1149	2459103.85470132	+0.0001778397	−0.0001803071	0.6 − 1.0 μm	TESS S29
1150	2459104.79555654	+0.0001625176	−0.0001631086	0.6 − 1.0 μm	TESS S29
1151	2459105.73693338	+0.0001674303	−0.0001728937	0.6 − 1.0 μm	TESS S29
1152	2459106.67848308	+0.0001915787	−0.0001836274	0.6 − 1.0 μm	TESS S29
1153	2459107.61998804	+0.0001852554	−0.0001908498	0.6 − 1.0 μm	TESS S29

Continues on the next page

* Value derived by Maciejewski et al. (2020)

Table A.1 – continued

Epoch	T_{mid} (BJD)	Residuals		Band-pass	Light Curve Reference
1154	2459108.56109682	+0.0001617988	−0.0001577111	0.6 − 1.0 μm	TESS S29
1155	2459109.50246742	+0.0001534618	−0.0001552651	0.6 − 1.0 μm	TESS S29
1156	2459110.44401564	+0.0001615148	−0.0001572489	0.6 − 1.0 μm	TESS S29
1157	2459111.38546737	+0.0001939066	−0.0001912813	0.6 − 1.0 μm	TESS S29
1162	2459116.09285056	+0.0001631719	−0.0001617505	0.6 − 1.0 μm	TESS S30
1163	2459117.03434091	+0.000159676	−0.0001590436	0.6 − 1.0 μm	TESS S30
1164	2459117.97587372	+0.0001570867	−0.0001617813	0.6 − 1.0 μm	TESS S30
1165	2459118.91736845	+0.0001536699	−0.0001490039	0.6 − 1.0 μm	TESS S30
1166	2459119.85879866	+0.0001564968	−0.0001585761	0.6 − 1.0 μm	TESS S30
1167	2459120.80037428	+0.0001553485	−0.0001542201	0.6 − 1.0 μm	TESS S30
1168	2459121.74156424	+0.0001554497	−0.0001566477	0.6 − 1.0 μm	TESS S30
1169	2459122.68320566	+0.0001682892	−0.0001619783	0.6 − 1.0 μm	TESS S30
1170	2459123.62416204	+0.0001632229	−0.0001626586	0.6 − 1.0 μm	TESS S30
1171	2459124.56604724	+0.0001482321	−0.0001548794	0.6 − 1.0 μm	TESS S30
1172	2459125.50752307	+0.0001542799	−0.0001514558	0.6 − 1.0 μm	TESS S30
1173	2459126.44901138	+0.0001535523	−0.0001585222	0.6 − 1.0 μm	TESS S30
1178	2459131.15613401	+0.0001649443	−0.000162974	0.6 − 1.0 μm	TESS S30
1179	2459132.09748432	+0.000152724	−0.0001505922	0.6 − 1.0 μm	TESS S30
1180	2459133.03891429	+0.000160387	−0.0001600435	0.6 − 1.0 μm	TESS S30
1181	2459133.98016695	+0.0001660438	−0.0001685588	0.6 − 1.0 μm	TESS S30
1182	2459134.92223374	+0.0001939714	−0.000202803	0.6 − 1.0 μm	TESS S30
1183	2459135.86338806	+0.000181922	−0.000183373	0.6 − 1.0 μm	TESS S30
1184	2459136.80530221	+0.0001828732	−0.0001829882	0.6 − 1.0 μm	TESS S30
1185	2459137.74616908	+0.0001570621	−0.000162082	0.6 − 1.0 μm	TESS S30
1186	2459138.6877949	+0.0001539593	−0.0001510713	0.6 − 1.0 μm	TESS S30
1187	2459139.62954128	+0.0001504001	−0.000146267	0.6 − 1.0 μm	TESS S30
1188	2459140.57066808	+0.0001572311	−0.000159404	0.6 − 1.0 μm	TESS S30
1189	2459141.51195794	+0.0001686196	−0.0001678828	0.6 − 1.0 μm	TESS S30

TABLE A.2: WASP-19b transit times with epochs calculated from reference time T_0 = 2456021.70389628.

Epoch	T_{mid} (BJD)	Residuals		Bandpass	Light Curve Reference
−1580	2454775.3372	+0.0015	−0.0015	z	Hebb et al. (2009b)
−1578	2454776.91566	+0.00019	−0.00019	H	Anderson et al. (2010)
−1527	2454817.14633	+0.00021	−0.00021	H	Lendl et al. (2013)
−1042	2455199.73343	+0.00083	−0.00083	Clear	Tifner F. (TRESCA)
−976	2455251.79657	+0.00014	−0.00014	r-Gunn	Tregloan-Reed et al. (2013)

Continues on the next page

Table A.2 – continued

Epoch	$T_{\rm mid}$ (BJD)	Residuals		Bandpass	Light Curve Reference
−975	2455252.58544	+0.0001	−0.0001	*r-Gunn*	Tregloan-Reed et al. (2013)
−971	2455255.74077	+0.00012	−0.00012	*r-Gunn*	Tregloan-Reed et al. (2013)
−966	2455259.68448	+0.00033	−0.00033	Clear	Coloque J. (TRESCA)
−948	2455273.88282	+0.00062	−0.00062	Clear	Evans P. (TRESCA)
−916	2455299.12768	+0.00055	−0.00055	Clear	Curtis I. (TRESCA)
−871	2455334.6254	+0.00021	−0.00021	*R*	Mancini et al. (2013)
−866	2455338.56927	+0.00023	−0.00023	*I+z'*	Lendl et al. (2013)
−847	2455353.55659	+0.00024	−0.00024	*R*	Mancini et al. (2013)
−834	2455363.81131	+0.00041	−0.00041	*BB*	Milne G. (TRESCA)
−828	2455368.54285	+0.00212	−0.00212	*R*	Mancini et al. (2013)
−611	2455539.72327	+0.0003	−0.0003	*I-Cousins*	Lendl et al. (2013)
−573	2455569.69826	+0.00036	−0.00036	*I+z'*	Lendl et al. (2013)
−556	2455583.10979	+0.00089	−0.00089	Clear	Curtis I. (TRESCA)
−554	2455584.68693	+0.00024	−0.00024	*r'*	Lendl et al. (2013)
−554	2455584.68684	+0.00019	−0.00019	*I+z'*	Lendl et al. (2013)
−542	2455594.15188	+0.00168	−0.00168	*R*	Mancini et al. (2013)
−533	2455601.25164	+0.00071	−0.00071	*R*	Mancini et al. (2013)
−531	2455602.83138	+0.00046	−0.00046	*I+z'*	Lendl et al. (2013)
−528	2455605.19414	+0.0018	−0.0018	*R*	Mancini et al. (2013)
−526	2455606.77464	+0.00022	−0.00022	*z'*	Lendl et al. (2013)
−525	2455607.56241	+0.00033	−0.00033	*I+z'*	Lendl et al. (2013)
−506	2455622.55057	+0.00026	−0.00026	*I+z'*	Lendl et al. (2013)
−504	2455624.12787	+0.00142	−0.00142	*R*	Mancini et al. (2013)
−493	2455632.80612	+0.00025	−0.00025	*r'*	Lendl et al. (2013)
−464	2455655.68222	+0.00045	−0.00045	*I+z'*	Lendl et al. (2013)
−445	2455670.66976	+0.00064	−0.00064	*I+z'*	Lendl et al. (2013)
−436	2455677.77038	+0.00195	−0.00195	*R*	Mancini et al. (2013)
−422	2455688.81201	+0.00333	−0.00333	*R*	Mancini et al. (2013)
−421	2455689.60276	+0.0003	−0.0003	*R*	Mancini et al. (2013)
−417	2455692.75674	+0.00255	−0.00255	*R*	Mancini et al. (2013)
−416	2455693.54639	+0.00013	−0.00013	*R*	Mancini et al. (2013)
−403	2455703.79933	+0.00411	−0.00411	*R*	Mancini et al. (2013)
−402	2455704.59078	+0.00034	−0.00034	*R*	Mancini et al. (2013)
−397	2455708.53495	+0.00015	−0.00015	*R*	Mancini et al. (2013)
−171	2455886.81234	+0.00208	−0.00208	*R*	Mancini et al. (2013)
−159	2455896.27611	+0.0021	−0.0021	*R*	Mancini et al. (2013)
−135	2455915.2098	+0.00065	−0.00065	*R*	Mancini et al. (2013)
−130	2455919.15485	+0.00103	−0.00103	*R*	Mancini et al. (2013)

Continues on the next page

Table A.2 – continued

Epoch	$T_{\rm mid}$ (BJD)	Residuals		Bandpass	Light Curve Reference
−126	2455922.30966	+0.00555	−0.00555	*R*	Mancini et al. (2013)
−28	2455999.616301	+0.00007	−0.00007	*HK*	Bean et al. (2013)
0	2456021.70374	+0.000085	−0.000085	*HK*	Bean et al. (2013)
10	2456029.5925	+0.00035	−0.00035	*r'*	Lendl et al. (2013)
15	2456033.53645	+0.00014	−0.00014	*g'*	Mancini et al. (2013)
15	2456033.53651	+0.00007	−0.00007	*r'*	Mancini et al. (2013)
15	2456033.53643	+0.00007	−0.00007	*i'*	Mancini et al. (2013)
15	2456033.53652	+0.00009	−0.00009	*z'*	Mancini et al. (2013)
53	2456063.51174	+0.0003	−0.0003	*I+z'*	Lendl et al. (2013)
397	2456334.87208	+0.00053	−0.00053	Clear	Evans P. (TRESCA)
910	2456739.547178	+0.000046	−0.000046	White light	Espinoza et al. (2019)
957	2456776.622511	+0.000066	−0.000066	White light	Espinoza et al. (2019)
1464	2457176.563965	+0.000094	−0.000094	White light	Espinoza et al. (2019)
2250	2457796.591441	+0.000061	−0.000061	White light	Espinoza et al. (2019)
2316	2457848.654791	+0.000068	−0.000068	White light	Espinoza et al. (2019)
2326	2457856.543042	+0.000111	−0.000111	White light	Espinoza et al. (2019)
952	2456772.67789	+0.00052	−0.00052	*I+z'*	Patra et al. (2020)
1933	2457546.53025	+0.00038	−0.00038	*I+z'*	Patra et al. (2020)
3244	2458580.69724	+0.0004	−0.0004	*I+z'*	Patra et al. (2020)
3198	2458544.41098726	+0.0005096953	−0.0005161792	0.6 – 1.0 μm	TESS S9
3199	2458545.19909857	+0.0004676348	−0.0004776159	0.6 – 1.0 μm	TESS S9
3200	2458545.98899546	+0.000459334	−0.0004546766	0.6 – 1.0 μm	TESS S9
3201	2458546.77724425	+0.0004526817	−0.0004699151	0.6 – 1.0 μm	TESS S9
3202	2458547.56694414	+0.0004957815	−0.0005057116	0.6 – 1.0 μm	TESS S9
3203	2458548.35481158	+0.0004678426	−0.0004630053	0.6 – 1.0 μm	TESS S9
3204	2458549.14425338	+0.0004675586	−0.0004538751	0.6 – 1.0 μm	TESS S9
3205	2458549.93228826	+0.0004875952	−0.0004723997	0.6 – 1.0 μm	TESS S9
3206	2458550.72132794	+0.0004917443	−0.0004904705	0.6 – 1.0 μm	TESS S9
3207	2458551.51006035	+0.0005079718	−0.000499857	0.6 – 1.0 μm	TESS S9
3208	2458552.29893896	+0.000491923	−0.0004829233	0.6 – 1.0 μm	TESS S9
3209	2458553.08800457	+0.000490958	−0.0004977896	0.6 – 1.0 μm	TESS S9
3210	2458553.87691279	+0.000444077	−0.0004363738	0.6 – 1.0 μm	TESS S9
3211	2458554.66571083	+0.0004551007	−0.0004432428	0.6 – 1.0 μm	TESS S9
3212	2458555.45433949	+0.0004878705	−0.0004864196	0.6 – 1.0 μm	TESS S9
3215	2458557.82151997	+0.0005212972	−0.0005195209	0.6 – 1.0 μm	TESS S9
3216	2458558.609454	+0.0004931412	−0.000493327	0.6 – 1.0 μm	TESS S9
3217	2458559.39915513	+0.0004648924	−0.000459963	0.6 – 1.0 μm	TESS S9
3218	2458560.18683688	+0.0004597507	−0.0004630294	0.6 – 1.0 μm	TESS S9

Continues on the next page

Table A.2 – continued

Epoch	T_{mid} (BJD)	Residuals		Bandpass	Light Curve Reference
3219	2458560.97725509	+0.0004797756	−0.0004820024	$0.6-1.0$ μm	TESS S9
3220	2458561.76548315	+0.0004690496	−0.0004596392	$0.6-1.0$ μm	TESS S9
3221	2458562.55375174	+0.0004630492	−0.0004569487	$0.6-1.0$ μm	TESS S9
3222	2458563.34272117	+0.000474578	−0.0004586996	$0.6-1.0$ μm	TESS S9
3223	2458564.13193688	+0.0004401143	−0.000421447	$0.6-1.0$ μm	TESS S9
3224	2458564.92115668	+0.0004787526	−0.0004844793	$0.6-1.0$ μm	TESS S9
3225	2458565.70935215	+0.0004918357	−0.000486038	$0.6-1.0$ μm	TESS S9
3226	2458566.49875766	+0.000457878	−0.0004531755	$0.6-1.0$ μm	TESS S9
3227	2458567.28771693	+0.000479046	−0.0004815575	$0.6-1.0$ μm	TESS S9
3228	2458568.07636429	+0.0004715116	−0.000471451	$0.6-1.0$ μm	TESS S9
4134	2459282.76422855	+0.000445984	−0.0004382528	$0.6-1.0$ μm	TESS S36
4135	2459283.55349494	+0.0004680825	−0.0004832548	$0.6-1.0$ μm	TESS S36
4136	2459284.34243336	+0.0005023551	−0.000509186	$0.6-1.0$ μm	TESS S36
4137	2459285.13027096	+0.0004852793	−0.0004831051	$0.6-1.0$ μm	TESS S36
4138	2459285.91977053	+0.0004735948	−0.0004618111	$0.6-1.0$ μm	TESS S36
4139	2459286.70892877	+0.0005314286	−0.0005276405	$0.6-1.0$ μm	TESS S36
4140	2459287.49727343	+0.0004814359	−0.000498216	$0.6-1.0$ μm	TESS S36
4141	2459288.28588867	+0.0004538875	−0.0004737029	$0.6-1.0$ μm	TESS S36
4142	2459289.07496964	+0.0005078695	−0.000492987	$0.6-1.0$ μm	TESS S36
4143	2459289.86351056	+0.0004664274	−0.0004644744	$0.6-1.0$ μm	TESS S36
4144	2459290.65262719	+0.0005161349	−0.0005024358	$0.6-1.0$ μm	TESS S36
4145	2459291.44091157	+0.0005141344	−0.0005178709	$0.6-1.0$ μm	TESS S36
4146	2459292.23014503	+0.0004648569	−0.0004685227	$0.6-1.0$ μm	TESS S36
4150	2459295.38506316	+0.0005516386	−0.0005686305	$0.6-1.0$ μm	TESS S36
4151	2459296.17521974	+0.0004610964	−0.0004679605	$0.6-1.0$ μm	TESS S36
4152	2459296.9630376	+0.0004828338	−0.0004728424	$0.6-1.0$ μm	TESS S36
4153	2459297.75137559	+0.0005018343	−0.000503573	$0.6-1.0$ μm	TESS S36
4154	2459298.53984262	+0.0004852697	−0.0004830355	$0.6-1.0$ μm	TESS S36
4155	2459299.32941899	+0.0004804281	−0.0004758144	$0.6-1.0$ μm	TESS S36
4156	2459300.11844447	+0.0004893952	−0.0004878233	$0.6-1.0$ μm	TESS S36
4157	2459300.90763443	+0.0004986904	−0.0005087346	$0.6-1.0$ μm	TESS S36
4158	2459301.69651184	+0.0004741549	−0.0004809383	$0.6-1.0$ μm	TESS S36
4159	2459302.48452828	+0.0004956919	−0.0004803605	$0.6-1.0$ μm	TESS S36
4160	2459303.27444271	+0.0005392028	−0.0005249785	$0.6-1.0$ μm	TESS S36
4161	2459304.06362531	+0.0004885187	−0.0004994962	$0.6-1.0$ μm	TESS S36
4162	2459304.85196345	+0.000436011	−0.0004488881	$0.6-1.0$ μm	TESS S36
4163	2459305.64011759	+0.000536406	−0.0005166219	$0.6-1.0$ μm	TESS S36

Appendix B

Numerical integration for calculating Love number

Here, we present the numerical integration process to obtain the $\eta(r)$ function. We implement an explicit integration method to solve the differential equation 5.3, a key step in determining the Love numbers k_2 and h_2. Explicit numerical integration methods are commonly used to approximate solutions to ordinary differential equations (ODEs) by progressively calculating function values from an initial condition, using previously computed values at each step. These methods provide an efficient way to solve first-order differential equations, being computationally inexpensive and straightforward to implement.

One of the simplest explicit methods for numerical integration is Euler's Method, which iteratively computes the next value of a function based on the slope at the current point. It is given by:

$$y_{n+1} = y_n + h \left. \frac{dy}{dx} \right|_n \tag{B.1}$$

where y_n is the value of the function at point x_n, y_{n+1} is the function at the next point x_{n+1} and $h = x_{n+1} - x_n$ is the step, given as the difference between the two points. This approach provides a straightforward method to iteratively integrate equation (5.3). However, Euler's method is only first-order accurate, meaning its error scales linearly with h, and it may require a small step size for accurate results.

We rewrite equation (5.3) to explicitly express the derivative $d\eta(r)/dr$:

$$\frac{d\eta(r)}{dr} = \frac{1}{r} \left[-\eta(r)^2 + \eta(r) + 6 - \frac{6\rho(r)}{\rho_m(r)} (\eta(r) + 1) \right] \tag{B.2}$$

Applying Euler's method, we compute $\eta(r)$ at each given radius r_n:

$$\eta(r_{n+1}) = \eta(r_n) + (r_{n+1} - r_n)\frac{1}{r_n}\left[-\eta(r_n)^2 + \eta(r_n) + 6 - \frac{6\rho(r_n)}{\rho_m(r_n)}(\eta(r_n)+1)\right] \quad \text{(B.3)}$$

The remaining values to compute are the density values $\rho(r_n)$ and $\rho_m(r_n)$. The density $\rho_(r_n)$ can be obtained directly from the density profiles, either from the analytical model or the output from the MESA model, while $\rho_m(r_n)$ is given by the average density enclosed within r_n.

When using the analytical model, we can calculate $\rho_m(r)$ straight from equation 5.8. When using MESA, or any other non-analytical software or method, we do not have the final expression for the density profile. Therefore, we compute the integral numerically using a discrete summation over radial points. Given a discrete set of radial grid points r_n where $\rho(r)$ is known, the integral is approximated by summation:

$$\rho_m(r_n) = \frac{3}{r_n^3}\sum_{i=1}^{n}\rho(r_i)r_i^2\Delta r \quad \text{(B.4)}$$

where $rho(r_i)$ is the density at radius r_i and $\Delta r = r_{i+1} - r_i$ is the step size. This approach allows the mean density to be dynamically updated as the integration progresses.

We can rewrite the above equation in the following way, making it easier to implement.

$$\rho_m(r_n) = \rho_m(r_{n-1}) + \frac{\rho(r_n)(r_n^3 - r_{n-1}^3)}{r_n^3} \quad \text{(B.5)}$$

The above methods and equations are then implemented in a Python script, which is used to calculate the $\eta(r)$ function and evaluate k_2 through equation 5.2.

Bibliography

Acuña, L., Deleuil, M., Mousis, O., et al. 2021, Astronomy & Astrophysics, 647, A53 [Cited on pages 4 and 16.]

Adibekyan, V., Dorn, C., Sousa, S. G., et al. 2021, Science, 374, 330 [Cited on pages 15, 58, 64, and 98.]

Aigrain, S., Pont, F., & Zucker, S. 2012, Monthly notices of the royal astronomical society, 419, 3147 [Cited on page 31.]

Akeson, R. L., Chen, X., Ciardi, D., et al. 2013, Publications of the Astronomical Society of the Pacific, 125, 989 [Cited on pages xiii, 2, and 3.]

Akinsanmi, B., Barros, S., Lendl, M., et al. 2024, arXiv preprint arXiv:2402.10486 [Cited on pages 20, 68, and 99.]

Akinsanmi, B., Barros, S., Santos, N., et al. 2019, Astronomy & Astrophysics, 621, A117 [Cited on pages xiii, 9, 18, and 19.]

Akinsanmi, B., Santos, N., Faria, J., et al. 2020, Astronomy & Astrophysics, 635, L8 [Cited on pages 9, 10, and 14.]

Alston, C., Kuhnert, P., Choy, L. S., McVinish, R., & Mengersen, K. 2005, International Statistical Insitute, 55th session [Cited on page 37.]

Ambikasaran, S., Foreman-Mackey, D., Greengard, L., Hogg, D. W., & O'Neil, M. 2015, IEEE Transactions on Pattern Analysis and Machine Intelligence, 38, 252 [Cited on page 51.]

Anderson, D., Gillon, M., Maxted, P., et al. 2010, Astronomy & Astrophysics, 513, L3 [Cited on page 106.]

Anglada-Escudé, G., Tuomi, M., Arriagada, P., et al. 2016, The Astrophysical Journal, 830, 74 [Cited on page 31.]

Artigau, É., Bouchy, F., Doyon, R., et al. 2024, in Ground-based and Airborne Instrumentation for Astronomy X, Vol. 13096, SPIE, 71–87 [Cited on page 8.]

Auvergne, M., Bodin, P., Boisnard, L., et al. 2009, Astronomy & Astrophysics, 506, 411 [Cited on page 12.]

Baranne, A., Queloz, D., Mayor, M., et al. 1996, Astronomy and Astrophysics Supplement Series, 119, 373 [Cited on pages 6, 8, 30, and 43.]

Barnes, J. W. & Fortney, J. J. 2004, The Astrophysical Journal, 616, 1193 [Cited on page 9.]

Barragán, O., Gillen, E., Aigrain, S., et al. 2023, Monthly Notices of the Royal Astronomical Society, 522, 3458 [Cited on page 31.]

Barros, S., Boué, G., Gibson, N., et al. 2013, Monthly Notices of the Royal Astronomical Society, 430, 3032 [Cited on pages 10 and 71.]

Barros, S., Demangeon, O., Alibert, Y., et al. 2022a, Astronomy & Astrophysics, 665, A154 [Cited on pages 3 and 52.]

Barros, S., Demangeon, O., Diaz, R. F., et al. 2020, Astronomy & Astrophysics, 634, A75 [Cited on pages 24, 32, and 46.]

Barros, S. C., Akinsanmi, B., Boué, G., et al. 2022b, Astronomy & Astrophysics, 657, A52 [Cited on pages 9, 18, 20, 29, 33, 38, 46, 69, 88, 89, 92, 93, and 94.]

Barros, S. C. C., Akinsanmi, B., Alibert, Y., et al. 2024, JWST Proposal. Cycle 3, 5022 [Cited on page 89.]

Baştürk, Ö., Southworth, J., Yalçınkaya, S., et al. 2023, Monthly Notices of the Royal Astronomical Society, 521, 1200 [Cited on page 69.]

Batalha, N. M. 2014, Proceedings of the National Academy of Sciences, 111, 12647 [Cited on pages 1, 4, and 5.]

Batygin, K. & Stevenson, D. J. 2013, The Astrophysical Journal Letters, 769, L9 [Cited on page 91.]

Baumeister, P., Padovan, S., Tosi, N., et al. 2020, The Astrophysical Journal, 889, 42 [Cited on pages 16 and 89.]

Bean, J. L., Désert, J.-M., Seifahrt, A., et al. 2013, The Astrophysical Journal, 771, 108 [Cited on page 108.]

Benz, W., Broeg, C., Fortier, A., et al. 2021, Experimental Astronomy, 51, 109 [Cited on page 13.]

Bernabo, L. M., Csizmadia, S., Smith, A., et al. 2024, Astronomy & Astrophysics, 684, A78 [Cited on page 82.]

Bitsch, B., Raymond, S. N., & Izidoro, A. 2019, Astronomy & Astrophysics, 624, A109 [Cited on page 5.]

Bodenheimer, P., Lin, D., & Mardling, R. 2001, The Astrophysical Journal, 548, 466 [Cited on page 94.]

Bonati, I., Lasbleis, M., & Noack, L. 2021, Journal of Geophysical Research: Planets, 126, e2020JE006724 [Cited on page 64.]

Bonfanti, A., Brady, M., Wilson, T., et al. 2024, Astronomy & Astrophysics, 682, A66 [Cited on pages 5, 33, and 38.]

Borucki, W. J., Koch, D., Basri, G., et al. 2010, Science, 327, 977 [Cited on page 12.]

Brown, T. M., Charbonneau, D., Gilliland, R. L., Noyes, R. W., & Burrows, A. 2001, The Astrophysical Journal, 552, 699 [Cited on page 12.]

Brugger, B., Mousis, O., Deleuil, M., & Deschamps, F. 2017, The Astrophysical Journal, 850, 93 [Cited on page 15.]

Buhler, P. B., Knutson, H. A., Batygin, K., et al. 2016, The Astrophysical Journal, 821, 26 [Cited on pages 86, 91, and 95.]

Burke, C. J., Bryson, S. T., Mullally, F., et al. 2014, The Astrophysical Journal Supplement Series, 210, 19 [Cited on page 24.]

Butler, R. P., Marcy, G. W., Williams, E., et al. 1996, Publications of the Astronomical Society of the Pacific, 108, 500 [Cited on page 43.]

Butters, O., West, R. G., Anderson, D., et al. 2010, Astronomy & Astrophysics, 520, L10 [Cited on page 103.]

Carter, J. A. & Winn, J. N. 2010, The Astrophysical Journal, 709, 1219 [Cited on page 18.]

Chandrasekhar, S. 1987, New York: Dover [Cited on pages 17 and 18.]

Charbonneau, D., Berta, Z. K., Irwin, J., et al. 2009, Nature, 462, 891 [Cited on page 24.]

Charbonneau, D., Brown, T. M., Latham, D. W., & Mayor, M. 1999, The Astrophysical Journal, 529, L45 [Cited on page 12.]

Chen, H. & Rogers, L. A. 2016, The Astrophysical Journal, 831, 180 [Cited on pages 91 and 94.]

Ciardi, D. R., Beichman, C. A., Horch, E. P., & Howell, S. B. 2015, The Astrophysical Journal, 805, 16 [Cited on page 45.]

Cincunegui, C., Diaz, R. F., & Mauas, P. J. D. 2007, Astronomy & Astrophysics, 469, 309 [Cited on page 32.]

Claret, A. 2000, Astronomy and Astrophysics, v. 363, p. 1081-1190 (2000), 363, 1081 [Cited on page 28.]

Claret, A. 2017, Astronomy & Astrophysics, 600, A30 [Cited on pages 10 and 29.]

Cloutier, R., Astudillo-Defru, N., Bonfils, X., et al. 2019, Astronomy & Astrophysics, 629, A111 [Cited on page 32.]

Cloutier, R. & Menou, K. 2020, The Astronomical Journal, 159, 211 [Cited on page 5.]

Correia, A. C. 2014, Astronomy & Astrophysics, 570, L5 [Cited on pages xiii, 9, 18, 19, and 20.]

Correia, A. C. & Rodriguez, A. 2013, The Astrophysical Journal, 767, 128 [Cited on pages 17, 18, 19, and 86.]

Cortés-Zuleta, P., Rojo, P., Wang, S., et al. 2020, Astronomy & Astrophysics, 636, A98 [Cited on pages 69, 70, 103, and 104.]

Costes, J. C., Watson, C. A., de Mooij, E., et al. 2021, Monthly Notices of the Royal Astronomical Society, 505, 830 [Cited on page 32.]

Crane, J. D., Shectman, S. A., & Butler, R. P. 2006, in Ground-based and Airborne Instrumentation for Astronomy, Vol. 6269, SPIE, 972–982 [Cited on page 43.]

Crane, J. D., Shectman, S. A., Butler, R. P., et al. 2010, in Ground-based and Airborne Instrumentation for Astronomy III, Vol. 7735, SPIE, 1909–1923 [Cited on page 43.]

Crane, J. D., Shectman, S. A., Butler, R. P., Thompson, I. B., & Burley, G. S. 2008, in Ground-based and Airborne Instrumentation for Astronomy II, Vol. 7014, SPIE, 2484–2493 [Cited on page 43.]

Csizmadia, S., Pasternacki, T., Dreyer, C., et al. 2013, Astronomy & Astrophysics, 549, A9 [Cited on page 29.]

Da Silva, J. G., Santos, N., Bonfils, X., et al. 2012, Astronomy & Astrophysics, 541, A9 [Cited on page 31.]

Davoudi, F., Baştürk, Ö., Yalçınkaya, S., Esmer, E. M., & Safari, H. 2021, The Astronomical Journal, 162, 210 [Cited on page 69.]

de Beurs, Z. L., Vanderburg, A., Shallue, C. J., et al. 2022, The Astronomical Journal, 164, 49 [Cited on page 32.]

Delrez, L., Ehrenreich, D., Alibert, Y., et al. 2021, Nature Astronomy, 5, 775 [Cited on page 15.]

Demangeon, O., Cubillos, P., Singh, V., et al. 2024, Astronomy & Astrophysics, 684, A27 [Cited on pages 9 and 14.]

Demangeon, O. D., Faedi, F., Hébrard, G., et al. 2018, Astronomy & Astrophysics, 610, A63 [Cited on page 52.]

Demangeon, O. D., Osorio, M. Z., Alibert, Y., et al. 2021, Astronomy & Astrophysics, 653, A41 [Cited on pages 33 and 52.]

Dorn, C., Khan, A., Heng, K., et al. 2015, Astronomy & Astrophysics, 577, A83 [Cited on pages 4 and 15.]

Dorn, C. & Lichtenberg, T. 2021, The Astrophysical Journal Letters, 922, L4 [Cited on pages 4, 16, 63, and 64.]

Dorn, C., Venturini, J., Khan, A., et al. 2017, Astronomy & Astrophysics, 597, A37 [Cited on pages 4, 15, 16, and 62.]

Dubber, S. C., Mortier, A., Rice, K., et al. 2019, Monthly Notices of the Royal Astronomical Society, 490, 5103 [Cited on page 53.]

Dumusque, X., Pepe, F., Lovis, C., et al. 2012, Nature, 491, 207 [Cited on page 31.]

Dumusque, X., Turner, O., Dorn, C., et al. 2019, Astronomy & Astrophysics, 627, A43 [Cited on pages 1, 5, 39, 40, 43, 48, 56, 62, and 98.]

Durante, D., Parisi, M., Serra, D., et al. 2020, Geophysical Research Letters, 47, e2019GL086572 [Cited on pages 87 and 88.]

Dziewonski, A. M. & Anderson, D. L. 1981, Physics of the earth and planetary interiors, 25, 297 [Cited on page 15.]

Efron, B., Gous, A., Kass, R., Datta, G., & Lahiri, P. 2001, Lecture Notes-Monograph Series, 208 [Cited on page 37.]

Egger, J., Osborn, H., Kubyshkina, D., et al. 2024, Astronomy & Astrophysics, 688, A223 [Cited on pages 4, 16, and 59.]

Espinoza, N. & Jordán, A. 2015, Monthly Notices of the Royal Astronomical Society, 450, 1879 [Cited on page 29.]

Espinoza, N., Rackham, B. V., Jordán, A., et al. 2019, Monthly Notices of the Royal Astronomical Society, 482, 2065 [Cited on pages 69, 70, 76, 82, and 108.]

Faria, J., Adibekyan, V., Amazo-Gómez, E., et al. 2020, Astronomy & Astrophysics, 635, A13 [Cited on page 31.]

Faria, J., Haywood, R., Brewer, B., et al. 2016, Astronomy & Astrophysics, 588, A31 [Cited on page 32.]

Fischer, D. A., Anglada-Escude, G., Arriagada, P., et al. 2016, Publications of the Astronomical Society of the Pacific, 128, 066001 [Cited on page 31.]

Folkner, W., Iess, L., Anderson, J., et al. 2017, Geophysical Research Letters, 44, 4694 [Cited on page 87.]

Ford, E. B. 2005, The Astronomical Journal, 129, 1706 [Cited on page 49.]

Foreman-Mackey, D., Hogg, D. W., Lang, D., & Goodman, J. 2013, Publications of the Astronomical Society of the Pacific, 125, 306 [Cited on pages 37 and 52.]

Fortney, J., Militzer, B., Mankovich, C., et al. 2023, arXiv preprint arXiv:2304.09215 [Cited on page 89.]

Fortney, J. J., Dawson, R. I., & Komacek, T. D. 2021, Journal of Geophysical Research: Planets, 126, e2020JE006629 [Cited on pages xvi, 93, 94, and 95.]

Fortney, J. J., Marley, M. S., & Barnes, J. W. 2007, The Astrophysical Journal, 659, 1661 [Cited on page 15.]

Fortney, J. J. & Nettelmann, N. 2010, Space Science Reviews, 152, 423 [Cited on page 86.]

Forveille, T., Bonfils, X., Delfosse, X., et al. 2009, Astronomy & Astrophysics, 493, 645 [Cited on page 31.]

Fressin, F., Torres, G., Charbonneau, D., et al. 2013, The Astrophysical Journal, 766, 81

Fulton, B. J., Petigura, E. A., Blunt, S., & Sinukoff, E. 2018, Publications of the Astronomical Society of the Pacific, 130, 044504 [Cited on page 49.]

Fulton, B. J., Petigura, E. A., Howard, A. W., et al. 2017, The Astronomical Journal, 154, 109 [Cited on pages xiii, 4, 5, and 62.]

Gaia Collaboration. 2020, I/350yCatI/350 [Cited on page 43.]

Gaia Collaboration, Vallenari, A., Brown, A. G. A., et al. 2023, Astronomy & Astrophysics, 674, A1 [Cited on page 44.]

Gaillard, F., Bouhifd, M. A., Füri, E., et al. 2021, Space Science Reviews, 217, 1 [Cited on page 64.]

Gandolfi, D., Fossati, L., Livingston, J. H., et al. 2019, The Astrophysical Journall, 876, L24 [Cited on pages 1, 5, 39, 40, 43, 48, 56, 62, and 66.]

Gardner, J. P., Mather, J. C., Clampin, M., et al. 2006, Space Science Reviews, 123, 485 [Cited on page 14.]

Gaudi, B. S., Stassun, K. G., Collins, K. A., et al. 2017, Nature, 546, 514 [Cited on page 69.]

Gilliland, R. L., Chaplin, W. J., Dunham, E. W., et al. 2011, The Astrophysical Journal Supplement Series, 197, 6 [Cited on page 24.]

Gillon, M., Anderson, D., Collier-Cameron, A., et al. 2014, Astronomy & Astrophysics, 562, L3 [Cited on page 69.]

Ginzburg, S., Schlichting, H. E., & Sari, R. 2018, Monthly Notices of the Royal Astronomical Society, 476, 759 [Cited on page 5.]

Goldreich, P. & Soter, S. 1966, icarus, 5, 375 [Cited on page 17.]

Goodman, J. & Weare, J. 2010, Communications in applied mathematics and computational science, 5, 65 [Cited on page 37.]

Grasset, O., Schneider, J., & Sotin, C. 2009, The Astrophysical Journal, 693, 722 [Cited on page 15.]

Gregory, P. 2005, Bayesian logical data analysis for the physical sciences: A comparative approach with Mathematica® support (Cambridge University Press) [Cited on page 36.]

Grunblatt, S. K., Huber, D., Gaidos, E., et al. 2017, The Astronomical Journal, 154, 254 [Cited on page 24.]

Guillot, T. & Showman, A. P. 2002, Astronomy & Astrophysics, 385, 156 [Cited on page 94.]

Gupta, A. & Schlichting, H. E. 2019, Monthly Notices of the Royal Astronomical Society, 487, 24 [Cited on page 5.]

Hakim, K., Rivoldini, A., Van Hoolst, T., et al. 2018, Icarus, 313, 61 [Cited on page 58.]

Haldemann, J., 201, C., Venturini, J., Alibert, Y., & Benz, W. 2024, Astronomy & Astrophysics, 681, A96 [Cited on pages 16 and 59.]

Haldemann, J., Alibert, Y., Mordasini, C., & Benz, W. 2020, Astronomy & Astrophysics, 643, A105 [Cited on page 58.]

Haldemann, J., Ksoll, V., Walter, D., et al. 2023, Astronomy & Astrophysics, 672, A180 [Cited on page 16.]

Harre, J.-V., Smith, A., Barros, S., et al. 2023, Astronomy & Astrophysics, 669, A124 [Cited on pages 10, 38, and 69.]

Haywood, R., Collier Cameron, A., Queloz, D., et al. 2014, Monthly notices of the royal astronomical society, 443, 2517 [Cited on pages 32 and 33.]

Haywood, R. D. 2016, Radial-velocity Searches for Planets Around Active Stars, 13 [Cited on page 32.]

He, H., Wang, H., & Yun, D. 2015, The Astrophysical Journal Supplement Series, 221, 18 [Cited on page 24.]

Hearnshaw, J. B. 2014, The Doppler effect (Cambridge University Press), 86–126 [Cited on page 6.]

Hebb, L., Collier-Cameron, A., Loeillet, B., et al. 2009a, The Astrophysical Journal, 693, 1920 [Cited on page 68.]

Hebb, L., Collier-Cameron, A., Triaud, A., et al. 2009b, The Astrophysical Journal, 708, 224 [Cited on pages 1, 70, 76, 82, and 106.]

Helled, R., Bodenheimer, P., Podolak, M., et al. 2014, in Protostars and Planets VI, ed. H. Beuther, R. S. Klessen, C. P. Dullemond, & T. Henning, 643–665 [Cited on pages 2, 87, and 90.]

Hellier, C., Anderson, D., Cameron, A. C., et al. 2009, Nature, 460, 1098 [Cited on pages 69 and 103.]

Hellier, C., Anderson, D., Cameron, A. C., et al. 2011a, Astronomy & Astrophysics, 535, L7 [Cited on page 69.]

Hellier, C., Anderson, D., Collier-Cameron, A., et al. 2011b, The Astrophysical Journal Letters, 730, L31 [Cited on pages 9 and 74.]

Hestroffer, D. 1997, Astronomy and Astrophysics, v. 327, p. 199-206, 327, 199 [Cited on page 28.]

Hippke, M., David, T. J., Mulders, G. D., & Heller, R. 2019, The Astronomical Journal, 158, 143 [Cited on page 24.]

Hirzberger, J., Gizon, L., Solanki, S. K., & Duvall, T. L. 2008, Helioseismology, Asteroseismology, and MHD Connections, 415 [Cited on page 24.]

Howell, S. B., Sobeck, C., Haas, M., et al. 2014, Publications of the Astronomical Society of the Pacific, 126, 398 [Cited on page 12.]

Hoyer, S., Bonfanti, A., Leleu, A., et al. 2022, Astronomy & Astrophysics, 668, A117 [Cited on page 29.]

Hoyer, S., Guterman, P., Demangeon, O., et al. 2020, Astronomy & Astrophysics, 635, A24 [Cited on pages 27 and 46.]

Huélamo, N., Figueira, P., Bonfils, X., et al. 2008, Astronomy & Astrophysics, 489, L9 [Cited on page 31.]

Husser, T.-O., Wende-von Berg, S., Dreizler, S., et al. 2013, A&A, 553, A6 [Cited on page 29.]

Ivshina, E. S. & Winn, J. N. 2022, The Astrophysical Journal Supplement Series, 259, 62 [Cited on pages 81 and 82.]

Jenkins, J. M. 2020, Kepler Science Document KSCI-19081-003, 2 [Cited on page 25.]

Kaltenegger, L. 2017, Annual Review of Astronomy and Astrophysics, 55, 433 [Cited on page 1.]

Kass, R. E. & Raftery, A. E. 1995, Journal of the american statistical association, 90, 773 [Cited on page 37.]

Kedziora-Chudczer, L., Zhou, G., Bailey, J., et al. 2019, Monthly Notices of the Royal Astronomical Society, 483, 5110 [Cited on page 104.]

Kipping, D. M. 2013, Monthly Notices of the Royal Astronomical Society: Letters, 434, L51 [Cited on pages 34, 35, and 53.]

Kopal, Z. 1950, Harvard College Observatory Circular, 454, pp. 1-12, 454, 1 [Cited on page 28.]

Kramm, U., Nettelmann, N., Redmer, R., & Stevenson, D. J. 2011, Astronomy & Astrophysics, 528, A18 [Cited on page 88.]

Kreidberg, L. 2015, Publications of the Astronomical Society of the Pacific, 127, 1161 [Cited on pages 11 and 51.]

Kubyshkina, D. & Fossati, L. 2022, Astronomy & Astrophysics, 668, A178 [Cited on pages 91 and 94.]

Kubyshkina, D., Vidotto, A. A., Fossati, L., & Farrell, E. 2020, Monthly Notices of the Royal Astronomical Society, 499, 77 [Cited on pages 91 and 94.]

Kuerster, M., Endl, M., Rouesnel, F., et al. 2003, Astronomy & Astrophysics, 403, 1077 [Cited on page 43.]

Lafarga, M., Ribas, I., Lovis, C., et al. 2020, Astronomy & Astrophysics, 636, A36 [Cited on page 32.]

Lainey, V., Jacobson, R. A., Tajeddine, R., et al. 2017, Icarus, 281, 286 [Cited on page 89.]

Lee, E. J. & Chiang, E. 2016, The Astrophysical Journal, 817, 90 [Cited on page 5.]

Léger, A., Rouan, D., Schneider, J., et al. 2009, Astronomy & Astrophysics, 506, 287 [Cited on page 12.]

Leleu, A., Alibert, Y., Hara, N. C., et al. 2021, Astronomy & Astrophysics, 649, A26 [Cited on pages 4, 15, 16, 33, 57, and 58.]

Lendl, M., Csizmadia, S., Deline, A., et al. 2020, Astronomy & Astrophysics, 643, A94 [Cited on pages 9 and 46.]

Lendl, M., Gillon, M., Queloz, D., et al. 2013, Astronomy & Astrophysics, 552, A2 [Cited on pages 106, 107, and 108.]

Lester, K. V., Matson, R. A., Howell, S. B., et al. 2021, The Astronomical Journal, 162, 75 [Cited on pages 44 and 66.]

Liddle, A. R. 2007, Monthly Notices of the Royal Astronomical Society: Letters, 377, L74 [Cited on page 37.]

Lillo-Box, J., Lopez, T. A., Santerne, A., et al. 2020, Astronomy & Astrophysics, 640, A48 [Cited on page 3.]

Lin, D. N., Bodenheimer, P., & Richardson, D. C. 1996, Nature, 380, 606 [Cited on pages 1 and 2.]

Liu, S.-F., Hori, Y., Lin, D., & Asphaug, E. 2015, The Astrophysical Journal, 812, 164 [Cited on page 5.]

Lo Curto, G., Pepe, F., Avila, G., et al. 2015, The Messenger, 162, 9 [Cited on page 8.]

Lopez, E. D. & Fortney, J. J. 2014, The Astrophysical Journal, 792, 1 [Cited on page 58.]

Love, A. E. H. 1909, Proceedings of the Royal Society of London. Series A, Containing Papers of a Mathematical and Physical Character, 82, 73 [Cited on page 18.]

Lovis, C., Fischer, D., et al. 2010, Exoplanets, 27 [Cited on page 6.]

Lovis, C. & Pepe, F. 2007, Astronomy & Astrophysics, 468, 1115 [Cited on page 43.]

Lozovsky, M., Helled, R., Rosenberg, E. D., & Bodenheimer, P. 2017, The Astrophysical Journal, 836, 227 [Cited on page 88.]

Maciejewski, G., Fernández, M., Aceituno, F., et al. 2018, arXiv preprint arXiv:1812.02438 [Cited on pages 2, 18, and 69.]

Maciejewski, G., Knutson, H. A., Howard, A. W., et al. 2020, Acta Astronomica, 70, 1 [Cited on pages 18, 29, 69, 70, 75, 76, 81, 103, 104, and 105.]

Mancini, L., Ciceri, S., Chen, G., et al. 2013, Monthly Notices of the Royal Astronomical Society, 436, 2 [Cited on pages 69, 70, 76, 82, 107, and 108.]

Mancini, L., Southworth, J., Naponiello, L., et al. 2022, Monthly Notices of the Royal Astronomical Society, 509, 1447 [Cited on page 69.]

Mandel, K. & Agol, E. 2002, The Astrophysical Journal, 580, L171 [Cited on page 28.]

Mankovich, C. R. & Fuller, J. 2021, Nature Astronomy, 5, 1103 [Cited on page 89.]

Marboeuf, U., Thiabaud, A., Alibert, Y., Cabral, N., & Benz, W. 2014, Astronomy & Astrophysics, 570, A36 [Cited on page 59.]

Marcy, G. W., Butler, R. P., Williams, E., et al. 1997, The Astrophysical Journal, 481, 926 [Cited on page 8.]

Martinez, C. F., Cunha, K., Ghezzi, L., & Smith, V. V. 2019, The Astrophysical Journal, 875, 29 [Cited on page 5.]

Maxted, P. 2018, Astronomy & Astrophysics, 616, A39 [Cited on page 28.]

Maxted, P., Anderson, D., Doyle, A., et al. 2013, Monthly Notices of the Royal Astronomical Society, 428, 2645 [Cited on page 103.]

Maxted, P. F. L., Ehrenreich, D., Wilson, T. G., et al. 2022, MNRAS, 514, 77 [Cited on pages 27 and 46.]

Mayo, A. W., Vanderburg, A., Latham, D. W., et al. 2018, The Astronomical Journal, 155, 136 [Cited on page 24.]

Mayor, M., Marmier, M., Lovis, C., et al. 2011, Astronomy and Astrophysics Manuscript No. HARPS˙ stat [Cited on pages 5 and 7.]

Mayor, M., Pepe, F., Queloz, D., et al. 2003, The Messenger, 114, 20 [Cited on page 8.]

Mayor, M. & Queloz, D. 1995, nature, 378, 355 [Cited on pages 2 and 8.]

McDonald, I. & Kerins, E. 2018, Monthly Notices of the Royal Astronomical Society: Letters, 477, L21 [Cited on page 70.]

Mehrabi, A., He, H., & Khosroshahi, H. 2017, The Astrophysical Journal, 834, 207 [Cited on page 24.]

Meibom, S. & Mathieu, R. D. 2005, The Astrophysical Journal, 620, 970 [Cited on page 17.]

Meunier, N., Desort, M., & Lagrange, A.-M. 2010, Astronomy & Astrophysics, 512, A39 [Cited on page 31.]

Militzer, B., Wahl, S., & Hubbard, W. 2019, The Astrophysical Journal, 879, 78 [Cited on page 89.]

Milne, E. A. 1921, Monthly Notices of the Royal Astronomical Society, 81, 361 [Cited on page 28.]

Morales, J. C., Mustill, A., Ribas, I., et al. 2019, Science, 365, 1441 [Cited on page 1.]

Morello, G., Tsiaras, A., Howarth, I. D., & Homeier, D. 2017, The Astronomical Journal, 154, 111 [Cited on pages 10 and 29.]

Morris, B., Delrez, L., Brandeker, A., et al. 2021, Astronomy & Astrophysics, 653, A173 [Cited on pages 38 and 46.]

Murray, C. D. & Correia, A. C. 2010, Exoplanets, 1, 15 [Cited on page 7.]

Nelder, J. A. & Mead, R. 1965, The computer journal, 7, 308 [Cited on page 52.]

Noyes, R., Hartmann, L., Baliunas, S., Duncan, D., & Vaughan, A. 1984, Astrophysical Journal, Part 1 (ISSN 0004-637X), vol. 279, April 15, 1984, p. 763-777. Research supported by the Smithsonian Institution and National Geographic Society., 279, 763 [Cited on page 32.]

Nymeyer, S., Harrington, J., Hardy, R. A., et al. 2011, The Astrophysical Journal, 742, 35 [Cited on page 74.]

Oberst, T. E., Rodriguez, J. E., Colón, K. D., et al. 2017, The Astronomical Journal, 153, 97 [Cited on page 69.]

Ogilvie, G. I. 2014, Annual Review of Astronomy and Astrophysics, 52, 171 [Cited on page 17.]

Ogilvie, G. I. & Lin, D. 2007, The Astrophysical Journal, 661, 1180 [Cited on pages 17 and 18.]

Oshagh, M., Santos, N. C., Boisse, I., et al. 2013, Astronomy & Astrophysics, 556, A19 [Cited on page 24.]

Otegi, J. F., Dorn, C., Helled, R., et al. 2020, Astronomy & Astrophysics, 640, A135 [Cited on pages 4, 41, 55, and 62.]

Owen, J. E. & Wu, Y. 2017, The Astrophysical Journal, 847, 29 [Cited on page 5.]

Padovan, S., Spohn, T., Baumeister, P., et al. 2018, Astronomy & Astrophysics, 620, A178 [Cited on page 101.]

Parviainen, H. & Aigrain, S. 2015, Monthly Notices of the Royal Astronomical Society, 453, 3821 [Cited on page 29.]

Patra, K. C., Winn, J. N., Holman, M. J., et al. 2020, The Astronomical Journal, 159, 150 [Cited on pages 9, 67, 70, 81, 82, 104, and 108.]

Paxton, B., Cantiello, M., Arras, P., et al. 2013, The Astrophysical Journal Supplement Series, 208, 4 [Cited on page 91.]

Paxton, B., Schwab, J., Bauer, E. B., et al. 2018, The Astrophysical Journal Supplement Series, 234, 34 [Cited on page 91.]

Pepe, F., Cristiani, S., Rebolo, R., et al. 2021, Astronomy & Astrophysics, 645, A96 [Cited on page 8.]

Pepe, F., Mayor, M., Galland, F., et al. 2002, Astronomy & Astrophysics, 388, 632 [Cited on page 30.]

Pepe, F., Mayor, M., Galland, F., et al. 2002, Astronomy & Astrophysics, 388, 632 [Cited on page 43.]

Pepe, F., Mayor, M., Rupprecht, G., et al. 2002, Messenger, 110, 9 [Cited on page 8.]

Perger, M., Anglada-Escudé, G., Ribas, I., et al. 2021, Astronomy & Astrophysics, 645, A58 [Cited on page 32.]

Perryman, M. 2018, The exoplanet handbook (Cambridge university press) [Cited on pages 7 and 12.]

Petigura, E. A. 2020, The Astronomical Journal, 160, 89 [Cited on page 5.]

Petrucci, R., Jofré, E., Gómez Maqueo Chew, Y., et al. 2020, Monthly Notices of the Royal Astronomical Society, 491, 1243 [Cited on pages 70, 81, and 82.]

Pojmanski, G. 1997, Acta Astronomica, 47, 467 [Cited on page 103.]

Priest, E. 2014, Magnetohydrodynamics of the Sun (Cambridge University Press) [Cited on page 24.]

Prieto-Arranz, J., Palle, E., Gandolfi, D., et al. 2018, Astronomy & Astrophysics, 618, A116 [Cited on page 39.]

Queloz, D., Henry, G. W., Sivan, J.-P., et al. 2001, Astronomy & Astrophysics, 379, 279 [Cited on pages 30 and 31.]

Queloz, D., Mayor, M., Weber, L., et al. 2000, Astronomy and Astrophysics, v. 354, p. 99-102 (2000), 354, 99 [Cited on page 8.]

Ragozzine, D. & Wolf, A. S. 2009, The Astrophysical Journal, 698, 1778 [Cited on page 88.]

Rajpaul, V., Aigrain, S., Osborne, M. A., Reece, S., & Roberts, S. 2015, Monthly Notices of the Royal Astronomical Society, 452, 2269 [Cited on pages 32 and 33.]

Rasmussen, C. E. & Williams, C. K. 2006 (MIT press Cambridge, MA) [Cited on page 33.]

Rauer, H., Aerts, C., Cabrera, J., et al. 2024, arXiv e-prints, arXiv:2406.05447 [Cited on pages 14, 55, and 98.]

Rice, K., Malavolta, L., Mayo, A., et al. 2019, Monthly Notices of the Royal Astronomical Society, 484, 3731 [Cited on page 24.]

Ricker, G. R., Winn, J. N., Vanderspek, R., et al. 2015, Journal of Astronomical Telescopes, Instruments, and Systems, 1, 014003 [Cited on page 12.]

Robert, C. P., Casella, G., Robert, C. P., & Casella, G. 2004, Monte Carlo statistical methods, 267 [Cited on page 37.]

Rogers, L. & Seager, S. 2010, The Astrophysical Journal, 712, 974 [Cited on page 15.]

Rosário, N., Demangeon, O., Barros, S., et al. 2024, Astronomy & Astrophysics, 686, A282 [Cited on pages xiv, xv, 1, 3, 26, 42, 44, 51, 54, 55, 56, 57, 60, 61, and 63.]

Rosário, N. M., Barros, S. C. C., Demangeon, O. D. S., & Santos, N. C. 2022, Astronomy & Astrophysics, 668, A114 [Cited on pages xv, xvi, 10, 26, 67, 72, 73, 74, 75, 78, 79, 80, and 81.]

Sainsbury-Martinez, F., Wang, P., Fromang, S., et al. 2019, Astronomy & Astrophysics, 632, A114 [Cited on page 94.]

Santerne, A., Díaz, R., Moutou, C., et al. 2012, Astronomy & Astrophysics, 545, A76

Santos, N., Mayor, M., Naef, D., et al. 2000, Astronomy and Astrophysics, v. 361, p. 265-272 (2000), 361, 265 [Cited on page 31.]

Santos, N., Mortier, A., Faria, J., et al. 2014, Astronomy & Astrophysics, 566, A35 [Cited on pages 31 and 32.]

Santos, N. C. 2008, New Astronomy Reviews, 52, 154 [Cited on page 31.]

Santos, N. C., Barros, S. C., Demangeon, O. D., & Faria, J. P. 2020, in Oxford Research Encyclopedia of Planetary Science [Cited on pages 3, 6, 7, and 9.]

Schwab, C., Rakich, A., Gong, Q., et al. 2016, in Ground-based and airborne instrumentation for astronomy vi, Vol. 9908, SPIE, 2220–2225 [Cited on page 8.]

Schwarz, G. 1978, The annals of statistics, 461 [Cited on page 37.]

Seager, S. & Hui, L. 2002, The Astrophysical Journal, 574, 1004 [Cited on pages 18 and 20.]

Seager, S., Kuchner, M., Hier-Majumder, C., & Militzer, B. 2007, The Astrophysical Journal, 669, 1279 [Cited on page 15.]

Seager, S. & Mallén-Ornelas, G. 2003, The Astrophysical Journal, 585, 1038 [Cited on pages 9 and 11.]

Serrano, L., Barros, S., Oshagh, M., et al. 2018, Astronomy & Astrophysics, 611, A8 [Cited on page 24.]

Sharma, S. 2017, Annual Review of Astronomy and Astrophysics, 55, 213 [Cited on page 36.]

Short, D. R., Welsh, W. F., Orosz, J. A., Windmiller, G., & Maxted, P. F. L. 2019, Research Notes of the American Astronomical Society, 3, 117 [Cited on page 29.]

Showman, A. P. & Guillot, T. 2002, Astronomy & Astrophysics, 385, 166 [Cited on page 93.]

Shporer, A., Wong, I., Huang, C. X., et al. 2019, The Astronomical Journal, 157, 178 [Cited on pages 24, 69, 70, 75, and 81.]

Simola, U., Dumusque, X., & Cisewski-Kehe, J. 2019, Astronomy & Astrophysics, 622, A131 [Cited on page 32.]

Simon, A., Szabó, G. M., Kiss, L. L., Fortier, A., & Benz, W. 2015, Publications of the Astronomical Society of the Pacific, 127, 1084 [Cited on pages 10 and 14.]

Simpson, E. R., Fetherolf, T., Kane, S. R., et al. 2022, The Astronomical Journal, 163, 215 [Cited on pages 31 and 32.]

Siverd, R. J., Beatty, T. G., Pepper, J., et al. 2012, The Astrophysical Journal, 761, 123 [Cited on page 69.]

Smith, J. C., Stumpe, M. C., Van Cleve, J. E., et al. 2012, Publications of the Astronomical Society of the Pacific, 124, 1000 [Cited on page 25.]

Sotin, C., Grasset, O., & Mocquet, A. 2007, Icarus, 191, 337 [Cited on page 58.]

Soubiran, C., Jasniewicz, G., Chemin, L., et al. 2018, Astronomy & Astrophysics, 616, A7 [Cited on page 43.]

Sousa, S. G. 2014, arXiv:1407.5817 [Cited on page 44.]

Southworth, J., Hinse, T., Dominik, M., et al. 2009, The Astrophysical Journal, 707, 167 [Cited on pages 69 and 103.]

Sterne, T. E. 1939, Monthly Notices of the Royal Astronomical Society, Vol. 99, p. 451-462, 99, 451 [Cited on page 86.]

Storch, N. I. & Lai, D. 2014, Monthly Notices of the Royal Astronomical Society, 438, 1526 [Cited on page 91.]

Stumpe, M. C., Smith, J. C., Catanzarite, J. H., et al. 2014, Publications of the Astronomical Society of the Pacific, 126, 100 [Cited on page 25.]

Tanaka, H., Takeuchi, T., & Ward, W. R. 2002, The Astrophysical Journal, 565, 1257 [Cited on pages 1 and 2.]

Tenenbaum, P. & Jenkins, J. M. 2018, TESS Science Data Products Description Document: EXP-TESS-ARC-ICD-0014 Rev D, Tech. Rep. NASA/TM-2018-220036, NASA Ames Research Center [Cited on page 25.]

Teske, J., Wang, S. X., Wolfgang, A., et al. 2021, The Astrophysical Journal Supplement Series, 256, 33 [Cited on pages 43, 49, and 56.]

Thiabaud, A., Marboeuf, U., Alibert, Y., et al. 2014, Astronomy & Astrophysics, 562, A27 [Cited on page 59.]

Thiabaud, A., Marboeuf, U., Alibert, Y., Leya, I., & Mezger, K. 2015, Astronomy & Astrophysics, 574, A138 [Cited on page 58.]

Thorngren, D. P. & Fortney, J. J. 2018, The Astronomical Journal, 155, 214 [Cited on page 93.]

Thorngren, D. P., Fortney, J. J., Murray-Clay, R. A., & Lopez, E. D. 2016, The Astrophysical Journal, 831, 64 [Cited on page 86.]

Tinetti, G., Drossart, P., Eccleston, P., et al. 2018, Experimental astronomy, 46, 135 [Cited on page 14.]

Tregloan-Reed, J., Southworth, J., & Tappert, C. 2013, Monthly Notices of the Royal Astronomical Society, 428, 3671 [Cited on pages 70, 76, 82, 106, and 107.]

Tremblin, P., Chabrier, G., Mayne, N., et al. 2017, The Astrophysical Journal, 841, 30 [Cited on page 94.]

Turner, J. D., Flagg, L., Ridden-Harper, A., & Jayawardhana, R. 2021a, arXiv preprint arXiv:2112.09621 [Cited on page 69.]

Turner, J. D., Ridden-Harper, A., & Jayawardhana, R. 2021b, The Astronomical Journal, 161, 72 [Cited on pages 38 and 68.]

Unterborn, C. T., Desch, S. J., Haldemann, J., et al. 2023, The Astrophysical Journal, 944, 42 [Cited on page 15.]

Valencia, D., O'Connell, R. J., & Sasselov, D. 2006, Icarus, 181, 545 [Cited on page 15.]

Valencia, D., Sasselov, D. D., & O'Connell, R. J. 2007a, The Astrophysical Journal, 656, 545 [Cited on page 15.]

Valencia, D., Sasselov, D. D., & O'Connell, R. J. 2007b, The Astrophysical Journal, 665, 1413 [Cited on page 15.]

Van Eylen, V., Agentoft, C., Lundkvist, M. S., et al. 2018, Monthly Notices of the Royal Astronomical Society, 479, 4786 [Cited on pages xiii, 4, and 5.]

Venturini, J., Guilera, O. M., Haldemann, J., Ronco, M. P., & Mordasini, C. 2020, Astronomy & Astrophysics, 643, L1 [Cited on page 5.]

Vogt, S. S. 1987, Publications of the Astronomical Society of the Pacific, 99, 1214 [Cited on page 8.]

Vogt, S. S. & Keane, M. J. 1993, in American Astronomical Society, 183rd AAS Meeting, id. 11.01; Bulletin of the American Astronomical Society, Vol. 25, p. 1305, Vol. 25, 1305 [Cited on page 8.]

Von Essen, C., Mallonn, M., Piette, A., et al. 2021, Astronomy & Astrophysics, 648, A71 [Cited on page 69.]

von Paris, P., Hedelt, P., Selsis, F., Schreier, F., & Trautmann, T. 2013, Astronomy & Astrophysics, 551, A120 [Cited on page 1.]

Wahl, S. M., Hubbard, W. B., Militzer, B., et al. 2017, Geophysical Research Letters, 44, 4649 [Cited on page 88.]

Wang, W., Zhang, Z., Chen, Z., et al. 2024, The Astrophysical Journal Supplement Series, 270, 14 [Cited on pages 81 and 82.]

Weinberg, N. N., Davachi, N., Essick, R., et al. 2023, The Astrophysical Journal, 960, 50 [Cited on page 17.]

Weinberg, N. N., Sun, M., Arras, P., & Essick, R. 2017, The Astrophysical Journal Letters, 849, L11 [Cited on page 67.]

Wilkins, A. N., Delrez, L., Barker, A. J., et al. 2017, The Astrophysical Journal Letters, 836, L24 [Cited on pages 70, 81, and 104.]

Wilson, D., Gillon, M., rr, C., et al. 2008, The Astrophysical Journal Letters, 675, L113 [Cited on page 69.]

Wilson, O. 1978, Astrophysical Journal, Part 1, vol. 226, Dec. 1, 1978, p. 379-396., 226, 379 [Cited on page 32.]

Winn, J. N. 2010, Exoplanet transits and occultations, Vol. 55 (University of Arizona Press Tucson, AZ)

Wong, I., Benneke, B., Shporer, A., et al. 2020, The Astronomical Journal, 159, 104 [Cited on pages 76 and 82.]

Wong, I., Shporer, A., Vissapragada, S., et al. 2022, The Astronomical Journal, 163, 175 [Cited on pages 68 and 81.]

Wong, I., Shporer, A., Zhou, G., et al. 2021, The Astronomical Journal, 162, 256 [Cited on pages 1 and 68.]

Youdin, A. N. & Mitchell, J. L. 2010, The Astrophysical Journal, 721, 1113 [Cited on page 94.]

Zaleski, S., Valio, A., Marsden, S., & Carter, B. 2019, Monthly Notices of the Royal Astronomical Society, 484, 618 [Cited on page 24.]

Zechmeister, M. & Kürster, M. 2009, Astronomy & Astrophysics, 496, 577 [Cited on pages xiv, 48, and 51.]

Zeng, L. & Sasselov, D. 2013, Publications of the Astronomical Society of the Pacific, 125, 227 [Cited on page 15.]

Zeng, L., Sasselov, D. D., & Jacobsen, S. B. 2016, The Astrophysical Journal, 819, 127 [Cited on pages xv, 15, 63, and 101.]

Zeng, L. & Seager, S. 2008, Publications of the Astronomical Society of the Pacific, 120, 983 [Cited on page 15.]

Ziegler, C., Tokovinin, A., Briceño, C., et al. 2020, The Astronomical Journal, 159, 19 [Cited on page 44.]